

NUCLEAR MICRO-ENGINEERING USING TRITIUM

by

Baojun Liu

B.S., University of Science and Technology of China, 2002

M.S. in Physics, University of Pittsburgh, 2004

Submitted to the Graduate Faculty of

The Swanson School of Engineering in partial fulfillment

of the requirements for the degree of

Doctor of Philosophy in Electrical Engineering

University of Pittsburgh

2008

UNIVERSITY OF PITTSBURGH

SWANSON SCHOOL OF ENGINEERING

This dissertation was presented

by

Baojun Liu

It was defended on

November 21, 2008

and approved by

Joel Falk, PhD, Professor, Electrical and Computer Engineering Department, University of Pittsburgh

William Stanchina, PhD, Professor, Electrical and Computer Engineering Department, University of Pittsburgh

Minhee Yun, PhD, Professor, Electrical and Computer Engineering Department, University of Pittsburgh

Qing-Ming Wang, PhD, Professor, Mechanical Engineering and Material Science Department, University of Pittsburgh

Dissertation Director: Kevin P. Chen, PhD, Professor, Electrical and Computer Engineering Department, University of Pittsburgh

Dissertation Co-Director: Nazir P. Kherani, PhD, Professor, Electrical and Computer Engineering Department, University of Toronto

© Copyright 2008, Baojun Liu

NUCLEAR MICRO-ENGINEERING USING TRITIUM

Baojun Liu, PhD

University of Pittsburgh, 2008

We have been witnessing unprecedented progress in the arena of MEMS and nanotechnology. By shrinking the size of individual devices and using batch micro-electronics fabrication processes, complex micro/nano-systems with greater functionalities have been integrated on a single chip. The research in this thesis pushes NEMS approach into nuclear engineering. Characterized by long life-time and high power density, radioactive isotopes are appealing power sources for autonomous and very small volume micro-devices. By immobilizing tritium in thin film or on-chip, the multi-functional nature of the nuclear micro-engineering was exploited for a range of applications in betavoltaics, sensing, and on-chip radiators.

The objective of this thesis is to explore the miniaturization of these self-powered devices and systems using MEMS and nanotechnology approaches. In this study: a contamination-free, CMOS-compatible fabrication technique to integrate monolithically radioactive isotopes on-chip on a micrometer scale has been demonstrated; the application of micro-power generation and sensing are explored; a number of nuclear to electricity energy conversion devices with high-efficiency potential and excellent longevity have been explored; and, embedded on-chip isotope micro-sources have been used to create localized ionization sources for chip-scale gas chromatography sensors and radiators. The extension of micro-engineered radioisotope into MEMS and nanotechnology will generate research opportunities in other unattended fields.

TABLE OF CONTENTS

LIST OF TABLES	IX
LIST OF FIGURES	X
ABBREVIATIONS	XV
ACKNOWLEDGEMENTS	XVII
1.0 INTRODUCTION	1
1.1 BACKGROUND AND MOTIVATION	1
1.2 ORGANIZATION OF THESIS	5
2.0 BETAVOLTAICS	6
2.1 INTRODUCTION	6
2.2 PRINCIPLES OF SEMICONDUCTOR BETAVOLTAICS	8
2.3 SEMICONDUCTOR PN JUNCTION BETAVOLTAICS	12
2.4 HYBRID AND EMERGING BETAVOLTAICS	25
2.5 SUMMARY	27
3.0 RADIOISOTOPES	29
3.1 RADIOISOTOPES AND THEIR APPLICATIONS	29
3.1.1 Radioisotopes	29
3.1.2 Radioisotope for Betavoltaics	32
3.2 TRITIUM	34
3.2.1 Tritium Fundamentals	35
3.2.2 Tritium Handling Safety	37

4.0	THE HIGH TEMPERATURE AND HIGH PRESSURE TRITIUM EXPOSURE SYSTEM.....	38
4.1	APPARATUS DESIGN.....	38
4.2	EXPERIMENTAL SETUP.....	42
4.3	CHRONOLOGY OF A TRITIUM HIGH PRESSURE, HIGH TEMPERATURE EXPOSURE.....	43
4.4	SAFETY	46
4.5	SUMMARY	47
5.0	TRITIATION OF AMORPHOUS, CRYSTALLINE AND POROUS SILICON	49
5.1	INTRODUCTION	49
5.2	TRITIATED AMORPHOUS AND CRYSTALLINE SILICON.....	50
5.2.1	Sample Preparation, Tritiation and Characterization.....	50
5.2.2	Thermal Effusion	52
5.2.3	Fourier Transform Infrared Spectroscopy	62
5.2.4	Thermal Profiles.....	63
5.2.5	Discussion.....	67
5.2.5.1	Tritium Diffusivity and Solubility in Amorphous and Crystalline Silicon.....	67
5.2.5.2	Energy Energetic and Network Stability of Tritiated Amorphous and Crystalline Silicon.....	71
5.3	TRITIATED POROUS SILICON	73
5.4	RADIOACTIVE SURFACE ACTIVITY OF THE TRITIATED AMORPHOUS, CRYSTALLINE AND POROUS SILICON	75
5.5	SUMMARY	77
6.0	METAL TRITIDES AND CONTACT POTENTIAL DIFFERENCE BETAVOLTAICS 79	
6.1	METAL TRITIDES	79
6.2	BETAVOLTAICS USING CONTACT POTENTIAL DIFFERENCE.....	82

6.2.1	AIR-MEDIUM CPD BETAVOLTAIC	83
6.2.2	SEMICONDUCTOR SANDWICHED CPD BETAVOLTAIC	85
6.3	SUMMARY	88
7.0	TRITIUM BETAVOLTAICS USING SEMICONDUCTOR PN JUNCTIONS	89
7.1	THREE DIMENSIONAL SEMICONDUCTOR PN DIODE FOR BETAVOLTAICS 89	
7.2	HIGH PRESSURE TRITIUM POWERED P-SI DIODE	91
7.3	SCANDIUM TRITIDE POWERED P-SI DIODE.....	98
7.4	INTERNALLY OCCLUDED TRITIUM POWERED P-SI DIODE.....	99
7.5	SUMMARY	102
8.0	TRITIUM IN NANO-MATERIALS.....	103
8.1	INTRODUCTION	103
8.2	TRITIUM STORAGE USING CARBON NANOTUBES	104
8.3	ZNO NANOWIRE BETA-LUMINESCENCE.....	108
9.0	SELECTIVE LOCKING OF TRITIUM IN SILICA USING DEEP UV LASER IRRADIATION	113
9.1	INTRODUCTION	113
9.2	EXPERIMENTAL PROCEDURES.....	114
9.3	DEEP UV LASER LOCKING OF TRITIUM IN SILICA	115
9.4	TRITIUM SELF-LOCKING IN SILICA.....	120
9.5	TRITIATED SILICA AS A COLD ELECTRON SOURCE	122
9.6	SELECTIVE LOCKING OF TRITIUM IN SILICA	123
9.7	SUMMARY	125
10.0	NUCLEAR MICRO-ENGINEERING USING METAL TRITIDES	126
10.1	INTRODUCTION	126
10.2	FABRICATION OF THE ON-CHIP MICRO-SENSOR.....	128

10.3	EXPERIMENTAL TEST	131
10.3.1	The 3D Ionization Sensor	131
10.3.2	The 2D Ionization Sensor	135
10.3.3	The Micro-scale Ionization Sensor	137
10.4	SUMMARY	139
11.0	CONCLUSIONS AND FUTURE WORKS	140
11.1	CONCLUSIONS	140
11.2	FUTURE WORK	142
	BIBLIOGRAPHY	146

LIST OF TABLES

TABLE 3.1 Alpha and beta radioisotopes with half-life 2-100 years	31
TABLE 3.2 Radioactive isotope suitable for betavoltaic applications	33
TABLE 3.3 Basic tritium data.[45].....	36
TABLE 5.1 Substrate temperature, time duration of the deposition, thickness and hydrogen concentration in the <i>a</i> -Si:H films.....	51
TABLE 5.2 Tritium concentration, position of low temperature and high temperature peaks yielded by Gaussian deconvolution, fractional areas of the peaks, and the free energy of desorption for films BL1, BL2 and BL3 tritiated in tritium gas for 3.5 days at a temperature of 250 °C and a pressure of 120 atm.	55
TABLE 5.3 Tritium concentration, position of low temperature and high temperature peaks yielded by Gaussian deconvolution, fractional areas of the peaks, and the free energy of desorption for film BL1 tritiated in tritium gas of various temperature and pressure for 3.5 days.	59
TABLE 5.4 Tritium concentration, position of low temperature and high temperature peaks yielded by Gaussian deconvolution, fractional areas of the peaks, and the free energy of desorption for samples of <i>a</i> -Si:H, annealed <i>a</i> -Si:H and <i>c</i> -Si tritiated in tritium gas for 3.5 days at a temperature of 250 °C and a pressure of 120 atm.	60
TABLE 10.1 Radiation ionization energy and transverse range of tritium betas in air, argon and helium.	133

LIST OF FIGURES

Figure 2.1 a) Illustration of the basic p-n junction betavoltaic cell and associated band diagrams. b) Current-voltage characteristics of a typical photovoltaic device. c) Ideal circuit representation of a betavoltaic cell.	9
Figure 2.2 Ionization energy for various materials plotted versus bandgap energy [19].	11
Figure 2.3 Power source configuration of <i>Betacel</i> [20].....	13
Figure 2.4 Calculated J_{sc} vs time for silicon n ⁺ p cells coupled to ¹⁴⁷ Pm beta source, and corresponding P_{max} behavior assuming a Model 400 cell.[20].....	13
Figure 2.5 Betavoltaic microbattery based on a planar Si pn diode with electroplated ⁶³ Ni. a) Picture of a packaged sample. b) Configuration of a packaged microbattery [25].....	14
Figure 2.6 Betavoltaic microbattery based on a pn junction device on a bulk-micromachined inverted pyramid array. a) Tope view of inverted pyramid array. b) Liquid ⁶³ NiCl/HCl solution in the inverted pyramid array.[25]	15
Figure 2.7 Fabrication procedure for the 3D porous silicon diode. a) silicon wafer substrate. b) Macropores formed by electrochemical ethching. c) p-n junctions introduced on all surfaces by solid-source diffusion. d) Aluminium ohmic contacts constructed on both side. e) representation of the continuous p-n junction in two neighboring pores. Geometry and morphology of the 3D porous diode. f) SEM image (top view). g) SEM image (cross section) [7].	16
Figure 2.8 Schematic illustration of 3D betavoltaic self-aligned microfabrication process. b) top and side view of SEM of 3D betavoltaic. [26].....	17
Figure 2.9 a) Intrinsic betavoltaic device. b) p-i-n delta layer device. [6].....	18
Figure 2.10 Short circuit current as a function of time in pin device.[6].....	19
Figure 2.11 a) Cross-section of the AlGaAs/GaAs heterojunction. b) Open circuit voltage and short circuit curren of a 0.3 cm ² betavoltaic cell based on Al _{0.1} Ga _{0.9} As as a function of tritium gas pressure in semisphere with radium of 1cm.[32].....	21
Figure 2.12 a) IV characteristics of the SiC cell under beta illumination from 1 mCi ⁶³ Ni. b) Current and power generated versus voltage under beta irradiation from 8.5 Gbq ³³ P. [28, 29]	22

Figure 2.13 An illumination of a betavoltaic device using the indirect conversion method.	23
Figure 2.14 Schematic of the radioisotope powered piezoelectric generator. [40]	26
Figure 3.1 Tritium beta decay spectrum showing the energy distribution between the electron and neutrino.	35
Figure 4.1 Illustration of the high temperature high pressure tritium exposure chamber.....	40
Figure 4.2 Photograph of the high pressure, high temperature exposure apparatus after manufacturing. An American 10 cent coin in the foreground is provided as scaling. In the foreground is located a customized Helicoflex [®] seal. The heaters are not shown. [47].....	41
Figure 4.3 Photograph of samples within the high pressure, high temperature exposure apparatus as it rests within the glovebox. [47].....	43
Figure 4.4 Pressure and temperature profile during the pressurization step. [47]	44
Figure 4.5 Pressure and temperature profile during the depressurization phase. [47].....	45
Figure 5.1 Illustration of tritium effusion monitor. [56].....	53
Figure 5.2 (a) Total tritium effusion from tritiated <i>a</i> -Si:H films, and (b) tritium effusion rate as a function of temperature for samples BL1, BL2 and BL3 tritiated in tritium gas for 3.5 days at a temperature of 250 °C and a pressure of 120 atm. The Gaussian deconvolution of BL1 is shown as an inset.....	56
Figure 5.3 (a) Total tritium effusion from tritiated <i>a</i> -Si:H films, and (b) tritium effusion rate as a function of temperature for sample BL1 tritiated in tritium gas for 84 hours in various temperature and pressures. The Gaussian deconvolution of film tritiated at 100 °C, 70 atm is shown as an inset.	58
Figure 5.4 (a) Total tritium effusion from tritiated <i>a</i> -Si:H films, and (b) tritium effusion rate as a function of temperature for samples of <i>a</i> -Si:H, annealed <i>a</i> -Si:H and <i>c</i> -Si tritiated in tritium gas for 84 hours at a temperature of 250 °C and a pressure of 120 atm. The Gaussian deconvolution of tritiated annealed <i>a</i> -Si:H is shown as an inset	61
Figure 5.5 Absorption spectra of an <i>a</i> -Si:H film before and after tritium exposure. For clarity, the spectra of the <i>a</i> -Si:H before tritium exposure has been shifted up by 500 cm ⁻¹ [57].....	63
Figure 5.6 Hydrogen and tritium depth profiles of <i>a</i> -Si:H film BL1 obtained after an exposure to T ₂ gas at 250 °C and 120 atm for 84 hours. The concentration profiles for H and T were measured simultaneously.....	64
Figure 5.7 Hydrogen and tritium depth profiles of <i>a</i> -Si:H film BL2 obtained after an exposure to T ₂ gas at 250 °C and 100 atm for 132 hours. The concentration profiles for H and T were measured simultaneously.....	66

Figure 5.8 Hydrogen and tritium depth profiles of crystalline silicon obtained after an exposure to T ₂ gas at 250 °C and 100 atm for 132 hours. The concentration profiles for H and T were measured simultaneously.	67
Figure 5.9 SEM surface morphology and side views of a) deep-trenched crystalline silicon prepared by deep reactive ion etching and b) porous silicon prepared by electrochemical etching.....	74
Figure 5.10 The total tritium occluded in crystalline silicon as a function of the total surface area. [57].....	75
Figure 5.11 Ionization current induced by tritiated c-Si, a-Si:H, and p-Si samples per unit centimeter in air as a function of the bias voltage. The air gap is set at 1 cm.[57].....	77
Figure 6.1 Cumulative tritium effusion and tritium effusion rate as a function of temperature for scandium film exposed to tritium gas at 250 °C.	80
Figure 6.2 Ionization current density (<i>J</i>) due to the Sc:T film sample in air as a function of the bias voltage (<i>V</i>). The air gaps are set at 1, 2, 4, and 6 mm, respectively.[79].....	81
Figure 6.3 The schematic of the CPD Betavoltaic battery.....	82
Figure 6.4 The IV characteristics of the CPD cell with a size of 2.5 cm by 1.3 cm at the electrode distances of 0.1, 0.3 and 0.6 mm in air.[79].....	83
Figure 6.5 The short circuit current (<i>I_{sc}</i>) and the open circuit voltage (<i>V_{oc}</i>) as a function of the electrode distance (<i>d</i>).[79]	84
Figure 6.6 The schematic of the solid state CPD cell. The Sc:T is the cathode, Pt is the anode and a-Si:H is the semiconductor medium. [79]	86
Figure 6.7 The IV characteristics of the solid CPD cell in darkness before tritiation and betavoltaic performance after tritiation. [79].....	87
Figure 7.1 The SEM image of the 3D porous silicon device.....	91
Figure 7.2 An illustration of the tritium molecules in the pores of the p-Si device.....	92
Figure 7.3 The effective specific power due to the gaseous tritium impinging on the planar device surface, on the pore device surface, and the total specific power, as a function of the tritium pressure.	93
Figure 7.4 The IV characteristics of the 3D diode under tritium-free dark condition and at tritium pressure of 0.8 atm.....	95
Figure 7.5 a) The short circuit current density (<i>I_{sc}</i>), and b) the open circuit voltage (<i>V_{oc}</i>), as a function of tritium pressure.....	96

Figure 7.6 The output power (P_{out}) and the energy conversion efficiency (η_p) as a function of tritium pressure.	97
Figure 7.7 The IV characteristics of the 3D BV cell under dark conditions and when powered by a ScT film (indirect solid tritium).	98
Figure 7.8 The tritium effusion profile and the effusion rate as a function of temperature for the 3D silicon cell tritiated in tritium gas at 100 °C and 10 atm.	100
Figure 7.9 The IV characteristics of the 3D BV cell under dark condition and when powered by tritium incorporated into the porous surface (direct solid tritium).	101
Figure 8.1 Schematic of gas molecules in single-walled carbon nanotubes.	105
Figure 8.2 SEM image (top and side views) of the purified Single Wall Carbon Nanotubes.	106
Figure 8.3 Tritium effusion and tritium effusion rate as a function of temperature for CNT sample exposed to tritium gas at 70 atm and 100°C for 3 days.[97]	107
Figure 8.4 SEM image of the ZnO nanowires.	110
Figure 8.5 Photoluminescence spectra of undoped ZnO nanowires at room temperature. [112]	110
Figure 8.6 The emission spectrum of the ZnO nWs under beta illumination.	111
Figure 9.1 Total tritium effusion from silica films as a function of temperature. The total laser fluence is 0, 700, 3000, 4800 J/cm ² for traces A, B, C and D, respectively.[82].....	117
Figure 9.2 Tritium effusion rate as a function of temperature. The total laser fluence is 0, 700, 3000, 4800 J/cm ² for traces A, B, C and D, respectively.[82]	118
Figure 9.3 The Gaussian deconvolution of trace C, which yields a low temperature (LT) peak and a high temperature (HT) peak.	119
Figure 9.4 Percentage of tritium occluded in silica as a function of the total laser fluence.[82]	120
Figure 9.5 Tritium effusion from a tritiated silica film stored at room temperature for 2 weeks post high-pressure tritiation. Gaussian deconvolution shows two peaks at 240°C and 450°C.[82].....	121
Figure 9.6 Ionization current due to a 0.5 cm ² tritiated silica sample in air as a function of the bias voltage. The air gap is set at 2, 5, and 10 mm.[82]	122
Figure 9.7 The processing of the nuclear micro-engineering in silica employing high pressure tritium loading, UV laser irradiation and thermal effusion.....	124
Figure 10.1 The schematic of the on-chip sensing device.	127

Figure 10.2 The processing of the micro-chip.....	129
Figure 10.3 The microscopic picture of the planar sensors. a), Picture of millimeter scale sensor. b), Microscopic picture of micro-scale sensor.....	130
Figure 10.4 The collected current density in SAM at a biased voltage of 100 V as a function of the air gap.....	132
Figure 10.5 The collected current density from the ScT thin film as a function of the biased voltage measured by the SAM at an gas gap of 3mm a) and 6mm b) for air, argon and helium respectively.....	134
Figure 10.6 Current as a function of the bias voltage for electrodes at different distances.....	135
Figure 10.7 Current signals as a function of the bias voltage in air, argon and helium.....	136
Figure 10.8 Current signal of the microscale as a function applied voltage in air, argon and helium, respectively.....	138
Figure 10.9 Response of helium flux introduced into the microsensors in air.....	138
Figure 11.1 a) The SEM side view of the trenched silicon. b) The proposed betavoltaic cell using a 3D diode.....	144
Figure 11.2 Plot of open circuit voltage (V_{oc}) vs. the leakage current (I_o) per unit area (1 cm^2).145	

ABBREVIATIONS

<i>a</i> -Si	Amorphous silicon
<i>a</i> -Si:H	Hydrogenated amorphous silicon
<i>a</i> -Si:H:T	Tritiated hydrogenated amorphous silicon
BL	Beta-Luminescence
BV	Betavoltaic
<i>c</i> -Si	Crystalline silicon
D	Deuterium
DB	Dangling bonds
ELO	Epitaxial Lift-Off
FTIR	Fourier Transform Infrared Spectroscopy
H	Hydrogen
HT	High temperature
LRT	Lower temperature
LT	Low temperature
MEMS	Micro-Electro-Mechanical Systems
MWNTs	Multi-Walled Carbon Nanotubes
nWs	Nanowires
PECVD	Plasma enhanced chemical vapor deposition
PV	Photovoltaic

p-Si	Porous Silicon
RIMS	Radioactive Isotope Micropower Source
RL	Radio-Luminescence
SAM	Surface Activity Monitor
SIMS	Secondary Ion Mass Spectroscopy
SWNTs	Single-Walled Carbon Nanotubes
T	Tritium

ACKNOWLEDGEMENTS

I am grateful for the tremendous help and financial support from my advisor. Kevin P. Chen. Grateful to Professor Chen who took me to his group at a time when I needed a fresh research perspective. I would like to thank my co-advisor Professor Nazir P. Kherani of University of Toronto (UofT) for his time, advice, invaluable helps that lead the research into the right directions. I would like to thank Professor Stefan Zukotynski (UofT) and Professor Joel Falk for their help ranging from instrumentation to advice.

The project could not have been possible without the help of Dr. Armando Antoniazzi at Kinectrics. I would like to express my gratitude to Dr. Tome Kostaski and Dr. Yeghikyan for their endless support and kindness at the University of Toronto. A thank you goes to the staff especially Clive Morton at the Kinectrics Tritium laboratory for their valuable assistance.

I am very appreciative of my committee members for their guidance and advice. I also would like to extend my gratitude to Ms. Sandy Weisberg from the department.

I had the opportunity to be with good and decent people. Special thanks go to Dr. Stefan Costea, Keith Leong, Bernie Ting, Michael Chang, Johnson Wong at University of Toronto, and Michael Buric, Di Xu, Tong Chen, Ben Mcmillen, Charles Jewart, Qingqing Wang at the University of Pittsburgh..

My studies could not have been possible without the love, care, support and encouragement from my family. They have amazing strength and I admire them.

1.0 INTRODUCTION

1.1 BACKGROUND AND MOTIVATION

In the last two decades, we have witnessed unprecedented progress in the arena of semiconductor, MEMS/NEMS (micro/nano-electromechanical systems) and nanotechnology [1-5]. By shrinking the size of individual devices and using batch micro-electronics fabrication processes, exceedingly complex micro- and nano- systems with extraordinary functionalities have been integrated on a single chip. As “small is better”, micro-electromechanical and nano-devices offer orders of magnitude improvement in performance, power consumption and cost reduction over conventional bulk devices. As flexible technologies, MEMS and nanotechnology have significantly affected every category of product in both commercial and military sectors. MEMS approaches and fabrication technology have been used to produce micro-systems useful in a wide array of applications from health care, to automotive, to environmental protection, and to aerospace industries.

In this thesis, we push NEMS approach and nanotechnology into a new frontier of nuclear engineering. Nuclear engineering, based on fission, has been a primary way to generate electrical power for our daily life. However, public perception about the danger of radioactive fuel has hindered the progress of nuclear engineering during the last 30 years. The field has yet to ride the wave of the micro-electronics and nanotechnology revolution that took place in the last decade.

Due to the increased concern about global warming, nuclear engineering, especially nuclear power generation, is being given a fresh look as a potential candidate to reduce greenhouse gas emissions. The renaissance of nuclear engineering and recent advances of MEMS and nanotechnology offer a number of unique R&D opportunities when these two fields intersect.

One of the greatest challenges to autonomous MEMS/NEMS systems is the absence of high density and long-lifetime micro-power sources. Several technologies have been proposed or developed to produce miniature power sources such as miniaturized electro-chemical batteries and micro-fuel cells. The output power and longevity of these electro-chemical based micropower sources are limited by the chemical energy density ($<20 \text{ kJ/m}^3$). Since the MEMS/NEMS devices have much larger surface to volume ratio than their bulk counterparts, the power density required to operate ever smaller devices *in a given volume* is scaled down quadratically with the device size (\sim proportional to the surface area of device). At the same time, the total power of fuel source will scale down cubically with the battery size. This unfavorable power scaling rule demands ever higher power density micro-energy sources when we scale down MEMS into NEMS-based nano-systems.

Research and development on radioactive micro-power sources described in this thesis aim to address this challenge. Characterized by long life-time and extremely high power density, radioactive isotopes are appealing power sources for a number of micro-system applications. In contrast to chemical power sources, radioactive fuels offer four orders of magnitude higher power density ($\sim 10^5 \text{ kJ/cm}^3$). Unlike chemical fuel, the half life of many radioactive isotopes are measured by years rather than hours. Therefore, the miniaturization of nuclear fuel and energy conversion mechanisms promises dramatic improvement in the operational longevity of micro- and nano- systems.

The rapid advance of MEMS and nanotechnology not only underscores the potential importance of nuclear micro-power sources, but also brings new approaches to develop high efficiency, energy harnessing techniques on a micron-meter scale by exploiting the nanotechnology itself. In addition, the high energy particles produced by natural decay of isotopes have been widely used in medical imaging, cancer treatment, and various sensing applications. The integration of micro radioactive isotope sources on-chip with other micro-systems such as lab-on-chip might enable us to develop unique applications for medical diagnosis and treatment on a single cellular level. One of the daunting challenges for chip-scale nuclear micro-engineering is to develop a safe and cost-effective method to integrate radioactive material on-chip with minimal collateral damage to surrounding micro-electronics circuits or MEMS structures. It is also important that the process to integrate radioactive materials on-chip should be compatible with existing micro-fabrication processes with minimal radiation cross-contamination to the fabrication facilities.

This thesis describes the first comprehensive research, to our best knowledge, to address the fabrication challenge, material interaction between isotope and electronic materials/structures, and harnessing radioactive energy using nanostructures. The radioisotope chosen for nuclear micro-engineering is tritium.

Tritium (^3H , T), a radioisotope of hydrogen, is arguably the ideal candidate for on-chip applications given its benign radiation characteristics, its relatively long half-life of 12.3 years, and its economic accessibility [6-8]. Tritium decays to $^3\text{He}^+$ and releases energetic electrons with an average energy of 5.7 keV and a maximum energy of 18.6 keV. Tritium/hydrogen can behave as either an alkaline metal or halogen and can react with nearly all elements of the periodical table. Further, safe tritium handling is routine given its wide usage in radio-

luminescent structures [9], pharmaceutical drug development [10], and fusion fuel research [11].

A high temperature, high pressure gaseous exposure apparatus was constructed to immobilize tritium on-chip, which is capable of generating a tritium environment with a temperature up to 300 °C and a pressure up to 200 bars. This technique is flexible, compatible for the micro-scale device fabrication process, and has very limited contamination. This system enables the tritiation of a range of semiconductor, photonic, and metallic materials. To date there are very few semiconductor materials available that contain a stably bonded radioactive element. This thesis presents the first comprehensive investigation of this post-tritiation technique in the incorporation of high-density tritium in various materials including hydrogenated amorphous silicon (a-Si:H) and crystalline silicon (c-Si), silicon dioxide, and scandium thin film with the intention of applying those in betavoltaic, sensing, lighting, on-chip radiation devices, and other applications.

Utilizing the tritiation technique and modern materials and fabrication technology, a series of betavoltaic devices of high efficiency and longevity with different energy conversion mechanisms are exploited. The radioisotope is also introduced into novel nano-materials as the first experimental study of tritium interaction with nano-materials. The micro-engineered radioisotope sources on-chip are investigated for sensing applications.

Using the MEMS technology and the post-tritiation technique, radioactive sources can be integrated on-chip at micro-scale with minimized contamination. This localized radioisotope can be amenable to a range of unattended applications, especially in extreme environments, such as exploration, military and implanted applications. With micro-engineered radioisotope radiator, it also provides a potential application for single cell diagnosis for biomedical field. It

is expected that this nuclear micro-engineering will generate brand new respective areas in the research of science and technology.

1.2 ORGANIZATION OF THESIS

To aid the discussion, the state of art of the nuclear batteries especially betavoltaics using tritium is discussed in chapter 2. The radioactive properties of tritium are briefly given in chapter 3. In chapter 4 the tritium loading apparatus is described. The results on tritiation of various silicon materials are presented in chapter 5. Chapter 6 describes the structure and performance of betavoltaic cell using metal tritide and a contact potential difference device. The structure of the betavoltaic devices using the semiconductor materials and their performance are given in chapter 7. The interaction of tritium with nano-materials, carbon nanotubes and ZnO nanowire is presented in chapter 8. Nuclear micro-engineering using silica and metal tritides are given in chapters 9 and 10, respectively. Conclusions are given in chapter 11.

2.0 BETAVOLTAICS

In the 50 years since the pioneering work of Rappaport at RCA (Radio Corporation of America), significant strides have been made in the development of betavoltaics. Early research was motivated largely by long term remote space application. The betavoltaic cell was also utilized as power source in pacemaker in 1970s. With the emergence of new materials and micro and nano fabrication science and technology, betavoltaics is getting renewed attention in recent years. Due to their unique properties such as high power density and long working life, they are expected to provide power source on-chip for miniaturized electronic and electromechanical devices. Benefitting from advanced technologies, novel materials and techniques are utilized to develop high quality high efficiency betavoltaics. This chapter will review the history, the progress, and the ongoing research on betavoltaics. The potential and the future of betavoltaics are also discussed.

2.1 INTRODUCTION

Betavoltaics are generators of electrical current, which form batteries that derive the primary energy from a radioactive source emitting beta particles (electrons). The science of betavoltaics began with the discovery of the electron voltaic effect in 1937. Studies of the electron voltaic effect were first reported by Becker and Kurppke for selenium photoelements [12] and later by

Ehrenberg, Lang and West for selenium and copper oxide [13, 14]. It was found that those photoelements developed an electromotive force (EMF) under bombardment and led to a corresponding circulating current. The technology of betavoltaics began with the preparation of the working devices made with silicon, germanium and gallium arsenide with ^{147}Pm and ^{90}Sr – ^{90}Y sources [15-18]. The best device efficiency reported was 0.38%. Along with the experimental effort, theoretical analyses were carried out. The bandgap dependence of electron-hole pair generation by ionization radiation was presented experimentally by Klein [19], and the theoretical treatment of betavoltaics for a variety of semiconductor materials were presented by Olsen [20]. In 1970s, Donald W. Douglas Laboratories presented practical betavoltaic devices using planar silicon fueled with ^{147}Pm with efficiencies ranging from 0.7 to 2% [20]. The device was used as a power source for pacemakers.

In the past 30 years, the applications of betavoltaics are mainly for military, spacecraft and medical use. Recently, with the continual miniaturization of the electrical and electromechanical devices, the power sources have had to accordingly follow the same trend of shrinking in volume. The radioactive fuel has much higher power density compared to the conventional chemical batteries and had been proposed as a new means of generating power for onchip applications. Today, radioactive isotope micropower sources (RIMS) are drawing more and more attention from investigators. In the following section, the principles of operation of semiconductor betavoltaics and efficiency limits are discussed. Subsequently, an overview of semiconductor betavoltaics is presented. Thereafter, the chapter focuses on hybrid and emerging betavoltaic technologies, followed by concluding remarks on the potential direction and future of betavoltaics.

2.2 PRINCIPLES OF SEMICONDUCTOR BETAVOLTAICS

Analogous to photovoltaic devices, the basic operation of a semiconductor betavoltaic device involves two steps. The first is the absorption of betas which lead to the generation of electron hole pairs, while the second step is the separation of electron hole pairs giving rise to a current in the external circuit. In particular, the built-in electric field of a p-n junction serves to separate the electron hole pairs created by betas and establishes the attainable external potential of the betavoltaic device. Unlike the photons, the beta absorption usually occurs near the surface of semiconductor due to the large absorption cross section. A schematic of a basic semiconductor pn junction betavoltaic cell is shown in Figure 2.1a. Also included in the figure are its energy band diagrams in the dark and under beta irradiation. The current voltage characteristics of a betavoltaic device under dark and irradiated conditions are shown in Figure 2.1b. Defining parameters of a betavoltaic device under given irradiation are the short circuit current density, the open circuit voltage, the maximum power point determined by the maximum power rectangle, and the fill factor. The electrical circuit model of the betavoltaic consists of a current source, a diode, a shunt resistance R_{sh} in parallel, and a contact resistance R_s in series. The R_{sh} and R_s are ignored in an ideal circuit (Figure 2.1c). The current source represents the current generated by the beta particles in the device. The diode is placed parallel with the current source to model the rectifying behavior of the pn junction. Current from the betavoltaic device is the sum of the diode current and the current source and is given as equation (2.1), in which I_0 is the saturation current. Under the short circuit conditions ($V=0$), the short circuit current is equal to I_β . When there is no load, the open circuit voltage is given by equation (2.2).

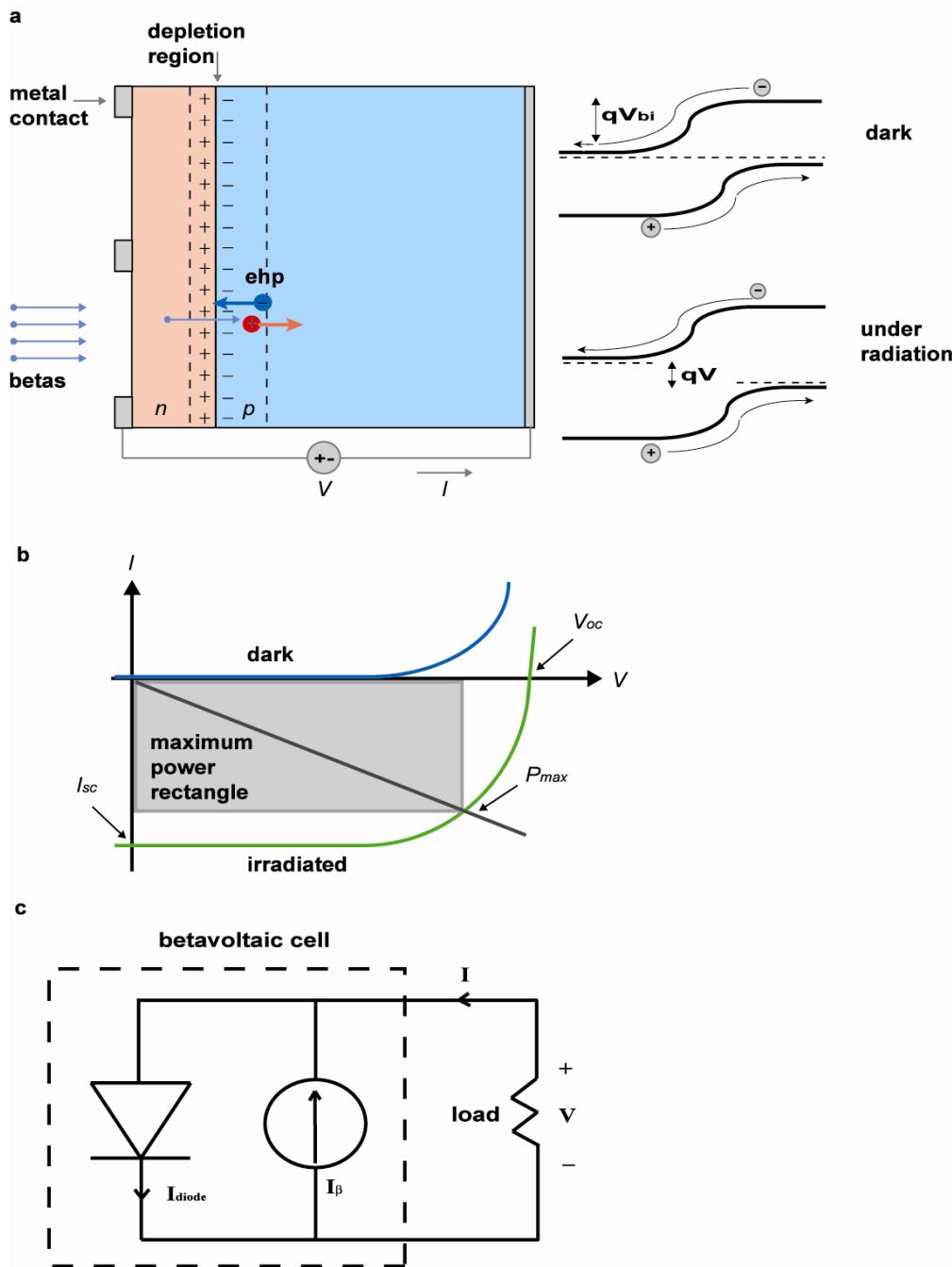


Figure 2.1 a) Illustration of the basic p-n junction betavoltaic cell and associated band diagrams. b) Current-voltage characteristics of a typical photovoltaic device. c) Ideal circuit representation of a betavoltaic cell.

$$I = I_0 (e^{qV/nkT} - 1) - I_\beta \quad (2.1)$$

$$V_{oc} = \frac{nkT}{q} \ln\left(\frac{I_\beta}{I_0} + 1\right) \quad (2.2)$$

As the betas travel in a semiconductor, they lose energy through interaction with the lattice. Electron hole pairs are created in a cascading process until the energy of the carrier is below the threshold energy. A portion of the energy is lost in the non-ideal processes which are categorized as optical phonon losses due to the instantaneous phonon generation, bandgap losses and thermalization losses due to energy transfer to the lattice. Klein determined experimentally that the radiation ionization energy required to create an electron hole pair is linearly dependent on the band gap of the semiconductor [19]. The radiation ionization energy (ε) is given by

$$\varepsilon = (14/5)E_g + r h\nu_R \quad (2.3)$$

where E_g is the bandgap of the material, r is the number of phonons created per ionization event, and $h\nu_R$ is the energy of an optical phonon. The equation provides a good fit to Klein's data which is shown in Figure 2.2. It is noted here that the radiation ionization energy of hydrogenated amorphous silicon is experimentally found to vary from 4.3 to 4.8 eV. Klein's formula yields a result that is in excess of the measured value. This can be corrected by modifying the coefficient of 14/5 to 11/5, thereby yielding a value of 4.5 eV.

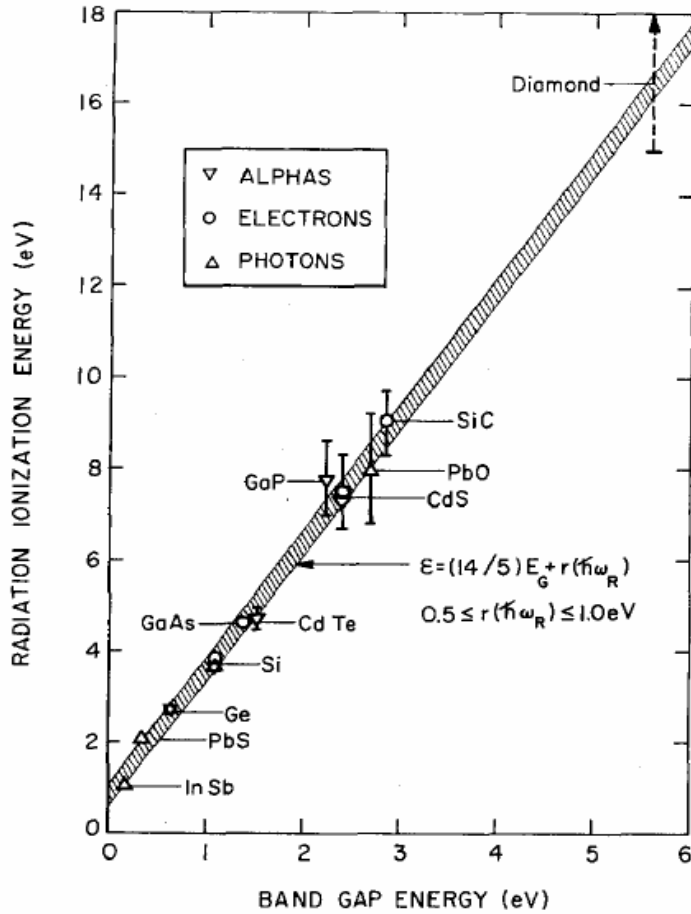


Figure 2.2 Ionization energy for various materials plotted versus bandgap energy [19].

One of the primary factors in selecting a given semiconductor material for betavoltaic applications is its potential maximum efficiency. From theoretical treatment of the betavoltaic performed by Olsen [21], the efficiency of betavoltaic conversion increases with the bandgap (E_g) of semiconductor converters. The theoretical analysis maximum of betavoltaic efficiency is about 20-22% for semiconductors with $E_g \sim 1.9 \text{ eV}$ and 13-14% for silicon. The semiconductors available for betavoltaics, such as Si, GaAs, GaP, SiC, have increasing bandgaps, thus efficiencies from betavoltaics using those are expected to increase accordingly.

2.3 SEMICONDUCTOR PN JUNCTION BETAVOLTAICS

Semiconductor p-n junctions were first suggested in the 1950s and the conversion efficiency was 0.5% due to suboptimal isotope choice and poor semiconductor quality. Great progress has been made in improving the quality of silicon, and new classes of semiconductor materials have emerged with wider band gaps than silicon. Higher efficiency of betavoltaic is expected with converters of high-band-gap materials[22]. The semiconductors have been utilized in betavoltaics include crystalline silicon[20], amorphous silicon[6, 8, 23, 24], patterned silicon[25, 26], porous silicon[7, 27], III-V semiconductor, and silicon carbide[28, 29].

Crystalline silicon pn junction was utilized to develop the commercialized betavoltaic cell by Donald W. Douglas Laboratory which is called *Betacel* batteries [20]. The basic approach for this power source fabricated is shown in Figure 2.3. They were fabricated with unidirectional beta sources which are made by vapor depositing Pm_2O_3 onto tantalum substrate, so only one side of the silicon diode is directly exposed to beta particle flux which is from ^{147}Pm due to the device geometry. The *Betacel* Model 400, which is named by the maximum power, 400 μW , utilizes ^{147}Pm of 66 Ci, produces a maximum voltage of 4V and short current of 112 μA . The efficiency is 1.7%. The behavior of the device depends on the beta flux determined by the source activity which decreases exponentially at a speed related to the half-life time of the radionuclide. The half life of ^{147}Pm is 2.6 years. Figure 2.4 shows the behavior of the calculated short circuit current density (J_{sc}) and the corresponding P_{max} versus time assuming a Model 400 cell. The *Betacel* batteries had 6- 8 year lifetime and 50-100 $\mu\text{W}/\text{cm}^3$ power density.

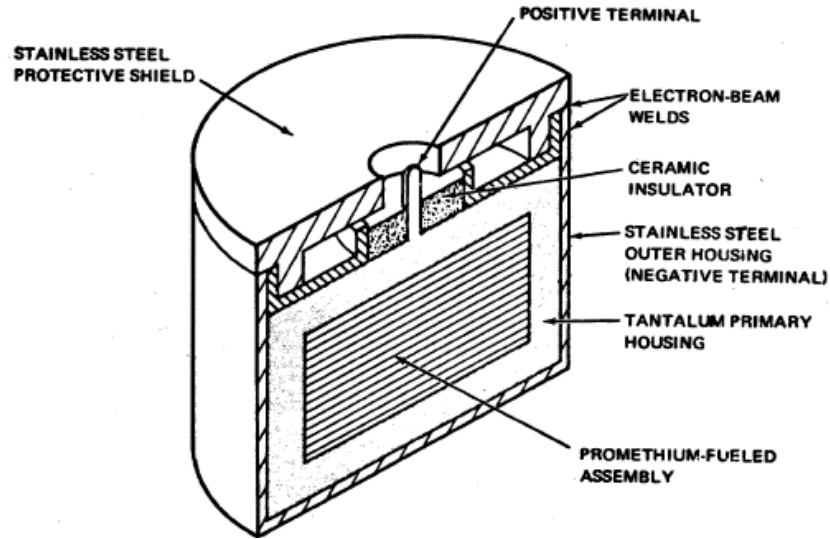


Figure 2.3 Power source configuration of *Betacel* [20]

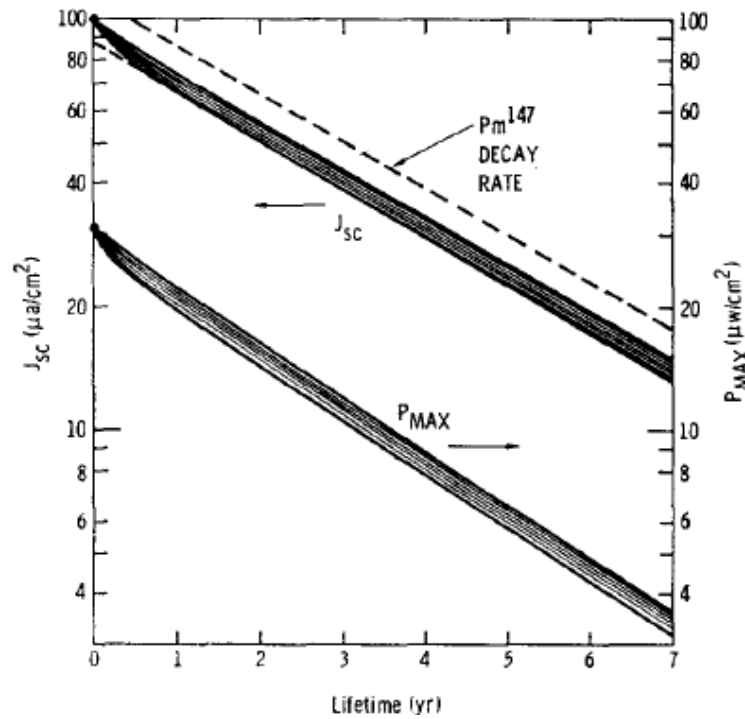


Figure 2.4 Calculated J_{sc} vs time for silicon n^+p cells coupled to ^{147}Pm beta source, and corresponding P_{max} behavior assuming a Model 400 cell.[20]

Converter with silicon is not expected to realize the maximum conversion efficiency in comparison with those of high bandgap materials. However, in view of the cost of the starting material, wide use of silicon devices, and advanced development of their technology, it is possible that mass production of betavoltaic batteries might favor less efficient but inexpensive and ecologically compatible silicon converters. As an inexpensive material with maturity in fabrication processing, silicon is also very useful in testing new configurations of betavoltaic devices.

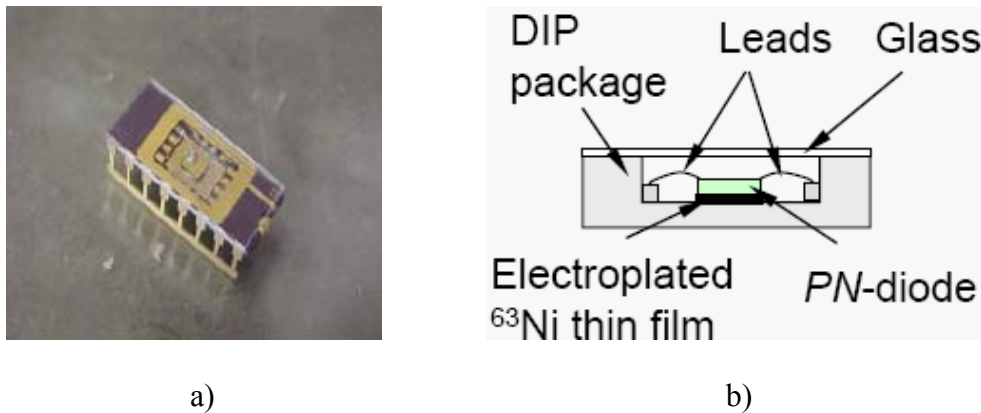


Figure 2.5 Betavoltaic microbattery based on a planar Si pn diode with electroplated ^{63}Ni . a) Picture of a packaged sample. b) Configuration of a packaged microbattery [25]

In an effort to make volume compatible power source for MEMS, betavoltaic microbatteries using silicon pn junction fueled with ^{63}Ni were demonstrated [25]. The picture and configuration is shown in Figure 2.5; the pn diode area is 4 by 4 mm². With a 1 mCi source, the short circuit current is 2.41 nA, the open circuit voltage is 115 mV, and the maximum output power is 0.24 nW. In order to increase the power, the pn junction area was increased by bulk-micromachining, by which the device was fabricated with inverted pyramid array as reservoirs

for liquid $^{63}\text{NiCl}/\text{HCl}$ solution (Figure 2.6). The area magnification is 1.85. On an inverted pyramid array occupied area of 4 by 4 mm², 125 μl $^{63}\text{NiCl}/\text{HCl}$ solution with activity of $8\mu\text{Ci}/\mu\text{l}$ produced an output power of 0.32 nW with a short circuit current of 2.86 nA and an open circuit voltage of 128 mV.

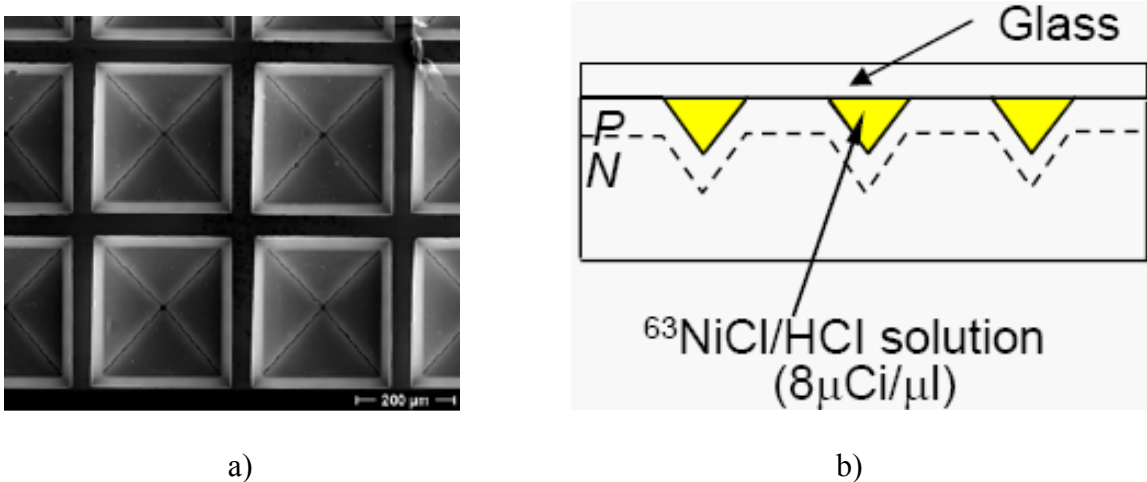


Figure 2.6 Betavoltaic microbattery based on a pn junction device on a bulk-micromachined inverted pyramid array. a) Top view of inverted pyramid array. b) Liquid $^{63}\text{NiCl}/\text{HCl}$ solution in the inverted pyramid array.[25]

In 2005, a betavoltaic device, called three-dimensional (3D) porous silicon diode, was proposed to increase the efficiency [7]. The fabrication of the device begins by introducing macropores in p-type silicon through electrochemical anodization. The pn junction was created in the pores through diffusion of n-type dopant. By introducing an appropriate radionuclide in the pores, this resulted in a volume effect battery. In this way, the energy conversion region and the source reservoir was combined. The fabrication process and the SEM images are shown in Figure 2.7. Tritium gas was used as the power source to test the device performance. It shows

that the efficiency was increased by ten fold in comparison with the planar diode. This increase in efficiency is largely due to the larger surface area; the porous silicon allows the tritium gas to penetrate into many pits and pores, greatly increasing the effective surface area of the device. The pn junction along the surface significantly increases the depletion region and thus enhance the electron-hole pair separation[27].

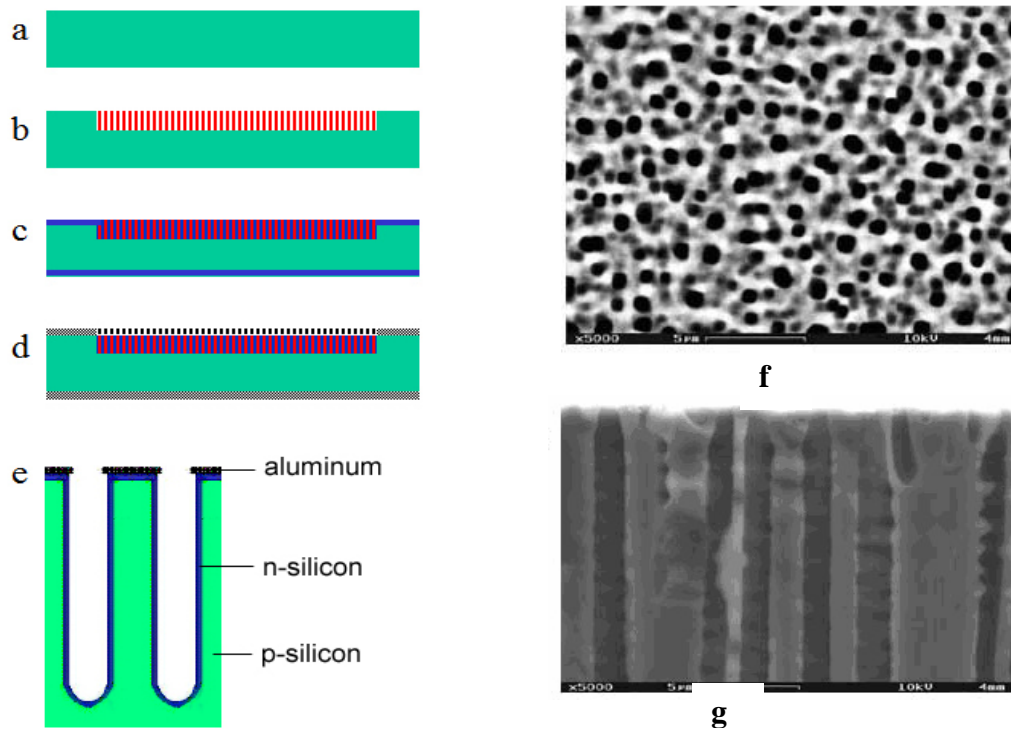


Figure 2.7 Fabrication procedure for the 3D porous silicon diode. a) silicon wafer substrate. b) Macropores formed by electrochemical etching. c) p-n junctions introduced on all surfaces by solid-source diffusion. d) Aluminium ohmic contacts constructed on both side. e) representation of the continuous p-n junction in two neighboring pores. Geometry and morphology of the 3D porous diode. f) SEM image (top view). g) SEM image (cross section) [7].

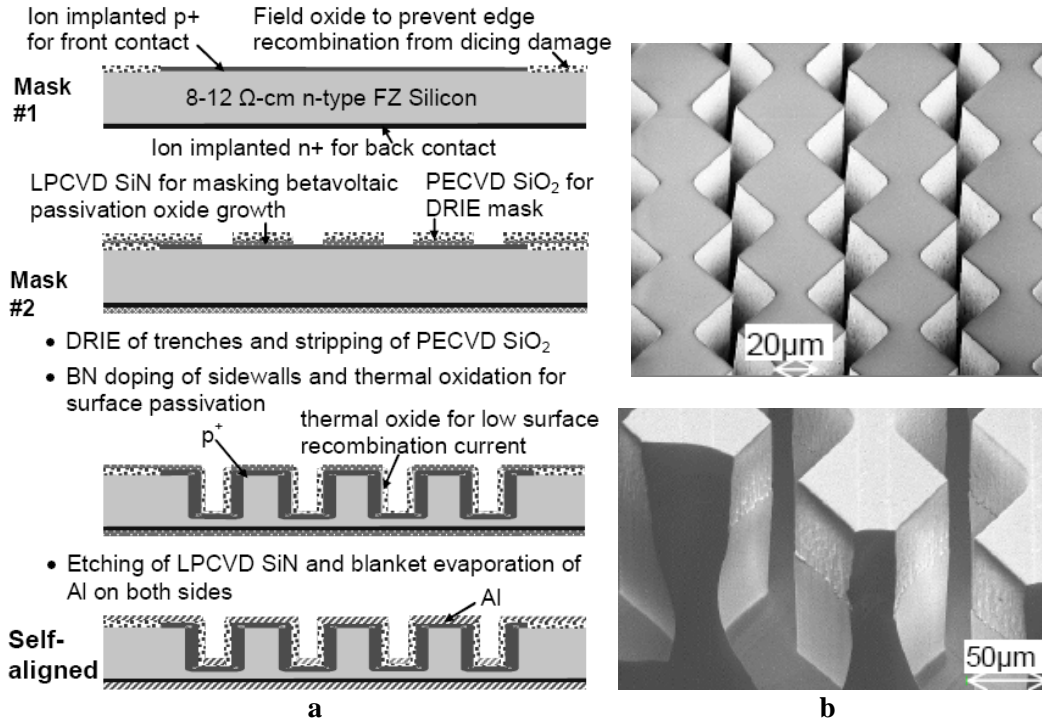


Figure 2.8 Schematic illustration of 3D betavoltaic self-aligned microfabrication process. b) top and side view of SEM of 3D betavoltaic. [26]

Lal and co-workers demonstrated prototype 3D silicon betavoltaics, micro-textured with deep reactive ion etched (DRIE) trenches, for potential application in 5 year lifetime 5 mW/cm³ ¹⁴⁷Pm powered microbatteries [26]. The devices were microfabricated in a 2-mask self-aligned process; the fabrication process and the SEM images are shown in Figure 2.8. The design increases the fuel fill factor by more than ten fold, thus to increase the power density. The performance of the cell was tested by SEM and an efficiency of 1.02% was obtained at a 30 kV acceleration voltage.

Thin film semiconductors are especially suitable for the development of commercial betavoltaic battery due to their low cost and compactness in stacked design. Among the currently available thin-film semiconductor materials, hydrogenated amorphous silicon (a-Si:H) is one of

the best choices for low cost low power energy sources. Advantages of a-Si:H over silicon include its wider bandgap and increased radiation hardness compared to silicon, as well as the low cost and compactness. Electron beam studies show that low-energy electron radiation induced defect creation stabilized at a level of around 10^{16} to 10^{17} cm^{-3} at room temperature depending on the fabrication process. Another favorable factor is the maturation of the a-Si:H in preparation of the solar cells [30].

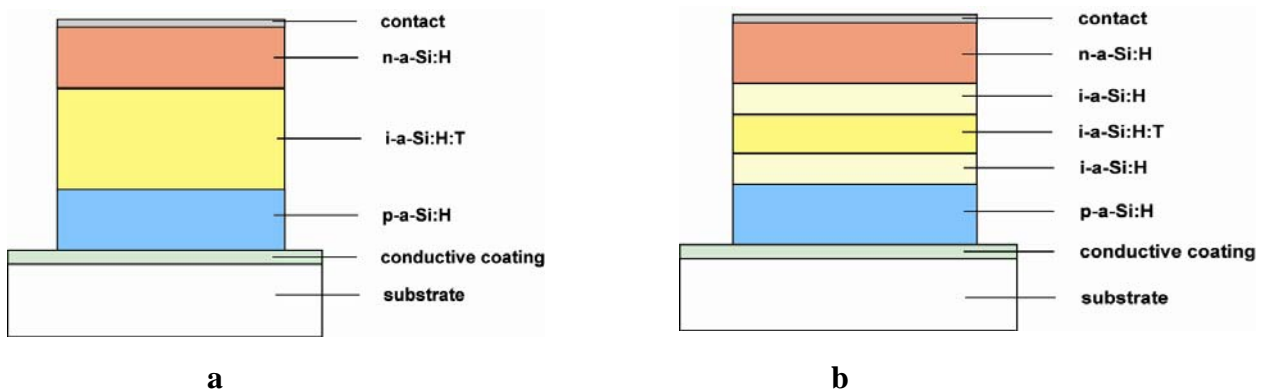


Figure 2.9 a) Intrinsic betavoltaic device. b) p-i-n delta layer device. [6]

Kherani and coworkers demonstrated the betavoltaic battery by incorporate the tritium in a-Si:H using their unique DC saddle-field plasma enhanced chemical vapor deposition (PECVD) technique [8]. They substituted tritium for hydrogen in a-Si:H to make the intrinsic tritiated amorphous silicon (a-Si:H:T) betavoltaic cell, a p-i-n junction. The configuration of the intrinsic tritiated amorphous silicon betavoltaic device is shown in Figure 2.9a. The tritium is within the energy conversion layer in contrast to betas originating from a source external to the device. The betavoltaic device using such intrinsic tritiated film is calculated to have a maximum conversion efficiency of 18%. A milli-watt power battery can be obtained by stacking a number of such cells

in series and or in parallel fueling with tritium of approximately 330 Ci. A 1mW battery is defined as that having this power output at the end of one tritium half-life. Tritium decay creates dangling bonds, and resultingly a nonuniform electric field develops in the intrinsic region of the p-i-n junction. This in turn increases the probability of the electron-hole pair recombination and the output power from the device decreases. The effect of these dangling bonds on the betavoltaic device can be reduced by using a thin slice of tritiated material to confine the tritium region and refer to this a delta layer configuration (Figure 2.9b). The behavior of devices with delta layers of different thickness with a device whose entire intrinsic layer was tritiated was compared, and the Figure 2.10 shows the short circuit current as a function of the time of the devices. As seen in Figure 2.10, the short circuit currents appeared to settle asymptotically to a fractional value greater than that of ‘uniform’. The difference in behavior is because dangling bonds in the delta devices are isolated in the delta devices [6].

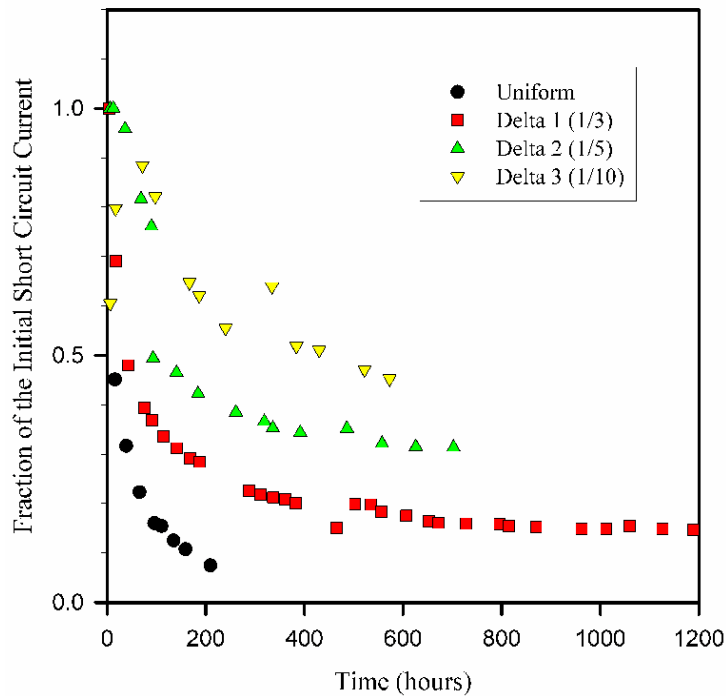


Figure 2.10 Short circuit current as a function of time in pin device.[6]

Hydrogenated amorphous silicon based betavoltaic cell powered with external source of tritium gas was also developed [24]. The p-i-n drift junction was deposited on the stainless steel substrate with an ultra thin layer of metal contact (5 nm). A large variety of cells were exposed in tritium gas at a pressure of 687 torr at room temperature for 46 days to test the performance. Initially a short circuit current density of 637 nA/cm^2 , an open circuit voltage of 457 mV, and an output power per unit area to matched load of 136 nW/cm^2 have been achieved with a 450 nm thick a-Si:H junction. Rather large degradation of junction performance has been observed due to diffusion of a significant amount of tritium into the a-Si:H film. The output power has dropped to about 6% of its initial value in 46 days.

The III-V semiconductors have been successfully used in photovoltaics for spaceflight. They have wider bandgap than silicon and showed good radiation tolerance. Series of studies of betavoltaics based on III-V semiconductor, such as GaP, GaAs, AlGaAs and GaN, have been reported. Betavoltic device consists of a GaP p-n junction device exposing to 3.3 kCi tritium has been reported [31]. The gas pressure was 1.03 MPa and the large concentration of tritium provides a significant flux of betas to the device. The initial short circuit current density was $1 \text{ }\mu\text{A/cm}^2$, and the open circuit voltage was 1V. The maximum output power density from this GaP betavoltaic device was $0.5 \text{ }\mu\text{W/cm}^2$. AlGaAs/GaAs heterojunction were developed for tritium-based betavoltaic application [32]. The heterostructure consists of n-GaAs substrate, n- $\text{Al}_x\text{Ga}_{1-x}\text{As}$ base layer, p- $\text{Al}_x\text{Ga}_{1-x}\text{As}$ ($x=0.1-0.37$) and p- $\text{Al}_{0.85}\text{Ga}_{0.15}\text{As}$ front layer of 10-30 nm thick (Figure 2.11a). Tritium betas are absorbed in the front thin layer and the separation of the minority carriers generated by the low energy beta radiation is highly efficient. A number of cells were experimented in tritium gas of 1-2 atm. The open circuit voltage and short circuit current density as a function of the tritium gas pressure of a typical cell is shown in Figure 2.11b. The

open circuit voltage and short circuit current density are in the range of 0.65-0.93 V and 0.75-1 $\mu\text{A}/\text{cm}^2$, respectively. The maximum output specific power of 0.51-0.55 $\mu\text{W}/\text{cm}^2$ was measured with fill factor of 0.8-0.85 in tritium gas. Titanium tritide was also used to power the cell, and open circuit voltage of 0.75V, short circuit current density of 0.04 $\mu\text{A}/\text{cm}^2$, and output power of 0.024 $\mu\text{W}/\text{cm}^2$ were measured, respectively. GaN, as a wide gap III nitride semiconductor, was also suggested by investigators as a candidate of betavoltaic device, and the design rule and radiation tolerance of GaN has been reported [33]

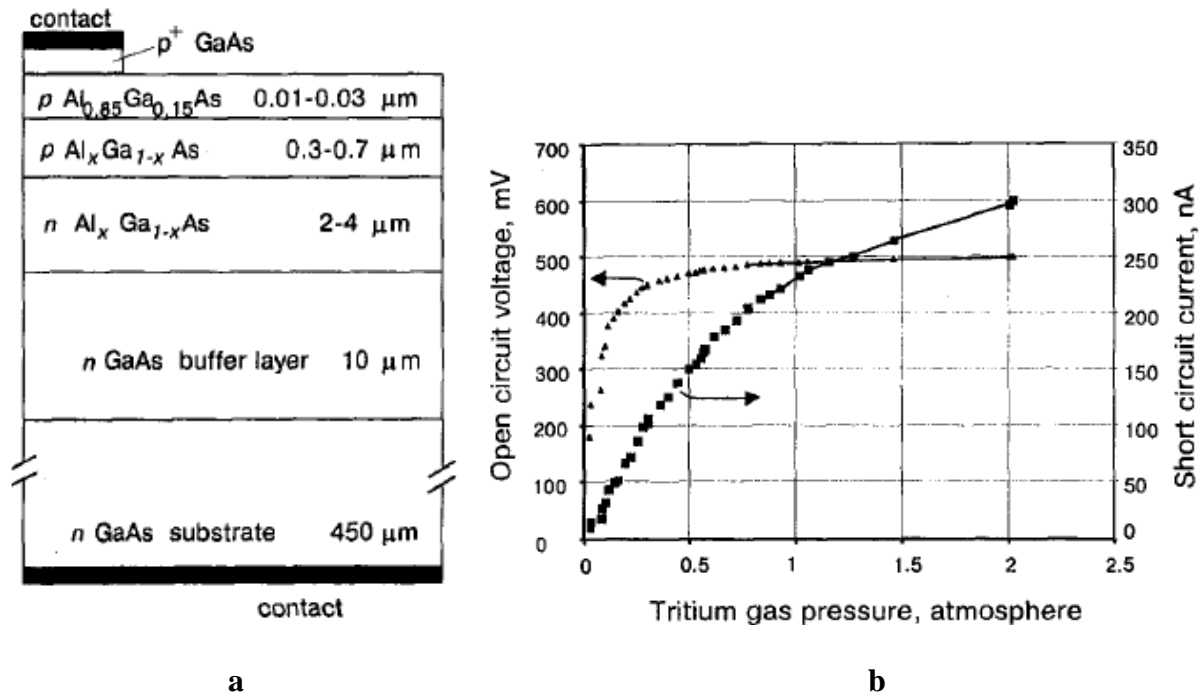


Figure 2.11 a) Cross-section of the AlGaAs/GaAs heterojunction. b) Open circuit voltage and short circuit current of a 0.3 cm^2 betavoltaic cell based on $\text{Al}_{0.1}\text{Ga}_{0.9}\text{As}$ as a function of tritium gas pressure in semisphere with radius of 1cm.[32]

Silicon carbide (SiC) is a wide band gap semiconductor (e.g. 3.3 eV for 4H SiC) which owns good thermal and electronic conductivity, and radiation harness. The wide bandgap

provides low leakage current, which is specifically favorable to low current betavoltaic applications. As predicted by theoretical analysis, the expected open circuit voltage and thus realizable efficiency of SiC betavoltaics are higher than of those alternative materials such as silicon. The SiC betavoltaic cells were reported by Cornell and Qyenergy in 2006, independently [28, 29]. In the Cornell cell, a p+ 4H SiC <0001> substrate cut 8° off axis from Cree was used as the substrate. A 4 μm thick active p layer background doped at $3 \times 10^{15} \text{ cm}^{-3}$, followed by a 0.25 μm thick n layer nitrogen doped at $2 \times 10^{18} \text{ cm}^{-3}$, were grown by chemical vapor deposition. Al/Ti were evaporated as the contact. The device was radiated from a 1 mCi ^{63}Ni source; an open circuit voltage of 0.72 V and a short circuit current density of 16.8 nA/cm² were measured (Figure 2.12a). The efficiency was 6%. Qyenergy utilized a SiC p-i-n junction and an 8.5 Gbq ^{33}P source was used power the cell. An open circuit voltage of 2.04 V and the peak power was 0.58 μW (Figure 2.12b). The conversion efficiency was 4.5%. The SiC cell showed a radiation resistant property and no degradation was observed over more than 3 months.

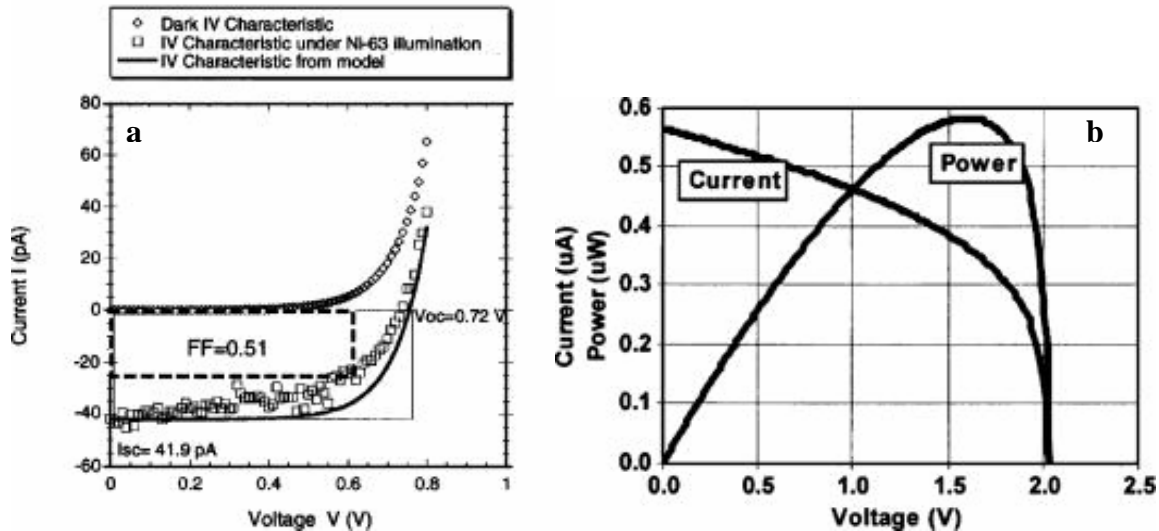


Figure 2.12 a) IV characteristics of the SiC cell under beta illumination from 1 mCi ^{63}Ni . b) Current and power generated versus voltage under beta irradiation from 8.5 Gbq ^{33}P . [28, 29]

Besides the direct conversion of the kinetic energy of betas into electricity, another important method is the indirect conversion. As illustrated in Figure 2.13, the indirect conversion method is a two step process. The beta flux strikes the phosphor film and emits photons; the photovoltaic device converts the photon energy into electrical energy. The Elgin-Kiddie cell utilizing the indirect conversion method was reported as early as in 1950s, which was made using a solar cell and a phosphor embedded with ^{147}Pm [34]. The delivered power was initially $20\ \mu\text{W}$. Due to the relatively short half life of ^{147}Pm , the battery is short lived. Betavoltaic using tritium, phosphor and a GaP solar cell has been proposed too. With a tritium pressure of 10.3 MPa to excite the phosphor, an output power density of $0.46\ \mu\text{W}/\text{cm}^2$ and an efficiency of $\sim 6\%$ were expected [31]

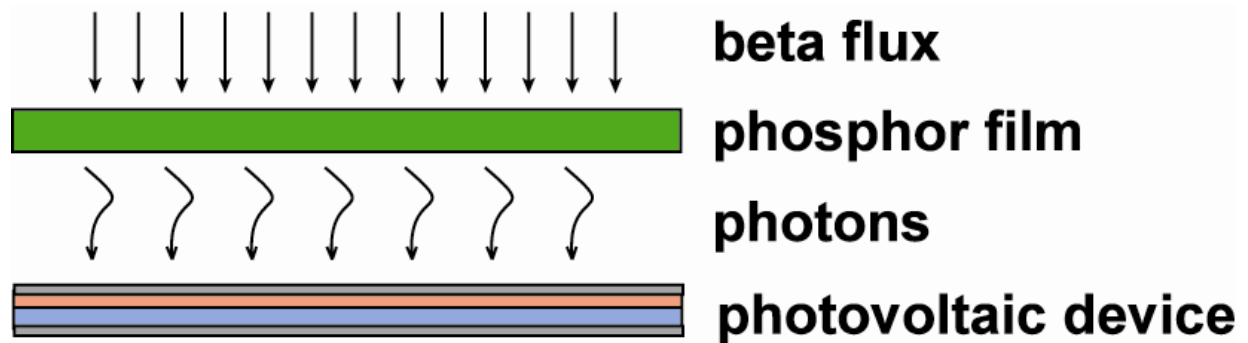


Figure 2.13 An illumination of a betavoltaic device using the indirect conversion method.

One important factor in the design with the indirect method is the light emission from the phosphor and the absorption of light by the solar cell should be matched. For example, using a GaP solar cell and a silver doped zinc sulphide results in good emission-absorption matching.[35]. The phosphor itself can convert about 25% of the beta particle energy into photons. Using the reported high efficiency solar cell of 35% with the III-V triple junction and

assuming a perfect emission-absorption match, an overall efficiency of 8% is expected for the indirect conversion betavoltaic device. The most practical radioluminescent light source would be the tritium lamp. The radioluminescent conversion efficiency of tritium beta to the light is about 10%, so an overall efficiency of 3% is expected for betavoltaics with tritium lighting source. Using $\text{Al}_x\text{Ga}_{1-x}\text{As}/\text{GaAs}$ junction, illuminated by a tritium green lamp, current density of $0.12 \mu\text{A}/\text{cm}^2$, open circuit voltage of 0.78 V, and output power of $0.074 \mu\text{W}/\text{cm}^2$ were obtained. The specific output power was 335 nW/Ci [32]. The a-Si:H PV cell has also been used for indirect conversion [24]. A radioluminescent lamp with tritium gas of 24.2 Gbq was involved to power a ZnS phosphor, open circuit voltage of 325.8 mV, short circuit current density of $13.42\text{nA}/\text{cm}^2$, and maximum power of $2.57 \text{nW}/\text{cm}^2$ were obtained. The two step conversion efficiency was 0.17%.

The indirect method is not the most efficient method of energy conversion because there are two steps involved, and the losses compound. The losses include the kinetic energy loss before the betas reach the phosphor film and the photon loss due to the configuration geometry. The good thing of the indirect method is that the stability of the phosphor is higher than the semiconductor device, and the indirect power output may surpass that of direct betavoltaic over a long term.[36] Another good factor of the indirect conversion method is the availability of various photovoltaics of high and ultra high efficiencies. With a matched wavelength of the radioluminescent light, a beta cell with competitive performance is expected.

2.4 HYBRID AND EMERGING BETAVOLTAICS

Direct charging method is the most straightforward one to convert the kinetic energy of the radioisotope into electricity [37]. The device involves two parallel metal plates with the radioisotope mounted on one of them. As the radioisotope decays, the electrons are collected on the second electrode while the first electrode builds up a positive potential. The build up of negative charge continues until electrons from the source can no longer overcome the electric field between the two electrodes. The average kinetic energy of the beta particles of the radioisotope ranges from several to a few hundred keV, consequently the developed potential can be of order of hundreds of kilovolts. The direct charging needs to be done in a vacuum condition. Utilizing a sandwiched dielectric medium can avoid the vacuum, though some of the kinetic energy will be consumed in the medium [38]. This direct charging capacitor is suitable of low current, high voltage applications.

A unique method to convert nuclear power into electricity is to utilize a contact potential difference (CPD) generated from two dissimilar metals [39]. Dielectric medium is sandwiched between two metal electrodes, which can be gas or dielectric thin film. An ionizing radiation source, dispersed within the dielectric source, provides energy source for electron-ion pair generation. Charged carriers are separated by the intrinsic electric field induced by contact potential difference and thus generate current to an external load.

A novel method using direct charging to excite cantilever, and subsequently convert the stored mechanical energy into electricity in a repeatable pulsed mode was reported. The device is called radioisotope powered piezoelectric generator and ^{63}Ni was utilized in it.[40] It was built on a self-reciprocating direct-charge cantilever, which utilized a direct collected-charge-to-motion conversion[41]. The reciprocation is obtained by self-timed contact between the

cantilever and radioisotope source. The radiated beta particles electrostatically charge a conductive plate on the underside of a piezoelectric unimorph. As the electrostatic field builds, the beam is attracted to the source until the contact is made and the field dissipates. At this point, the beam is released to vibrate at its natural frequency and the kinetic energy harvested from the piezoelectric film [40]. The schematic of the generator is shown as Figure 2.14. The piezoelectric unimorph supplies the load circuit with a directly usable voltage signal while shielding it from the high voltage generated owing to the radioisotope's direct charging. The overall efficiency of 2.78% was reported. To further increase the efficiency, a silicon betavoltaic cell was integrated to the cantilever to harness the wasted energy dissipated as heat in the cantilever. The converter utilized both the kinetic energy and the electric charge of the radioisotope, and an overall efficiency of 5.1% was reported [42].

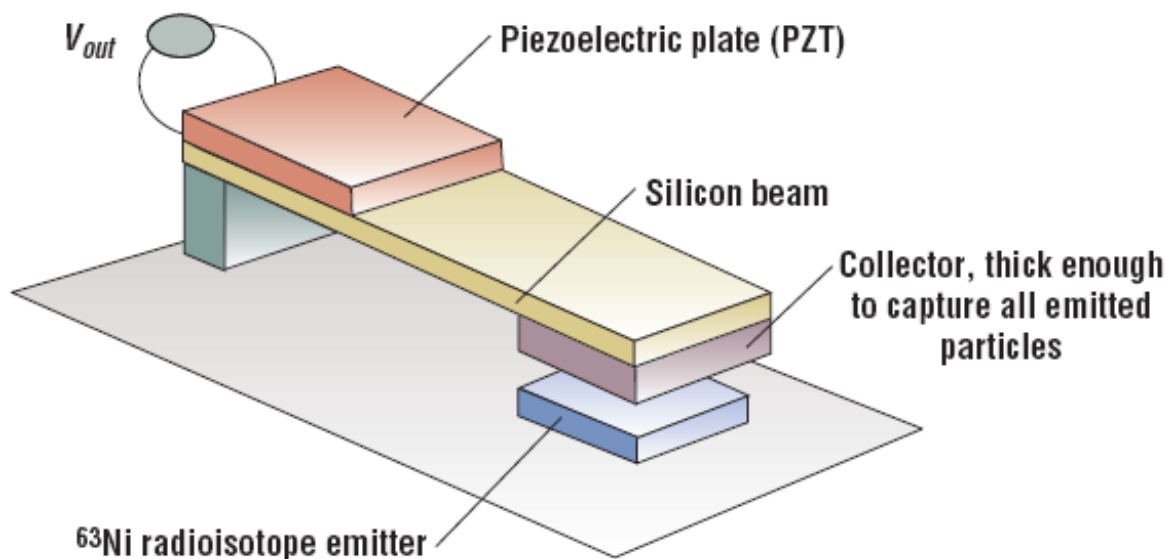


Figure 2.14 Schematic of the radioisotope powered piezoelectric generator. [40]

2.5 SUMMARY

The betavoltaics developed at RCA in 1950s ushered a generation of betavoltaic cells. They had been supplying electrical power for remote and long term use, such as spacecraft or remote sensing requires electrical powers for a decade or two, and some occasions that recharging is inaccessible, such as pacemakers. In recent years, with the miniaturization of the electronic and electromechanical devices, interests have been built in developing micropower sources for those miniaturized devices using betavoltaics. With the depleting and vulnerable fossil energy reserves, betavoltaics are also suggested as an alternative and supplement energy source. More and more efforts have put to develop high efficiency high power density betavoltaics using the novel materials and modern technologies. The development of betavoltaics has been benefited from the technology advance of related areas, especially the photovoltaics. The progress in semiconductor industry has been reflected in the betavoltaic development. With the progress of modern science and technology, especially the nanotechnology, it is not surprising to see more novel betavoltaics emerging in the near future. However, in general the investigation and development of betavoltaics lag far behind the similar photovoltaic devices. Up to now, the highest efficiency of the betavoltaics is about 6%, far lower than the predicted maximum. There is enough room for the betavoltaics in conversion efficiency to grow in the future.

The future of nuclear microbatteries depends on several factors, such as safety, efficiency, and cost. The scientists are working on those trying to improve the safety, enhance the efficiency and lower the cost, and solid progresses have been made. Once those challenges are overcome, the betavoltaics may power handheld devices like cellphone or PDAs. Nuclear microbatteries are not going to replace the chemical batteries. While as the continual shrinking of the electronic

devices, the betavoltaics compatible with the current semiconductor processing will provide the volume compatible battery and promises the micropower sources for onchip applications.

3.0 RADIOISOTOPES

3.1 RADIOISOTOPES AND THEIR APPLICATIONS

3.1.1 Radioisotopes

Radioisotopes are referred to atoms with an unstable nucleus, which loses energy by emitting radiation in the form of particles, alpha, beta or gamma. This phenomenon is called radioactivity. Radioactivity was first discovered in 1896 by the French scientist Henri Becquerel. Afterwards, Marie Curie, Pierre Curie, Ernest Rutherford and others carried out many more researches to further study the radioactive phenomena. The SI unit of radioactive decay is Becquerel (Bq). One Bq is defined as one decay per second. Another unit of decay is the Curie, which was originally defined as the radioactivity of one gram of pure radium, and is equal to 3.7×10^{10} Bq. The radioactive decay is random process, while it was found to be statistically exponential. The function 3.1 represents the exponential decay.

$$N(t) = N_0 e^{-\lambda t} = N_0 e^{-t/\tau} \quad (3.1)$$

Where N is the number of the atom at time t and N_0 is the atom number initially. The λ is called decay constant and τ is the time constant. In addition, a more commonly used parameter is half-life which is defined as

$$t_{1/2} = \frac{\ln 2}{\lambda} \quad (3.2)$$

The half-life is the time taken for half the radioactive atoms to decay.

To now, radioisotopes have found many applications in agriculture, industry, biochemistry, and environment. They are used as tracers in biochemistry and genetics, and they are also used to detect leaks and examine weld in industry, and trace and analyze pollutants in environment. In homes, most household smoke detectors contain the radioactive Americium-241, saving many lives. Radioisotopes play an important part in the technologies that provide us with food, water and good health. However, they can also constitute real or perceived dangers. If the radioisotopes are released into the environment, through accident, poor disposal, or other means, they can potentially cause harmful effects or radioactive contamination.

The most important application of radioisotopes is their use as nuclear fuel in the electrical power generation through fission process. With the fossil energy depletion and increasing concern of the global warming, more nuclear plants utilizing fission process are in construction and are going to generate electricity to meet the global energy thirsty. Besides the large scale power plants, radioisotopes also promise to provide volume-compatible power source for miniaturized electronic and electromechanical devices.[43] Owing to their unique properties of long life and high energy density, the radioactive isotope power sources (RIMS) are ideal power sources for on-chip application, and for remote and long term use such as spacecraft and implantable systems. Up to date many elements are found to have radioactive isotopes. They have different half lives. It is a remarkable aspect of the huge variety of isotopes, that only a few have lifetimes appropriate for long-life power supplies. Table 3.1 lists the main radioisotopes with half-life ranging from 2 to 100 years.

TABLE 3.1 Alpha and beta radioisotopes with half-life 2-100 years

Isotope	half-life	Ci/g	MeV	watt/g	wH/g
Alpha	years				10 years
¹⁴⁸ Gd	74.6	32.4	3.18	0.61	575,580
²⁰⁸ Po	2.898	593.1	5.12	17.82	667,021
²⁰⁹ Po	102	16.8	4.87	0.48	621,831
²²⁸ Th	1.9116	819.6	5.40	26.01	634,525
²³² U	68.9	22.4	5.31	0.70	612,566
²³⁶ Pu	2.858	531.2	5.75	17.91	660,728
²³⁸ Pu	87.7	17.119	5.49	0.55	616,347
²⁴³ Cm	29.1	51.6	5.84	1.73	649,579
²⁴⁴ Cm	18.1	80.9	5.80	2.76	646,947
²⁵⁰ Cf	13.08	109.3	6.02	3.87	659,014
²⁵² Cf	2.645	536.3	5.93	18.69	636,522
¹⁷² Hf	1.87	1123	0.15	0.960	22,889
Betas					
³ H	12.33	9664	0.01	0.324	52,041
⁴² Ar	32.9	259	0.23	0.354	149,745
⁵⁵ Fe	2.73	2381	0.00	0.053	1,870
⁶⁰ Co	5.2714	1130.36	0.10	0.637	43,963
⁶³ Ni	100.1	56.7	0.02	0.006	7,250
⁸⁵ Kr	10.756	392.3	0.25	0.577	81,022
⁹⁰ Sr	28.79	139.4	0.20	0.159	58,892
¹²⁵ Sb	2.7582	1048	0.09	0.524	18,631
¹³⁷ Cs	30.07	87	0.19	0.096	37,086
¹⁴⁶ Pm	5.53	443	0.08	0.216	15,628
¹⁴⁷ Pm	2.6234	927	0.06	0.338	11,404
¹⁵¹ Sm	90	26.3	0.13	0.019	22,127
¹⁵⁰ Eu	36.9	66.6	0.03	0.010	4,726
¹⁵² Eu	13.537	176.4	0.08	0.085	14,937
¹⁵⁴ Eu	8.593	264	0.23	0.360	40,529
¹⁵⁵ Eu	4.7611	465	0.05	0.134	8,338
¹⁷⁴ Lu	3.31	621	0.04	0.157	6,728
¹⁹⁴ Os	6	307	0.02	0.038	2,977
²⁰⁴ Tl	3.78	463.6	0.24	0.648	31,871

In the table, while the instantaneous power of radioisotopes (column 5) does not compare favorably to chemical batteries, integration of that power over long lifetimes shows very impressive energy density (column 6), 3 to 5 orders of magnitude higher than primary chemical cells. It is noted here that only a very limited radioisotopes are readily available, e.g. Pu-238 is available through Pacific Northwest National Lab and Oak Ridge National Lab for approximately \$10,000/g while tritium is available from Ontario Power Generation or Ontario Hydro for \$10,000/g. Other radioisotopes in multi-Curie quantities are very difficult to obtain in the United States where nuclear fuel has not been reprocessed for a few decades.

3.1.2 Radioisotope for Betavoltaics

Due to the small cross section of neutron and gamma rays, they are relatively difficult to be shielded and collected in energy conversion in comparison with alpha and betas. Thus, the radioisotope micro-power sources usually involve alphas and betas. The generators to convert alpha and beta energies into electricity are called alphavoltaics and betavoltaics, respectively. Typically they consist of a radiation source and a semiconductor diode. For a long-lived semiconductor based device, only the beta-emitting radioisotopes are suitable in the view of the fact that semiconducting materials are very susceptible to the defect damage caused by alphas. As a candidate for betavoltaic applications, the element should be relatively safe, chemically stable, readily available and relatively inexpensive. Multiple factors of the beta emitter affect the performance of the betavoltaic device. The energy spectrum of the emitted particle determines the penetration depth of the particle in the given semiconductor material impacting the device design, radiation damage, power and safety of the betavoltaic device; the half life and the

specific activity determine the available power. The beta-emitting isotopes, which are suitable for betavoltaic application and had been utilized before, are compared in Table 3.2.

TABLE 3.2 Radioactive isotope suitable for betavoltaic applications

Isotope	E_{ave} (keV)	E_{ave} (keV)	Half-life (yr)	Transverse range in Si (μm)	Power density (mW/cm^3)
$^{90}\text{Sr}/^{90}\text{Y}$	540/2.3	196/935	28.6	76	1205
^{147}Pm	62	230	2.6	24	2121
^{63}Ni	17.3	67	92	2.1	68
Tritium T_2 (gas)	5.7	18.6	12.3	0.7	0.087
Ti:T hydride (1:3)	5.7	18.6	12.3	0.7	270

The $^{90}\text{Sr}/^{90}\text{Y}$ has high power density of $1205 \text{ mW}/\text{cm}^3$ and long half life of 28.6 years. It is a good choice for higher power application if the semiconductor has sufficient radiation resistance to the high energy particles and if the converter is properly shielded.

The ^{147}Pm has been used in pacemaker. It has lower particle energy compared with $^{90}\text{Sr}/^{90}\text{Y}$ and it has a high power density of more than $2\text{W}/\text{cm}^3$. The half life of ^{147}Pm is 2.6 years and a device using ^{147}Pm objects a lifetime of 1 -2 half-life. The energy density for a 5 year output is $170 \text{ MJ}/\text{cm}^3$.

The ^{63}Ni has a lower energy decay, a higher half life, lower activity and power density. ^{63}Ni poses low chemical hazard and the low radiation can be shielded by thin layer ($< 30 \mu\text{m}$) of most materials. It can be readily incorporated into a semiconductor device as the nickel can be plated

to the semiconductor surface. The ^{63}Ni has also been employed in industry as electron capture devices for gas chromatography.

Tritium is a pure beta emitter producing energetic electrons with an average energy of 5.7 keV and a maximum energy of 18.6 keV, which pose little radiation damage concern for on-chip energy conversion devices. The half life of tritium decay is 12.3 years. Tritium is also considered as relatively safe and poses little health hazard. Unlike any other isotope sources, tritium is abundantly available at very low cost. Tritium handling is routine owing to the mature tritium lighting industry. Due to the benign radiation characteristics, availability and handling safety, tritium is arguably the idea candidate for betavoltaic applications.

3.2 TRITIUM

Tritium, chemical symbol ^3H or T, is a radioisotope of hydrogen. It was first predicted in the late 1920s by Walter Russell, and then produced in 1934 from deuterium by Ernest Rutherford. In the last couple of decades, the interests in the tritium research is grown markedly with its appearance in heavy water nuclear reactors, applications in self-powered lighting and radiotracer in biomedical studies, significant use in fusion fuel, and applications in agricultural and environmental studies such as water or wine dating. The growing tritium activity pushes and more tritium related studies and will continue to rise.

3.2.1 Tritium Fundamentals

The nucleus of tritium contains one proton and two neutrons. Its atomic weight is 3.0160492. It is in gas form (T_2) at standard temperature and pressure. Tritium combines with oxygen to form tritiated water HTO or T_2O . Tritium decays to ${}^3\text{He}^+$ and releases energetic electrons with an average energy of 5.7 keV and a maximum energy of 18.6 keV, while the remaining energy is carried off undetectably by the antineutrino.



The tritium decay spectrum is shown in Figure 3.1 and the half life is 12.3 years. Some tritium basic data is listed in Table 3.3.

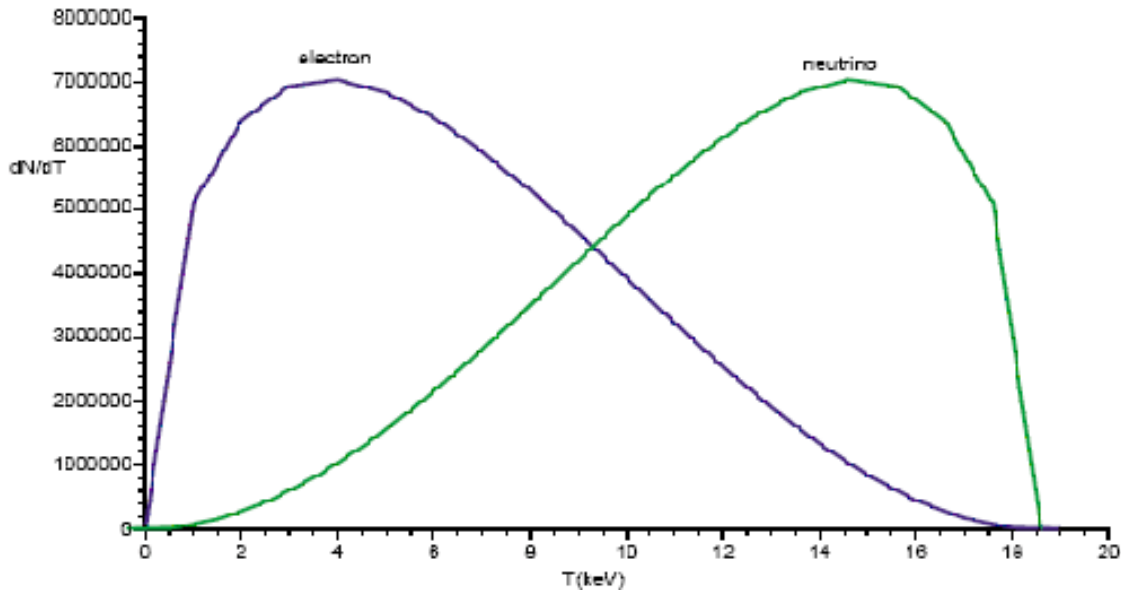


Figure 3.1 Tritium beta decay spectrum showing the energy distribution between the electron and neutrino.

Due to its benign radiation characteristics, its relatively long half-life of 12.3 years, and its economic accessibility[6, 7], tritium is particularly suitable for semiconductor betavoltaic energy conversion devices. Considering that the threshold electron energy for disruption of the silicon lattice due to knock-on collisions is 20 keV [44], tritium decay beta particles pose little radiation damage concern for on-chip applications.

TABLE 3.3 Basic tritium data.[45]

Atomic weight	3.01605 g
Half life	12.3 years
Decay constant (λ)	$1.782 \times 10^{-9} \text{ s}^{-1}$
Maximum β energy	18.6 keV
Mean β energy	5.69 keV
Decay β energy	0.911 $\mu\text{W/GBq}$
Maximum range of β in air	4.5-6 mm
Maximum range of β in water	5-7 μm
Specific activities	1 g = 355.7 TBq (9615 Ci*) 1 mole = 2146 TBq (58000 Ci) 1 cc (STP**) = 96 GBq (2.6 Ci)

* 1 Ci (curie) = 3.7×10^{10} disintegrations s^{-1} = 3.7×10^{10} Bq (bequerel)

** STP: Standard Temperature (0 °C) and Pressure (101.325 kPa)

3.2.2 Tritium Handling Safety

As shown in Table 3.3, the maximum range of an 18.6 keV beta particle is 6mm in air, while in water it is only 7 μm . The range of an 18.6 keV beta particle in soft tissue is 6 μm which is not sufficient to reach the radiosensitive layer of the skin, which is about 50 μm deep. [46] Tritium external to the human body poses little threat as a radiation hazard. However, tritium is a radiation hazard when within the body via inhalation or ingestion.

The human body does not readily absorb tritium in gaseous form; only $4 \times 10^{-3}\%$ of tritium gas that is inhaled is absorbed. However, the human body readily absorbs tritium in oxidized form (tritiated water). If tritium is absorbed by the human body as water, then the biological half-life about 10 days. [46] This can be reduced by increased consumption of liquids. The ICPR (International Commission on Radiological Protection) annual limit on intake (ALI) for tritium is 81 mCi, which is the highest level tolerated of any radioisotope. In view of the short range of beta particles emitted by tritium and the short biological half-life, tritium is considered to be one of the least hazardous radioactive isotopes.

4.0 THE HIGH TEMPERATURE AND HIGH PRESSURE TRITIUM EXPOSURE SYSTEM

The tritium loading was performed by high temperature and high pressure exposure. Usage of radioactive tritium required limiting at any given moment on the vulnerable quantity of tritium available for accidental release to surrounding environment. A tritium exposure system was built at the Kinectrics Tritium Laboratory to satisfy the competing requirements of high pressure (10 to 20 Mpa), high temperature and minimum inventory. This chapter described the high temperature and high pressure exposure system[47].

4.1 APPARATUS DESIGN

Review of the literature on work conducted using hydrogen indicated that the exposure apparatus would have to be able to generate gaseous tritium pressures in the range of 101 kPa to 21 MPa with temperatures ranging from 300 to 523 K. The exposure length was anticipated to vary from 1 hour to days. The gas volume needed to be minimized because: one, a heated, compressed gas is a significant source of stored energy and two, keeping the inventory of vulnerable tritium as low as possible.

The driving element in the design was the method by which the high pressure was to be generated. The choice was made to utilize cryogenically cooled (77 K) molecular sieve as a means of generating the high pressure. Molecular sieves cooled to liquid nitrogen temperatures are known to adsorb a substantial amount of hydrogen [48]. Specifically, at one atmosphere of hydrogen pressure the molecular sieve can adsorb approximately 5 millimoles of H₂ per gram of molesieve. Heating to room temperature of the molecular sieve material will release all the adsorb material generating the required pressure.

For the tests the tritium would reside on an Amersham bed, which contain 300 g of Uranium, and transferred to the exposure apparatus on need. Utilization of the Amersham bed kept the tritium in its original shipping container. The tritium, approximately 22 TBq or 6000 Ci, was purchased from Ontario Power Generation and shipped to Kinectrics in the international approved container of which the Amersham Uranium bed is a component.

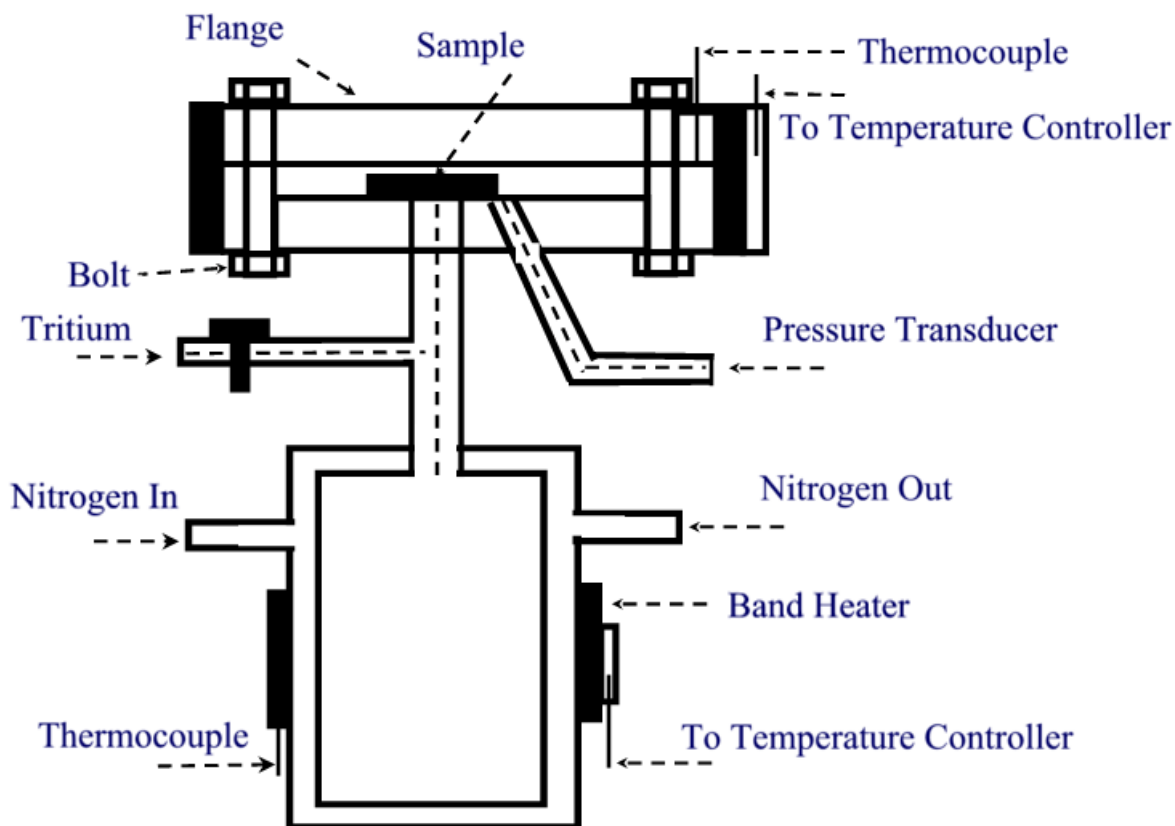


Figure 4.1 Illustration of the high temperature high pressure tritium exposure chamber.

A chamber thickness of 2.5 mm was deemed adequate to hold the samples. The area to be occupied by the samples required a couple square centimeters. The exposure apparatus design was arrived at by considering the required pressure, temperature, the physical volume occupied by valves and fittings and the method by which the pressure was to be generated. Figure 4.1 is an illustration of the exposure chamber and Figure 4.2 a photograph of the exposure apparatus prior to final assembly and mounting in the glovebox.



Figure 4.2 Photograph of the high pressure, high temperature exposure apparatus after manufacturing. An American 10 cent coin in the foreground is provided as scaling. In the foreground is located a customized Helicoflex[®] seal. The heaters are not shown. [47]

The space between the two 57 mm OD flanges of 2.5 mm depth and ~38 mm diameter defines the exposure volume. The cylinder attached to the flange incorporates the molecular sieve material and an annular region for flowing liquid nitrogen. The chamber is constructed from 316 SS. A high-pressure diaphragm valve from Swagelok with a polyamide seat isolates the exposure chamber from the tritium supply. A 316 SS Kulite sensor (0 to 35 MPa) is used to measure the exposure pressure. Sixteen grams of 5A molecular sieve (3 mm OD pellets) is used

for absorbing the tritium. The seal on the flange utilizes a specially designed and manufactured Helicoflex[®] seal from Garlock. Eight SAE J429 Grade 8 bolts are utilized to generate the sealing pressure on the Helicoflex seal. The final void volume, minus the samples, holding the T₂ is 31 cc.

The exposure apparatus was proof tested, using nitrogen, to 270 °C and at a pressure of 23.7Mpa (3450 psig) as per ASME specifications for pneumatic tests. Subsequent to proof testing and prior to tritium tests, the apparatus was tested with hydrogen to ensure the apparatus was capable of generating the required exposure conditions. The apparatus performed as expected.

4.2 EXPERIMENTAL SETUP

The process loop, tritium supply and exposure apparatus are contained in a closed glovebox with a volume of ~0.5 m³. The dry nitrogen atmosphere within the glovebox is continuously circulated through a Cleanup System. The Cleanup System has a metal bellows pump which moves gas from and to the glovebox at approximately 2 lpm. In circuit with the metal bellows pump are in-line tritium ionization monitors, a molecular sieve trap and a 5 kg Zr₂Fe metal hydride bed. One tritium monitor records the tritium concentration of the gas entering the glovebox while the second tritium monitor records the tritium concentration after the gas is scrubbed of tritium by the Zr₂Fe bed. To protect the glovebox from over pressurizing and rupturing a pressure relief system, consisting of two glycol filled bubblers, 7 to 8 inches of water equivalent, is connected between the glovebox atmosphere and the main laboratory exhaust.

4.3 CHRONOLOGY OF A TRITIUM HIGH PRESSURE, HIGH TEMPERATURE EXPOSURE

The samples to be exposed are transferred into the glovebox via a transfer port. Once the samples are within the glovebox they are placed on the flange of the exposure chamber as shown in Figure 4.3. A new Helicoflex seal is used when closing the chamber. At this stage vacuum is drawn on the apparatus using the process loop's vacuum pumps. Upon reaching base vacuum the valve on the exposure apparatus is closed isolating the exposure chamber. Monitoring of the internal pressure of the exposure apparatus overnight indicates any gross type of leaks.

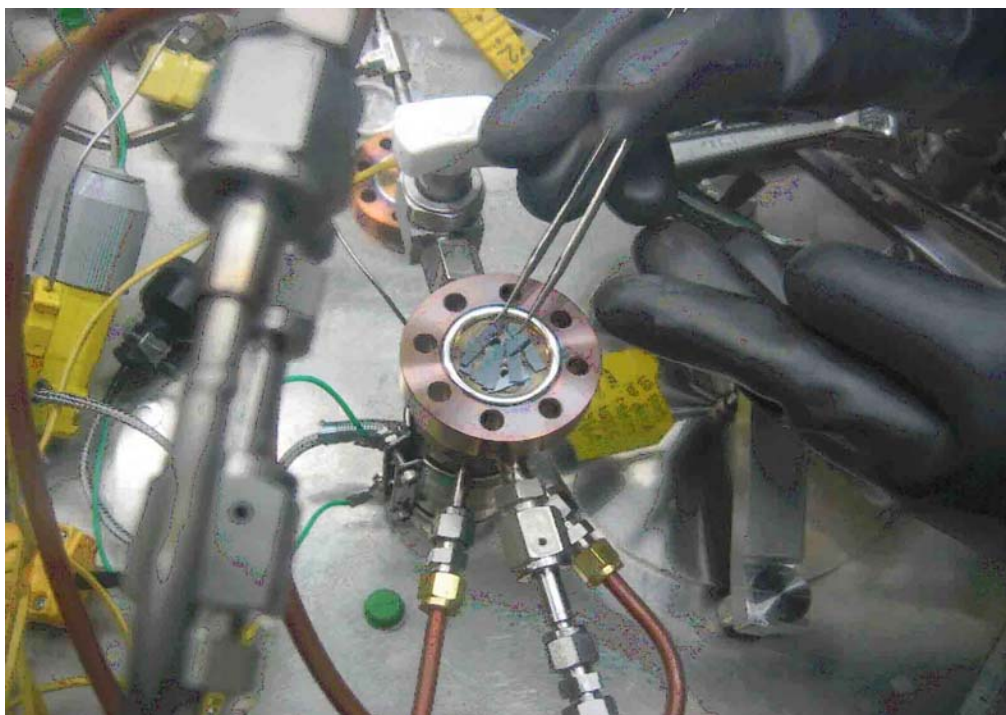


Figure 4.3 Photograph of samples within the high pressure, high temperature exposure apparatus as it rests within the glovebox. [47]

If no gross leaks are apparent the apparatus's valve is once again opened to the process loop's vacuum system and the cooling of the molecular sieve is initiated by flowing liquid nitrogen through the annulus region of molecular sieve container. The exposure begins by transferring tritium from the uranium storage bed to the cryogenically cooled molecular sieve trap. If the maximum pressure is desired the majority of the inventory is transferred to the cooled molecular sieve. The tritium pressure above the molecular seive is approximately two atmospheres when the exposure apparatus is isolated from the supply bed. At valve closure the flow of liquid nitrogen is stopped and the molecular sieve is allowed to warm to room temperature resulting in the release of all the adsorbed tritium. Figure 4.4 illustrates the rise in the exposure pressure when the liquid nitrogen flow is turned off. The final pressure boost, approximately a factor of two, is achieved through the heating of the exposure apparatus to the test temperature, see Figure 4.4.

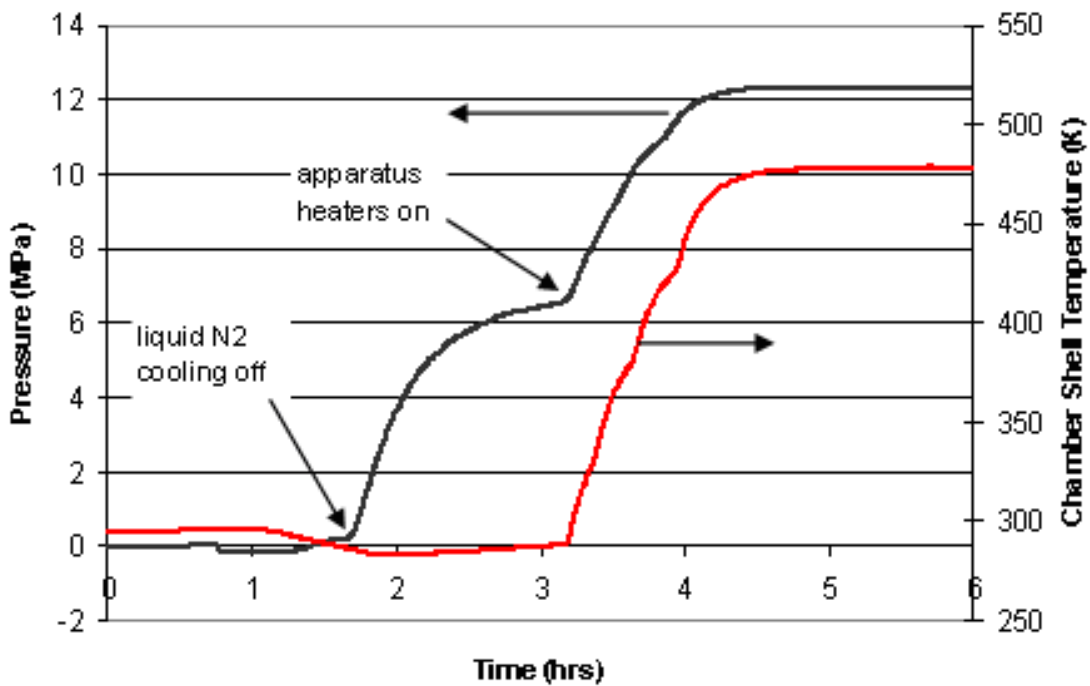


Figure 4.4 Pressure and temperature profile during the pressurization step. [47]

Typical tritium exposure duration ranged from 2 hours to 10 days. Following the tritium exposure, the heaters are turned off and the apparatus is allowed to return to room temperature gradually. Upon reaching room temperature the valve to the supply bed is opened and the tritium re-absorbed into the uranium. Figure 4.5 illustrates the pressure variation as the exposure apparatus is cooled and when the isolation valve is opened.

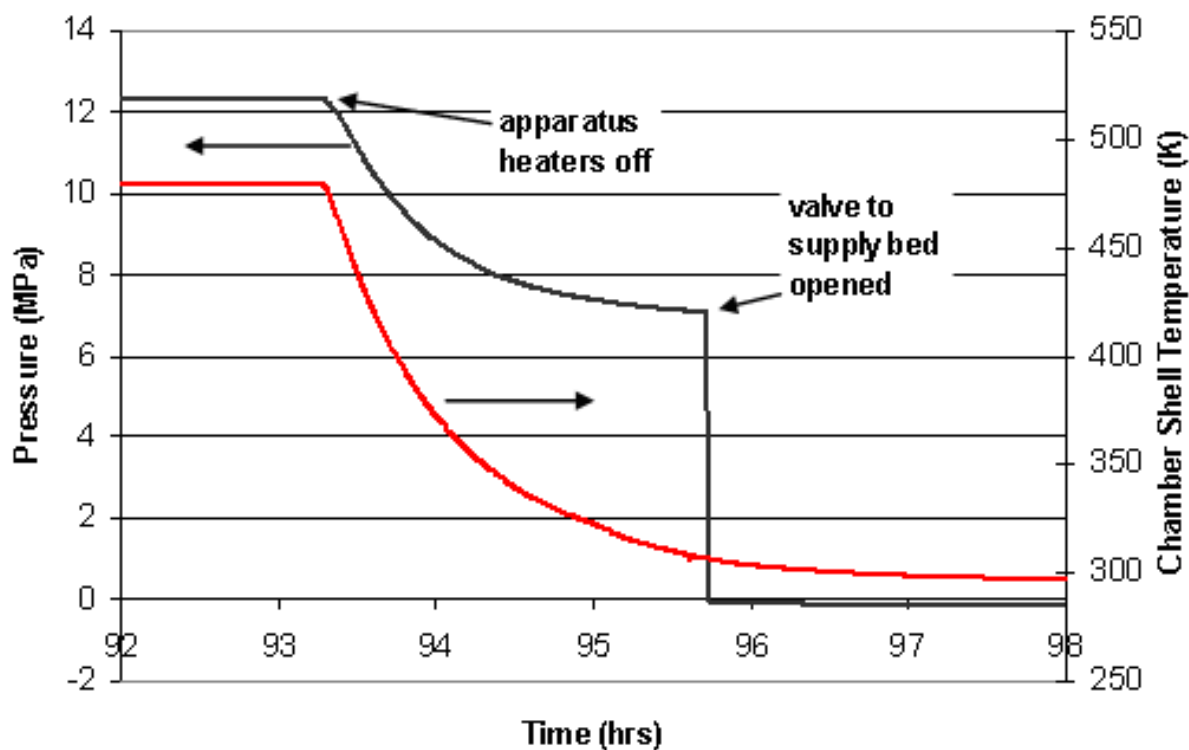


Figure 4.5 Pressure and temperature profile during the depressurization phase. [47]

4.4 SAFETY

A Job Safety Analysis (JSA) is performed prior to any work conducted in the Tritium Laboratory. This JSA, reviewed and signed off by all parties involved in the work, in conjunction with a Work Plan is required prior to the work being performed.

On a weekly basis urine samples are provided by personnel working on the project and the urine samples screened for tritium. If the worker has concerns that an unexpected exposure to tritium has taken place a urine sample is submitted no earlier than 4 hours after the exposure. The facility radiation safety officer is informed so that the tritium analysis can be given priority.

A tritium-in-air room monitor, set to alarm if the laboratory tritium concentration exceeds $10 \mu\text{Ci}/\text{m}^3$, is used to warn personnel of tritium leakages from the ventilated or sealed processed loop. Additionally, a hand-held Scintrex monitor is available to measure tritium-in-air concentrations locally.

The dominant tritium uptake (HTO) paths for personnel working in this project are expected to be skin absorption or inhalation while the arms are operating in the glovebox or samples are transferred out of the glovebox. Skin absorption is mitigated by using a lab coat in conjunction with sleeve protectors and double gloves. Inhalation of tritium is mitigated by utilization of a ventilated trunk line.

The maximum quantity of gas expected in the test apparatus is ~ 2.5 litres at NTP. If the Helicoflex seal were to leak and the gas released into the glovebox it would represent an increase in glovebox pressure of $(500 + 2.5)/500 = 1.005$, a pressure increase of 0.5%; that is 500 Pa, 2

inches of water equivalent. This increase in pressure would not trigger the passive pressure relief mechanism resulting in the venting of the tritium inventory to the environment.

The sensitivity to tritium of the Cleanup System's ionization monitors permits early detection of leaks from the testing apparatus. On two occasions, as the liquid nitrogen cooling was stopped, and the tritium pressure rose so did the tritium concentration in the glovebox indicating a leaking seal. Leak detection at this early stage permitted quick action; the isolation valve to the supply bed was opened and the tritium rapidly reabsorbed.

During this work tritium emissions to the environment are minimized by the following methods. The pure tritium transfer work is conducted in a sealed glove box which is fitted with a glove box clean-up system. The glove box clean-up system controls the tritium concentration in the glove box through the use of two traps; a molecular sieve trap for the oxidized hydrogenic species and a Zr-Fe trap for the elemental hydrogen species. Additionally, residual tritium from the transfer loop, when evacuating the exposure apparatus, is absorbed on another Zr-Fe getter located on the exhaust port of the vacuum pump.

A compliance monitor records the tritium emissions to the environment from the tritium laboratory in real time and weekly through silica gel integrators.

4.5 SUMMARY

A tritium exposure apparatus has been designed and built for the purposes of generating a high-pressure tritium atmosphere at 523 K. The loading system consists of a uranium tritide storage bed, an intermediate tritium transfer chamber filled with 5A molecular sieve, and the sample

exposure chamber. The loading system resides in a sealed glovebox with a nitrogen atmosphere that is continually purged through a Glovebox Clean-up System. The tritium used in each loading experiment is approximately 6000 Ci or 22 TBq. The process entails transferring the tritium inventory from the uranium storage bed to the cryogenically cooled (77 K) molecular sieve chamber. The molecular sieve at liquid nitrogen temperature is capable of adsorbing tritium to densities of 290 Ci/gram at one atmosphere. At 523 K a maximum tritium pressure of 21 MPa is achieved. The system performs as expected and proved to be safe.

5.0 TRITIATION OF AMORPHOUS, CRYSTALLINE AND POROUS SILICON

5.1 INTRODUCTION

Silicon is the most widely used material in semiconductor devices and its fabrication and processing have been well established. It has been long used in energy conversion device, such as solar cells in form of crystalline and amorphous silicon. Tritium, was incorporated into hydrogenated amorphous silicon ($a\text{-Si:H}$) using a PECVD (plasma enhanced chemical vapour deposition) technique [6, 8]. This method, while practical, is relatively complicated. Here, the post-tritiation technique developed in this work provides a simple and versatile method to incorporate high-density tritium into various forms of silicon by exposing these to tritium gas. Stable and high-density tritium bonding in hydrogenated amorphous silicon ($a\text{-Si:H}$) and crystalline silicon ($c\text{-Si}$) structures was achieved.

Post-hydrogenation has been widely researched for passivation of amorphous silicon ($a\text{-Si}$) and $a\text{-Si:H}$. Hydrogen is incorporated into $a\text{-Si}$ and $a\text{-Si:H}$ by ion implantation or exposing the samples to monatomic hydrogen, hydrogen plasma and H_2 gas at high temperatures [49]. Post-deuteration has also been investigated, and it has been shown that there is no chemical difference between hydrogen and deuterium [49, 50]. Hydrogen has also been introduced into $c\text{-Si}$ using similar processes [51]. Considering that tritium is chemically identical to hydrogen and deuterium, it is expected that similar processes can also be used to incorporate tritium into amorphous and crystalline silicon thereby facilitating the integration of a radioisotope micro-

power source on-chip. It is commonly accepted that hydrogen diffusion in silicon is predominantly in the atomic form and that post-hydrogenation using molecular hydrogen gas typically begins with the dissociation of hydrogen molecules at the silicon surface. In void rich material diffusion of molecular hydrogen is possible [50]. It is expected that tritium dispersion will also proceed in a similar manner. However, given the radioactive properties of tritium it is expected that tritium incorporation may be self-catalyzed. Specifically, excitation, ionization, and dissociation of molecular tritium (T_2) by the energetic beta particles as well as the production of atomic tritium due to tritium decay in T_2 .

In contrast to the relatively large quantities of literatures on the effect of post-hydrogenation and post-deuteration [52], very few studies have involved post-tritiation. In this chapter, a comprehensive study of post-tritiated process in both crystalline and amorphous silicons is presented. These studies will be insightful to further clarify post-tritiation mechanism between tritium gas and silicon materials. From engineering perspective, this study will provide useful information on how tritium post-processing and tritium-based nuclear micro-engineering will impact silicon micro-electronics on-chip.

5.2 TRITIATED AMORPHOUS AND CRYSTALLINE SILICON

5.2.1 Sample Preparation, Tritiation and Characterization

The crystalline silicon used here is the commercially available crystalline silicon wafer. The *a*-Si:H films were deposited on crystalline silicon substrates by a dc saddle-field glow discharge

PECVD system which has been described elsewhere [8, 23, 53]. The precursor gas used in the depositions was silane (SiH_4). The depositions reported here involved the flow of pure silane gas through the glow discharge chamber at 15 sccm each and a chamber pressure of 160 mTorr, anode potential of 530-650V, current to the anode of 17.5 mA, substrate at ground potential, and ion current to substrate of 0.6-1.0mA. The substrate temperature, time duration of the deposition, thickness of the film and hydrogen concentration of those α -Si:H films are listed in Table 5.1.

TABLE 5.1 Substrate temperature, time duration of the deposition, thickness and hydrogen concentration in the α -Si:H films.

Sample	BL1	BL2	BL3
Substrate Temperature	200 °C	115 °C	315 °C
Duration of Deposition	3 h	5 h 15 min	5 h
Thickness of Film	0.3 μm	0.6 μm	2.0 μm
Hydrogen Concentration	20%	35%	17%

In order to test the tritium pervasion in various forms of silicon, samples of silicon were exposed to tritium gas at temperature of 100–250 °C and pressure of 2–120 atm with time duration of 20 hours to 132 hours. Tritium effusion experiments were conducted in order to determine the atomic concentration and its bonding characteristics [53, 54]. A time-of-flight secondary ion mass spectroscopy (SIMS) measurement was carried out to resolve the depth

profile of tritium in silicon samples using Cs^+ sources. With the total atomic concentration found by effusion measurement, the SIMS profiles were carefully quantified. The depth resolution of SIMS is ~ 0.2 nm. The diffusion coefficient of tritium was derived from the tritium profiles.

5.2.2 Thermal Effusion

Unlike conventional hydrogen effusion experiments requiring ultra-high vacuum and mass spectrometer systems, tritium effusion experiments are carried out by measuring the evolution of tritium in an argon-filled ionization chamber. A schematic of the principle of tritium effusion monitoring is shown in Figure 5.1. Tritium effusion experiments are carried out in a modified ionization tritium monitor [55]. Tritium effusion monitor consists of three regions: the sample holder, the ion-precipitator, and the ion chamber proper. The sample holder consists of a copper crucible, heated with a boron-nitride coated graphite heater, and two thermocouples, one in the copper crucible close to the sample and the other on top of the crucible. The ion-precipitator consists of three grids, each with $\sim 70\%$ open area, between the sample holder and the ion chamber. The ion-precipitator, with its outer grids at ground potential and its central grid at 100 V dc, ensures that any gaseous species entering the ion chamber is electrically neutral. The ion chamber consists of a grounded cylindrical chamber, 1 L in net volume, and a collector which is held at -100 V dc. The electric field in the ion chamber separates ion pairs created by the deposition of tritium decay beta energy in argon. The electric field is sufficiently strong that all ions are collected and consequently the collector current is directly proportional to the number of tritium atoms in the ion chamber. The time derivative of the collector current is directly proportional to the rate of tritium effusion. Any error in the current signal due to ion-chamber-

surface adsorption effects is negligible given that the total current signal is several orders of magnitude greater than the background signal, and that surface memory outgassing effects for this monitor are small owing to the high polish of the internal surfaces of the chamber [55].

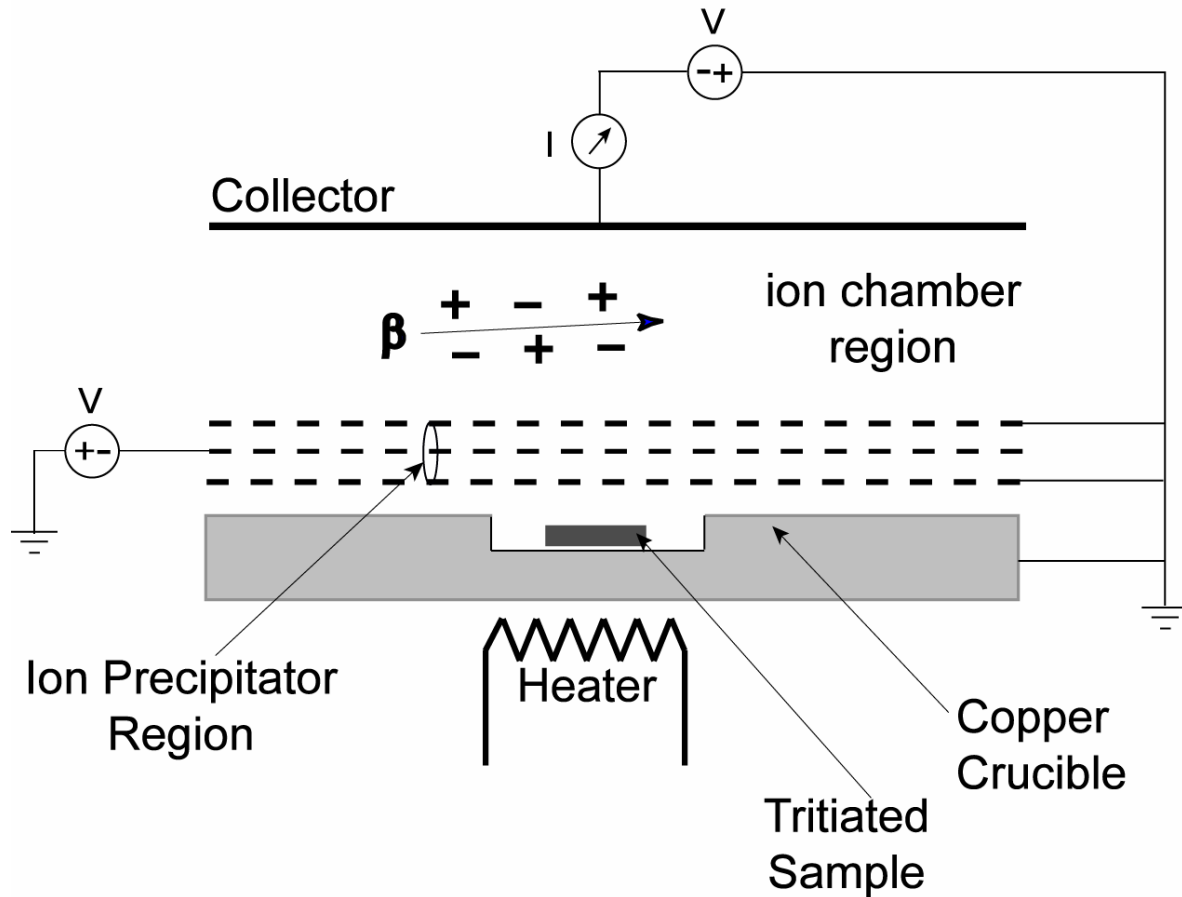


Figure 5.1 Illustration of tritium effusion monitor. [56]

A typical tritium effusion experiment involved placing an *a*-Si:H:T sample, approximately 1 mm² in size, in the copper crucible, establishing an argon purge, evacuating the chamber, and then back-filling the chamber with argon to 1 atmosphere. The sample is subjected to linear temperature ramping from room temperature to approximately 800 °C. Tritium effusion experiments were carried out at temperature ramp rates of 5, 10, and 20 °C/min.

The concentrations of hydrogen and tritium in the films are expected to be in proportion to the ratio of hydrogen and tritium in the discharge chamber [53]. The evolution of hydrogen and tritium from the films is to first order assumed to be in proportion to their concentrations in the films.

To gain comprehensive understanding on the high-pressure tritiation process, *a*-Si:H samples were deposited in various substrate temperatures, which yielded different hydrogen concentrations and bonding conditions. These samples were exposed in tritium gas for 84 hours at a temperature of 250 °C and a pressure of 120 atm. Thermal effusion measurements were then carried out to determine the tritium concentration and bonding characteristics. The tritium effusion profiles and tritium evolution rates as a function of temperature are shown in Figure 5.2(a) and (b); the latter were obtained by taking derivatives of tritium effusion profiles. It is shown that the profiles for all three samples deposited in different conditions are similar to each other. Tritium starts to effuse significantly above the loading temperature of 250 °C. Most of the tritium effuses out below 600 °C. The effusion rate was peaked around 400 °C for all three samples as shown in Figure 5.2 (b), which agrees with previous effusion studies on *a*-Si:H:T prepared by the PECVD process [6, 53, 54]. Gaussian deconvolution was employed to analyze the tritium evolution rate profile. An example is shown as an inset in Figure 5.2 (b), Table 5.2 lists the positions of two peaks and fractional areas of the tritium effusion peaks for all three tritiated *a*-Si:H samples. For all three samples, the low-temperature (LT) peak is located around 370 °C and the high temperature (HT) peak is centered around 500 °C. The LT peaks suggest the existence of high order silicon tritides and tritium clusters, and the HT peak could be attributed predominantly to the Si-T mono-tritide bonds [53, 57]. By comparing the fractional areas under both HT and LT peaks, it is estimated that around 70% tritium in *a*-Si:H films exists in forms of

high order silicon tritides and tritium cluster. Table 5.2 also lists the free energy ΔG associated with the low temperature (LT) peak; this will be discussed later. Despite identical tritium loading condition and similar effusion profiles, tritium concentration in three samples are significantly different. The effusion measurement yielded tritium concentrations of 3.3, 1.2 and 0.6 mCi/cm² for samples BL1, BL2 and BL3 respectively. The *a*-Si:H film deposited at 200 °C has the highest tritium concentration after the tritium exposure. These measurement results indicate that the hydrogen concentration in *a*-Si:H films has negative impact on the tritiation process.

TABLE 5.2 Tritium concentration, position of low temperature and high temperature peaks yielded by Gaussian deconvolution, fractional areas of the peaks, and the free energy of desorption for films BL1, BL2 and BL3 tritiated in tritium gas for 3.5 days at a temperature of 250 °C and a pressure of 120 atm.

Sample	Tritium Concentration (mCi/cm ²)	T (°C) LT ^b Peak	T (°C) HT ^a Peak	A _{LT} /A _t ^b	A _{HT} /A _t	ΔG (eV) for the LT peak
BL1	2.8	370	500	0.74	0.26	2.6
BL2	1.2	374	520	0.68	0.32	3.0
BL3	0.6	377	472	0.76	0.24	4.0

a. LT: low temperature; HT: high temperatures

b. A^t: Total area under the peaks

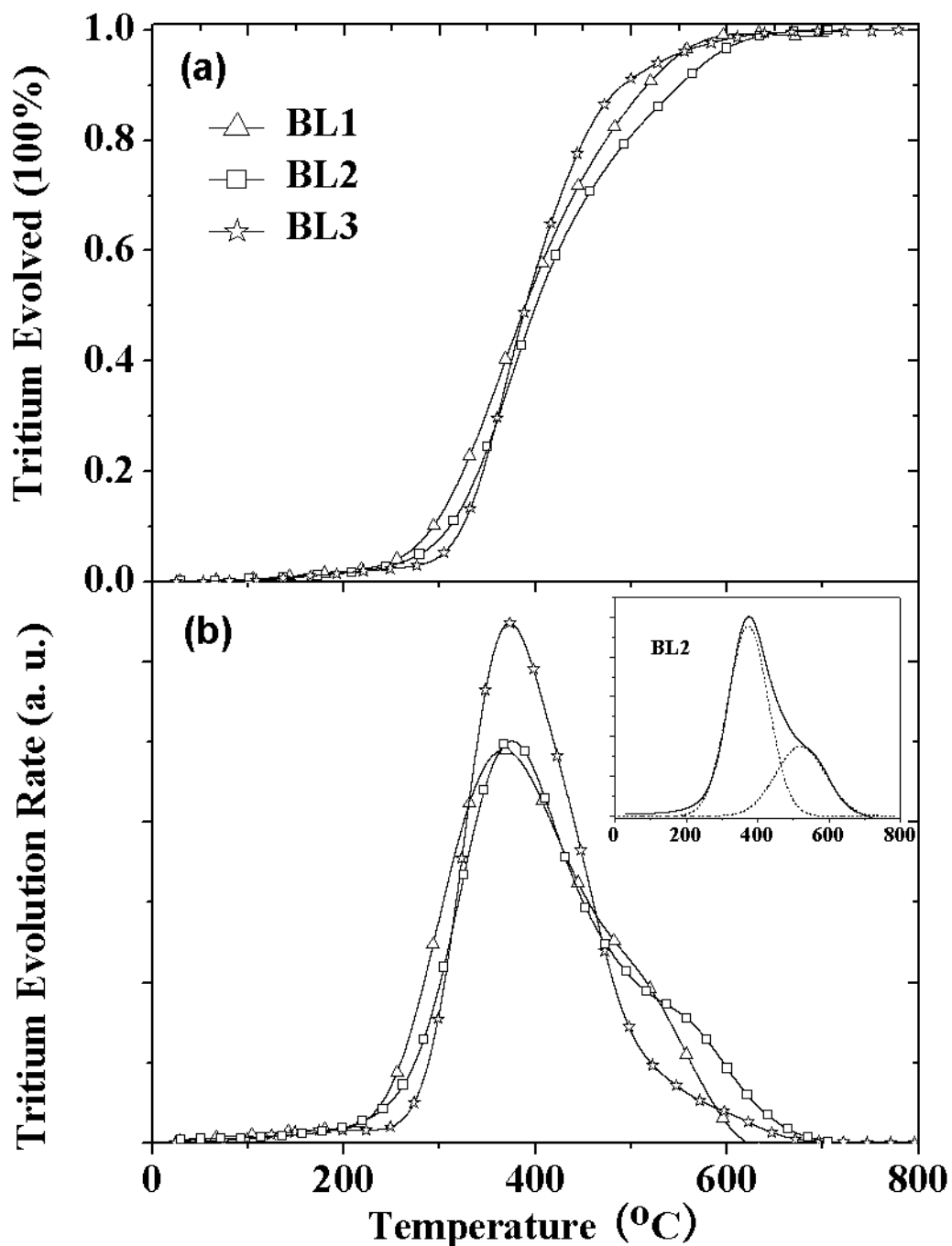


Figure 5.2 (a) Total tritium effusion from tritiated *a*-Si:H films, and (b) tritium effusion rate as a function of temperature for samples BL1, BL2 and BL3 tritiated in tritium gas for 3.5 days at a temperature of 250 °C and a pressure of 120 atm. The Gaussian deconvolution of BL1 is shown as an inset.

To study the influence of tritium exposure condition to the tritium concentration, sample BL1 were exposed in T₂ gas of various temperature and pressures. The spectra of tritium effusion and evolution rate are shown in Figure 5.3 and related data is listed in Table 5.3. Despite drastically different exposure conditions, there is no significant difference in the total tritium absorbed in the film under different tritium pressure and temperature. Slightly less tritium was measured for samples tritiated in the higher temperature of 250 °C, probably due to a stronger surface desorption effect at higher temperature. From samples loaded at lower temperature at 100 °C, tritium starts to effuse at lower temperature. Gaussian deconvolution yields an extra peak at lower temperature (LRT) around 320 °C. It is indicative of molecular tritium trapped in voids and weakly bonded tritium near the surface [54]. The sample is deposited at a substrate temperature of 200 °C. There is no significant change observed in tritium concentration for samples tritiated in different pressures. It is generally believed that *a*-Si:H films, especially those grown at low substrate temperatures, contains some void fraction. In device-quality films voids are not interconnected and H is assumed to diffuse as atomic species through the bulk. Therefore, high pressure molecular tritium doesn't enhance the tritium pervasion in *a*-Si:H.

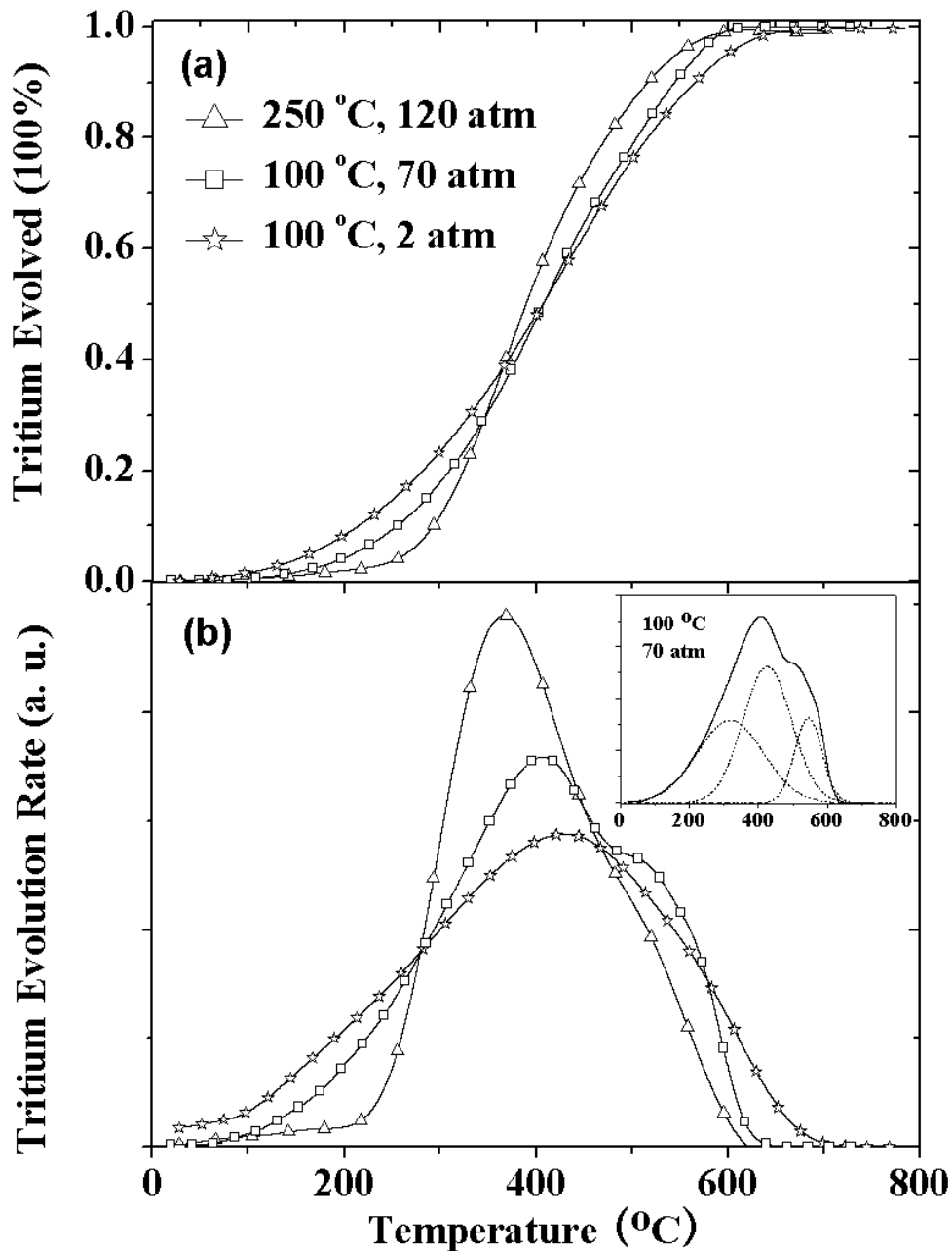


Figure 5.3 (a) Total tritium effusion from tritiated *a*-Si:H films, and (b) tritium effusion rate as a function of temperature for sample BL1 tritiated in tritium gas for 84 hours in various temperature and pressures. The Gaussian deconvolution of film tritiated at 100 °C, 70 atm is shown as an inset.

TABLE 5.3 Tritium concentration, position of low temperature and high temperature peaks yielded by Gaussian deconvolution, fractional areas of the peaks, and the free energy of desorption for film BL1 tritiated in tritium gas of various temperature and pressure for 3.5 days.

Sample	Tritium Concentration (mCi/cm ²)	T (°C)	T (°C)	T (°C)	A _{LRT} /A _t ^a	A _{LT} /A _t	A _{HT} /A _t	ΔG (eV)	ΔG (eV)
		LRT Peak	LT Peak	HT Peak				for the LRT peak	for the LT peak
250 °C, 120 atm	2.8	—	370	500	—	0.74	0.26	—	2.6
100 °C, 70 atm ^b	3.1	318	425	545	0.38	0.46	0.16	0.9	2.3
100 °C, 2 atm	3.3	322	458	572	0.55	0.39	0.06	0.6	1.8

a. LRT: lower temperature

b. Ramp rate: 20 °C/min; All others are 10 °C/min.

In order to study the relation between the tritium pervasion and the H concentration, *a*-Si:H, thermally annealed *a*-Si:H and crystalline silicon (*c*-Si) were exposed in tritium gas for 84 hours at a temperature of 250 °C and a pressure of 120 atm. The *a*-Si:H sample of BL3, which contains 17 at.% of hydrogen, was annealed in argon gas at 400 °C for 24 hours. The annealing process reduced the hydrogen concentration from 17 at.% to 6 at.%. Commercially available 500-μm thick *c*-Si wafer is used here as a reference with extremely tight lattice and almost no hydrogen content. Tritium effusion spectra are shown in Figure 5.4 and related data is listed in

Table 5.4. The annealed *a*-Si:H (BL3) absorbed slightly more tritium than the un-annealed sample. It is probably due to more dangling bond sites created by the out-diffusion of hydrogen during the annealing process. The effusion peak for the annealed sample also shifts to higher temperature and the fractional area below high temperature peak increased accordingly. This suggests an increased portion of tritium existed in Si-T mono-tritide forms. The annealing can also result in densification of the amorphous film with a tighter lattice configuration. This process might also suppress the formation of tritium clusters in matrix. As an extreme situation, tritium in *c*-Si is dominated by stably bonded mono-tritides as shown in Table 5.4.

TABLE 5.4 Tritium concentration, position of low temperature and high temperature peaks yielded by Gaussian deconvolution, fractional areas of the peaks, and the free energy of desorption for samples of *a*-Si:H, annealed *a*-Si:H and *c*-Si tritiated in tritium gas for 3.5 days at a temperature of 250 °C and a pressure of 120 atm.

Sample	Tritium Concentration (mCi/cm ²)	T (°C) LT Peak	T (°C) HT Peak	A _{LT} /A _t	A _{HT} /A _t	ΔG (eV) for the LT peak
<i>a</i> -Si:H ^a	0.6	377	472	0.76	0.24	4.0
<i>a</i> -Si:H annealed ^b	0.8	363	482	0.41	0.59	4.0
<i>c</i> -Si ^c	0.1	374	482	0.15	0.85	4.0

a. *a*-Si:H sample here is BL3;

b. *a*-Si:H annealed here is obtained by annealing BL3 at 400 °C for 24 hours.

c. *c*-Si here is commercially available silicon wafer.

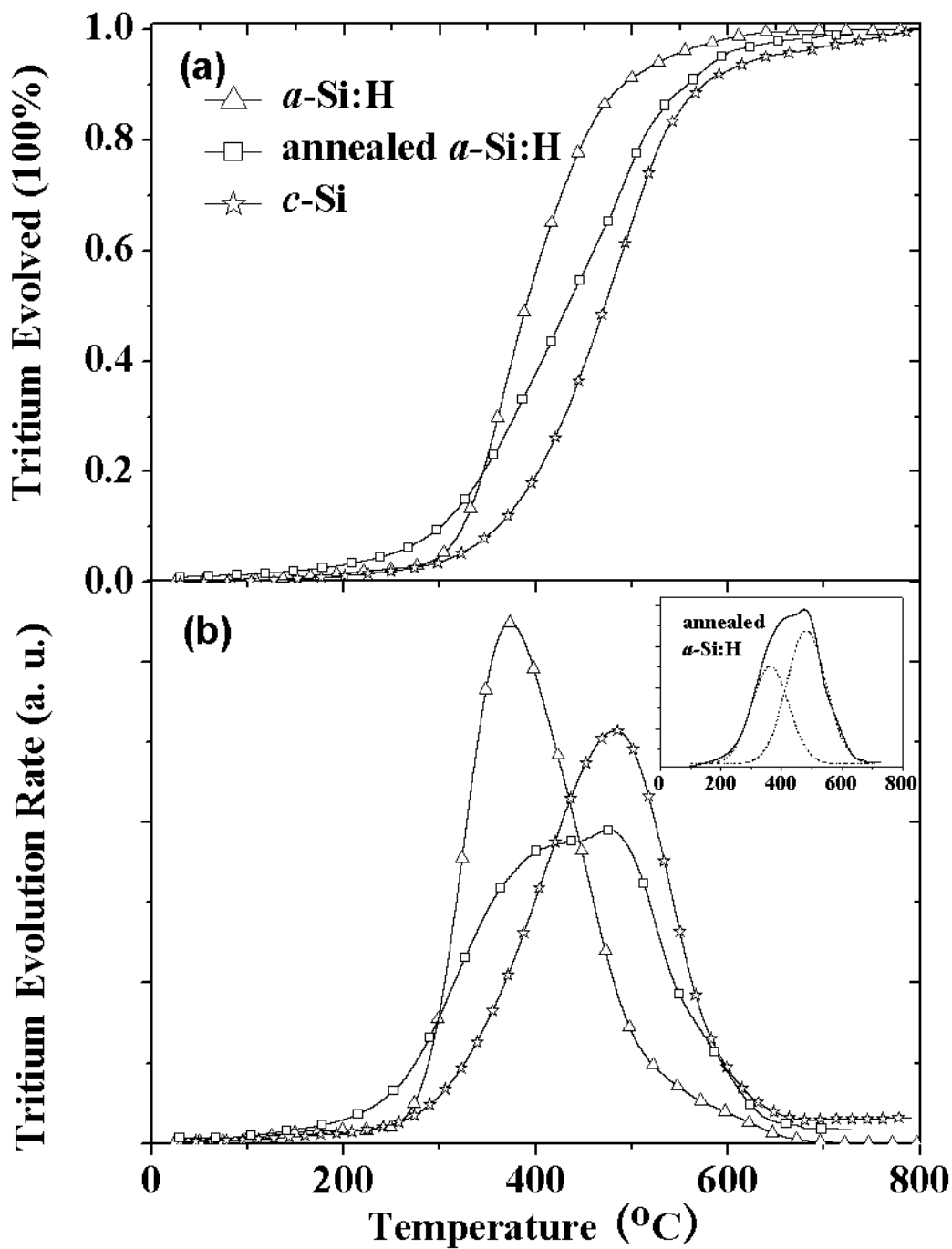


Figure 5.4 (a) Total tritium effusion from tritiated a -Si:H films, and (b) tritium effusion rate as a function of temperature for samples of a -Si:H, annealed a -Si:H and c -Si tritiated in tritium gas for 84 hours at a temperature of 250 °C and a pressure of 120 atm. The Gaussian deconvolution of tritiated annealed a -Si:H is shown as an inset

5.2.3 Fourier Transform Infrared Spectroscopy

Fourier Transform Infrared Spectroscopy (FTIR) is one of the most powerful tools for identifying chemical bonds in amorphous silicon materials by producing an infrared absorption spectrum like a molecular ‘fingerprint’. Structural information on the tritium in silicon was characterized using a Perkin Elmer 2000 FTIR spectrometer. IR spectra of samples were taken in the range 30-5200 cm^{-1} in the single-beam mode with a resolution of 2 cm^{-1} , in which the transmittances of the amorphous silicon film and a reference crystalline silicon substrate were measured and ratioed in rapid succession [58]. Since the mass of tritium atom (m_T) is heavier than hydrogen (m_H), the stretching frequencies of the Si-T bonds (ω_{Si-T}) can be calculated respect to the Si-H bond stretching frequency (ω_{Si-H}) as [58]:

$$\frac{\omega_{Si-T}}{\omega_{Si-H}} = \sqrt{\frac{m_H(m_T + M_{Si})}{m_T(m_H + M_{Si})}} \quad (5.1)$$

The infrared absorption spectra of the *a*-Si:H sample before and after the tritium exposure is shown in Figure 5.5. The vibrational spectra show a peak at 2000 cm^{-1} which corresponds to the Si-H stretching mode. The additional peak in the spectrum for the tritiated sample at ~1200 cm^{-1} corresponds to the Si-T stretching mode. This FTIR result is consistent with the reported vibrational spectra of *a*-Si:H:T prepared by PECVD [58].

After tritiation the peak intensity for Si-H stretching mode at $\omega_{Si-H} = 2000 \text{ cm}^{-1}$ decreases while the peak intensity Si-T stretching mode at $\omega_{Si-T} = 1200 \text{ cm}^{-1}$ increases [57]. It is noteworthy that the tritium quantity obtained from the FTIR spectrum is less than that of the effusion result; this suggests the existence of unbonded tritium, such as the free atomic tritium and molecular tritium in the *a*-Si:H film.

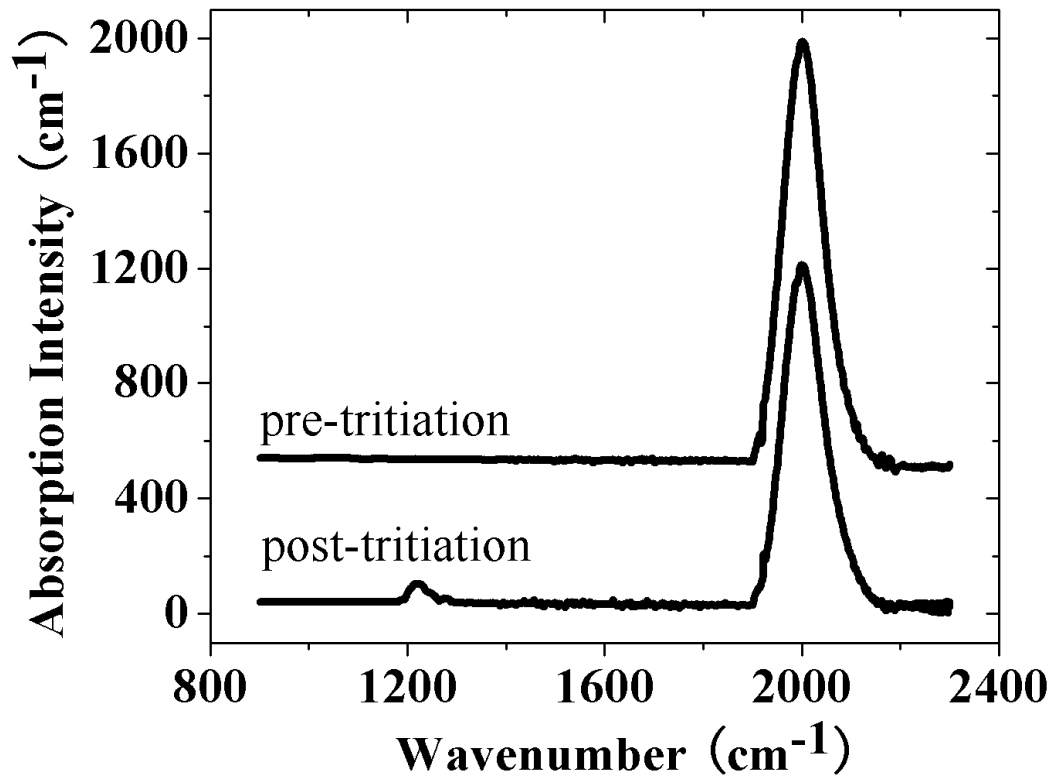


Figure 5.5 Absorption spectra of an *a*-Si:H film before and after tritium exposure. For clarity, the spectra of the *a*-Si:H before tritium exposure has been shifted up by 500 cm^{-1} [57].

5.2.4 Thermal Profiles

To study tritium diffusion profiles, SIMS measurements were performed on both *a*-Si:H films and *c*-Si wafers. Tritium concentration profiles of sample BL1 for hydrogen (H), tritium (T), and the total concentration of hydrogen and tritium (H+T) are shown in Figure 5.6.

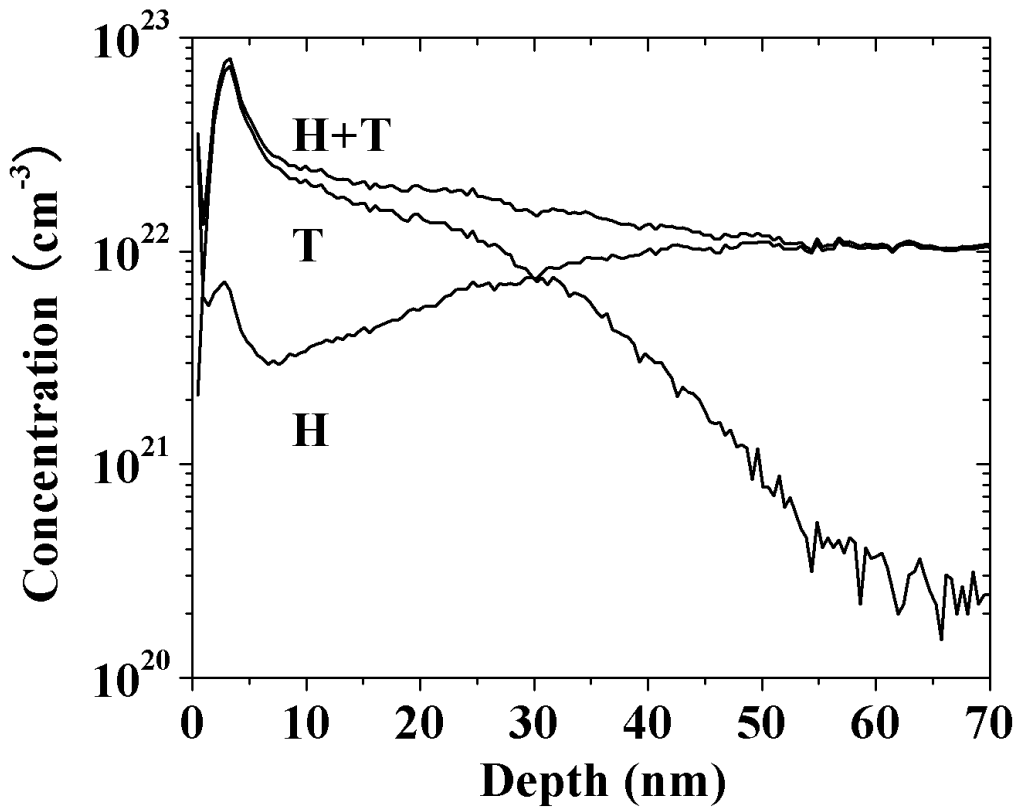


Figure 5.6 Hydrogen and tritium depth profiles of *a*-Si:H film BL1 obtained after an exposure to T₂ gas at 250 °C and 120 atm for 84 hours. The concentration profiles for H and T were measured simultaneously.

The *a*-Si:H films were exposed in T₂ gas at 250 °C, 120 atm for 84 hours. As shown in the figure, an extremely tritium-rich layer forms near the surface, the tritium concentration reaches $7 \times 10^{22} \text{ cm}^{-3}$ at a depth of 3 nm from the surface; it drops rapidly inwards at around $3 \times 10^{22} \text{ cm}^{-3}$ at around 6 nm deep. The tritium concentration then falls off at a slower rate into the sample. The H loss at the surface is about 2/3. The loss of H due to out-diffusion is over-compensated by the incorporation of T and a net increase of the hydrogen plus tritium concentration of $2 \times 10^{22} \text{ cm}^{-3}$ is

observed at a depth of 6 nm away from the surface. From this depth inwards, the diffusion profile can be described by a complementary error function (erfc). The diffusion length is related to the diffusion time t_d by [59]

$$x_0 = (4D_{eff} t_d)^{1/2}. \quad (5.2)$$

The diffusion length for T in-diffusion is approximately 50 nm (x_0). Therefore, a diffusion coefficient of $D_{eff} = 6 \times 10^{-17}$ cm²/s is obtained. This value is consistent with the reported result of plasma in-diffusion in *a*-Si:H [52] .

Figure 5.7 shows the hydrogen and tritium profiles of *a*-Si:H film of BL2 tritiated in tritium gas of 250 °C and 100 atm for 132 hours. The tritium concentration reaches 6×10^{22} cm⁻³ near the sample surface and drops rapidly to about 10^{21} cm⁻³ at 12 nm deep. The diffusion coefficient is calculated to be $D_{eff} = 2 \times 10^{-18}$ cm²/s. This value is over one magnitude order lower than that of BL1's. This is consistent with the effusion measurement that the concentration of BL2 is lower than BL1 in Table 5.2. It is also shown less hydrogen out-diffused from BL2 in comparison with that from BL1 sample. This is probably due to the reason that the hydrogen is bonded in a more stable form in sample BL2. FTIR spectrum, which is not presented here, also indicates that hydrogen in this film is mostly bonded in mono-hydride form.

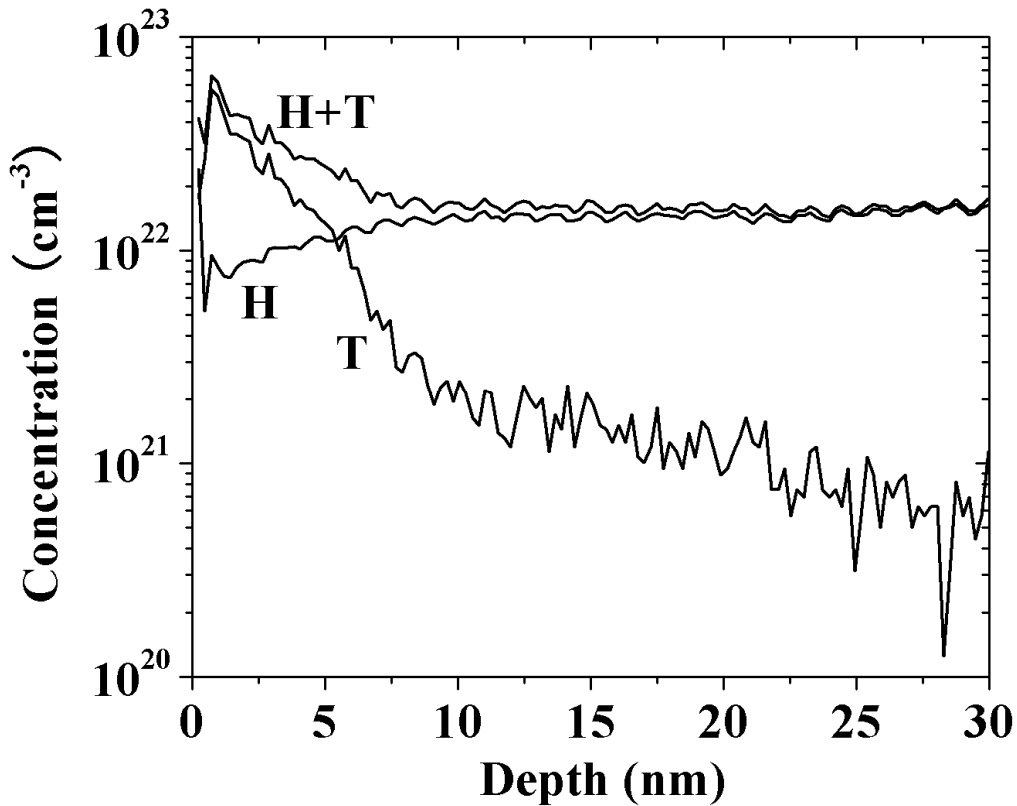


Figure 5.7 Hydrogen and tritium depth profiles of *a*-Si:H film BL2 obtained after an exposure to T₂ gas at 250 °C and 100 atm for 132 hours. The concentration profiles for H and T were measured simultaneously.

Figure 5.8 shows the hydrogen and tritium profiles of *c*-Si tritiated in tritium gas of 250 °C and 100 atm for 132 hours. A tritium concentration of 8 at.%, a number density of $4 \times 10^{21} \text{ cm}^{-3}$, is shown around the surface and it drops fast with depth. The concentration drops to 10% of the surface concentration at ~5 nm deep. The diffusion coefficient is calculated to be $D_{eff} = 5 \times 10^{-19} \text{ cm}^2/\text{s}$. Tritium is located at the superficial surface of the *c*-Si. The tight lattice of the *c*-Si has prevented the tritium pervasion in it.

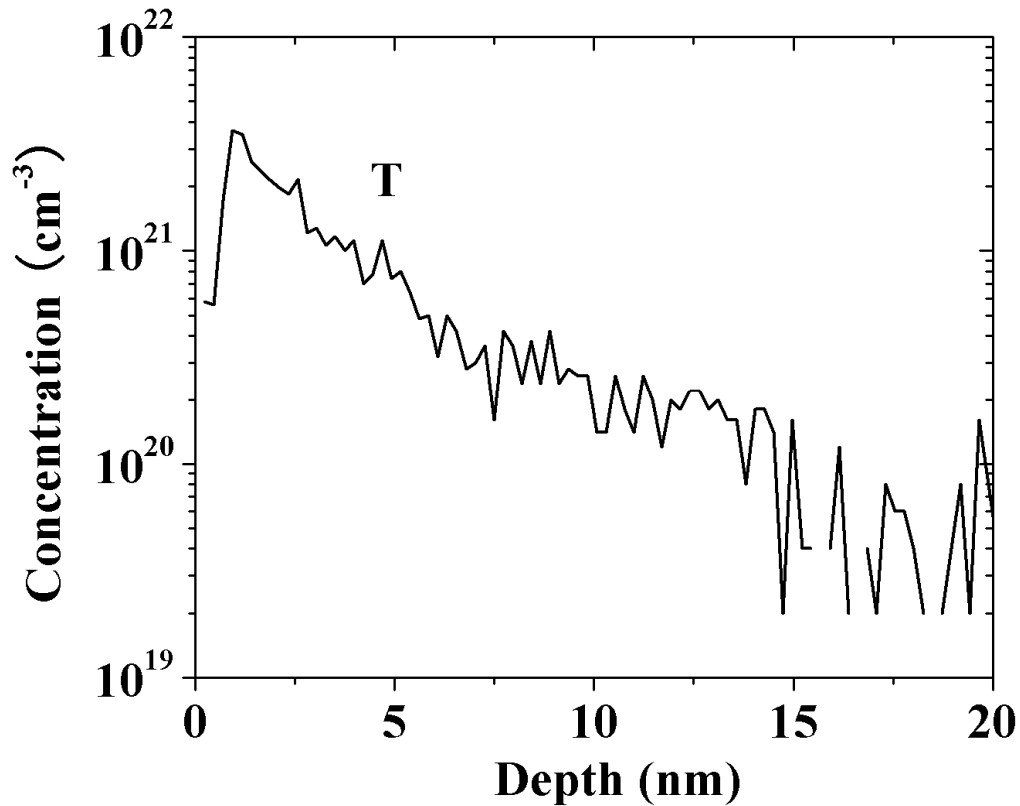


Figure 5.8 Hydrogen and tritium depth profiles of crystalline silicon obtained after an exposure to T_2 gas at 250 °C and 100 atm for 132 hours. The concentration profiles for H and T were measured simultaneously.

5.2.5 Discussion

5.2.5.1 Tritium Diffusivity and Solubility in Amorphous and Crystalline Silicon

In the reported literatures, studies of hydrogen solubility in *a*-Si were performed by rich deuterium (D) source layer diffusion or post-hydrogenation/deuteration with plasma/monoatomic hydrogen treatment or ion implantation. In the D diffusion and plasma/monoatomic hydrogen

treatment, hydrogen solubility of 1–3% was observed [50, 60]. At such low concentration level, the weak Si-Si bonds and dangling bonds seem to provide sites for H incorporation without dilatation of the Si network; the solubility depends on the micro-structure which, in turn, depends on deposition conditions. In the ion implantation process, the hydrogen incorporation proceeds simultaneously with the defect creation, a higher H concentration can be achieved than the initial H concentration. A hydrogen solubility limit of about 15-16% was reported in *a*-Si:H prepared by PECVD [61]. In this work, a much higher tritium concentration is observed from SIMS measurement; ignoring the ultrahigh tritium layer near the surface, a stabilized tritium concentration of $3 \times 10^{22} \text{ cm}^{-3}$ is achieved, which is equivalent to a tritium to silicon ratio of 3:5. This differs much from the previous results of post-hydrogenation and post-deuteration. Apparently, there are more Si bonds broken and more space provided for tritium to fit in. Given the radioactive property of tritium, the solubility of tritium in silicon is catalyzed by the beta radiation.

In order to maintain a plasma or mono-atomic hydrogen environment, the post-hydrogenation is commonly done in a very low pressure, ~1-2 Torr [49, 62]. While in the work, the pressure is much higher, ranging in 1.5-90 kTorr. The tritium concentration in materials that dissolve atomically will have a one-half power dependence on tritium pressure while those that dissolve molecularly will have a pressure dependence of power one.

$$C_H = S_H P^{1/2} \quad (5.3)$$

$$C_{H_2} = S_{H_2} P \quad (5.4)$$

It is commonly believed that hydrogen diffuses atomically in silicon. While the *a*-Si:H oxidizes upon exposure to air at a rate which depends on the microstructure of the film. Typical oxide layer thickness is 5-10 Å after a few days of exposure in air [30]. Silicon oxide has a

sparse lattice which allows diffuse of small molecules, like hydrogen. Equations (5.3) and (5.4) are hard to hold at the high concentration observed in this work; this is indicated in Table 5.3. While the surface area of the *a*-Si:H is affirmably believed to be dominated by the tritium once it is exposed in the tritium gas. In the tritium exposure system, there is about 1 cm thick T₂ layer above the silicon sample in the exposure chamber. Beta particles emitted from tritium decay can travel up to 35 mm in tritium gas at one atmosphere. The average range of the beta particles in silicon decreases with the increasing of the tritium pressure accordingly. Only half of the beta particles emitted from the tritium layer are able to reach the silicon due to the geometry. Among the other half, part of the energy will be lost in the gas due to some processes, such as tritium ionizing and dissociation. If 10% of the electrons can reach the silicon, the intensity corresponds to a flux of

$$\Phi = 10^{10} \text{ cm}^{-2} \text{ s}^{-1} \quad (5.5)$$

electrons striking the sample. Two effects are expected to occur due to the beta radiation. Firstly, the electron bombardment excites the silicon surface and makes it chemically active to the ionized or dissociated tritium. Thus tritium can be absorbed at the sample surface. Secondly, the beta radiation provides more space for tritium to fit in the silicon material. Electrons with keV energies are unlikely to produce atomic displacement in silicon.[44] While the silicon oxide, which has an amorphous structure, tends to embrittle and potentially fracture under beta radiation due to the reduction of the oxide bonds. Thus, the tritium can build up in the oxide layer with time. This explains the ultra high tritium layer near the material surface. For the beta particles impinged into the material, they lose energy in collision with the electrons in the material and produce an extremely large density of e-h pairs in their tracks. In case of *a*-Si:H, a pair is created for every 4.3 eV [63]. Electrons of 5.7 keV can travel about 0.17 μm in average and produce

about 1300 pairs. As the statement of hydrogen collision model, the e-h pair recombination breaks Si-H bonds to produce mobile H and DBs (dangling bonds) [64]. Less energetic electrons will lose energy more rapidly and more energetic electrons will lose it more slowly. The energy-loss profile drops rapidly with depth and the effective acting depth for electrons with energy of ~ 5 keV is around 50 nm in *a*-Si [65]. In this depth, extra DBs will be created and provide more room for the hydrogen (tritium) to fit in. In fact, a series of physical and chemical processes happen in this tritiation process, which include surface adsorption, dissociation, dissolution, diffusion, recombination, and desorption. It is speculated that a few factors may contribute to the increase in the tritium concentration, for example plasma treatment with annealing process is reported to increase the hydrogen concentration[61]; in our tritium exposure, it is also an annealing process simultaneously. In addition, high concentration of tritium is accumulated near the surface and the movement of such large amount of tritium in the silicon network may also contribute to break some weak silicon bonds and therefore provides more tritium to fit in. To further clarify the tritiation process, further investigations are needed to be carried out.

While the diffusivity seems to be not enhanced much by the beta radiation, similar diffusion coefficient is obtained as that of reported post-hydrogenation/deuteration experiments. Except the ultrahigh tritium layer near the surface, the tritium diffuses as the hydrogen/deuterium behaves. The *a*-Si:H deposited at substrate temperature of 200 °C displayed the rapidest tritium diffusion and in result of the highest tritium concentration. This seems to be due to a balance of the lattice tightness and initial hydrogen concentration. The film deposited at high temperature may result in a tight lattice; a low temperature deposition results in a high hydrogen concentration and the isotope exchange seems not to play a significant role in the tritiation process.

5.2.5.2 Energy Energetic and Network Stability of Tritiated Amorphous and Crystalline Silicon

The Gaussian deconvolution of the effusion rate profiles illustrate two peaks for silicon tritiated at high temperature (250 °C), one low temperature peak and one high temperature peak. The low temperature peak (LT) is around 370 °C and the high temperature (HT) one around 500 °C. Silicon tritiated at low temperature (100 °C) yields an extra lower temperature (LRT) peak located around 320 °C.

The low temperature hydrogen effusion is usually considered to be limited by surface desorption process, then it can be represented by the following surface desorption rate equation:[54, 66, 67]

$$\frac{d\left(\frac{N}{N_0}\right)}{dt} = \left(\frac{kT}{h}\right) \left(1 - \left(\frac{N}{N_0}\right)\right)^n \exp\left(-\frac{\Delta G}{kT}\right) \quad (5.6)$$

where N and N_0 represent the hydrogen evolved from the sample and the initial hydrogen in the sample, respectively, T is the sample temperature, n is the reaction order which is 1 or 2, ΔG is the free energy of desorption. Applying this rate equation to both the LT and LRT peaks by

plotting $\ln\left(\frac{d(N/N_0)}{dt} \left(\frac{kT}{h}\right)^{-1} \left(1 - \frac{N}{N_0}\right)^{-n}\right)$ as a function of $1/T$ results in a straight line for $n = 1$,

which indicates that the desorption reaction is a first order rate process. The calculated free energies are listed in Table 5.2-4. The free energy associated with the LRT peak is 0.6–0.9 eV. Given that the migration energy of free hydrogen atom and H₂ in silicon is around 0.5 -1 eV,[52] the LRT peak is attribute to the effusion of free atomic tritium and molecular tritium, as well as the shallowly trapped and tritium near the surface in the film. The free energy associated with the

LT peak is 1.8–4 eV. The surface absorption of hydrogen involves the simultaneously rupture of two neighboring Si-H bonds and formation of H₂. Considering the hydrogen bonding energy E_{H-H} of 4.5 eV, the silicon-tritium bond energy is calculated to be 3.15–4.25 eV. This is generally in agreement with the literature data.[52] Here, the mass difference between hydrogen and tritium is neglected. The range of energies suggests variation in the Si-T bonding environment. Higher activation energy of 4.0 eV is obtained for tritiated *a*-Si:H films deposited or annealed at high temperature (300-400 °C); in comparison, lower activation energy is found for film deposited at low temperature (100–200 °C). This suggests that the film morphology affects the tritium bonding in the post-tritiation process.

When hydrogen is introduced into the matrix above the solubility which is reported to around 3-16 at.%, a fundamental thermal instability of the alloy network occurs. With increasing hydrogen concentration, it is likely that the hydrogen will associate into molecular hydrogen. The existence of molecular hydrogen in silicon lattice was claimed by Raman measurement.[68] The LRT peak found in the effusion rate profile indicates an evidence of the tritium molecules. The molecular hydrogen can be effused by heating above 200 °C;[69] this is consistent with our experimental result that no LRT peak is found for silicon tritiated at 250 °C.

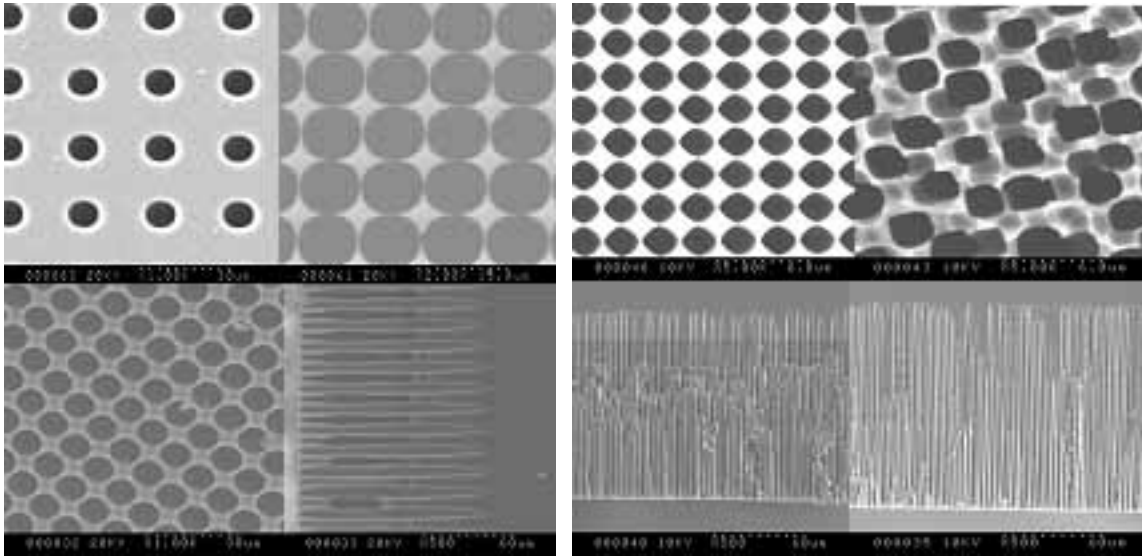
The influence of helium accumulation with tritium decay has not been investigated. Helium built-up with tritium decay may lead to the formation of bubbles, similar to that in metal tritides and in helium ion implanted silicon.[69, 70] The extent of bubble size and distribution will depend on various factors including the initial tritium concentration. It is expected that the effect of helium accumulation in amorphous and crystalline silicon will be quite different considering the inherent defect prone network of *a*-Si:H in contrast to the regular lattice of *c*-Si. One might expect the extent of lattice disruption and rearrangement to be small in *a*-Si:H in comparison to

c-Si. In fact, the tritiated amorphous silicon samples prepared using PECVD techniques show no evidence of blistering after more than 6 years of aging [8].

5.3 TRITIATED POROUS SILICON

The SIMS measurement shows that the tritiated crystalline silicon shows a surface effect that the tritium mainly immobilized around the surface of around 10 nm deep. Porous silicon, which has a large surface to volume ratio, is expected to absorb large quantity of tritium through the post-tritiation process. The high-pressure tritiations of *c*-Si were further studied on trenched *c*-Si and porous crystalline Si (*p*-Si). The trench *c*-Si were prepared by a deep reactive ion etching (DRIE) process, *p*-Si were prepared using an electrochemical etching process. The DRIE process produced array of pores with diameter of 10 μm and depth of 120 μm shown in Figure 5.9a. The spacing between adjacent pores was chosen as 10, 12, and 25 μm , which magnified the surface area by 33, 30, and 9 times respectively. The pore diameter of the *p*-Si was 2 μm and the depth was 150 μm shown in Figure 5.9b. The surface area was magnified by 120 and 180 times for random and ordered *p*-Si respectively. All DRIE-etched *c*-Si and *p*-Si samples were tritiated under the same condition as the planar *c*-Si. Effusion experiments were carried out right after the tritium loading. Figure 5.10 shows the total tritium evolved from the samples versus their total surface areas, which includes the internal area of the pores. Despite different fabrication method, Figure 5.10 reveals a linear dependence of tritium occluded on the total surface area. Effusion experiments also indicated similar thermal stability of *p*-Si with that found in *a*-Si and *c*-Si

samples. This suggests a universal mechanism underling the bonding of tritium in silicon material under the high pressure loading.



a)

b)

Figure 5.9 SEM surface morphology and side views of a) deep-trenched crystalline silicon prepared by deep reactive ion etching and b) porous silicon prepared by electrochemical etching.

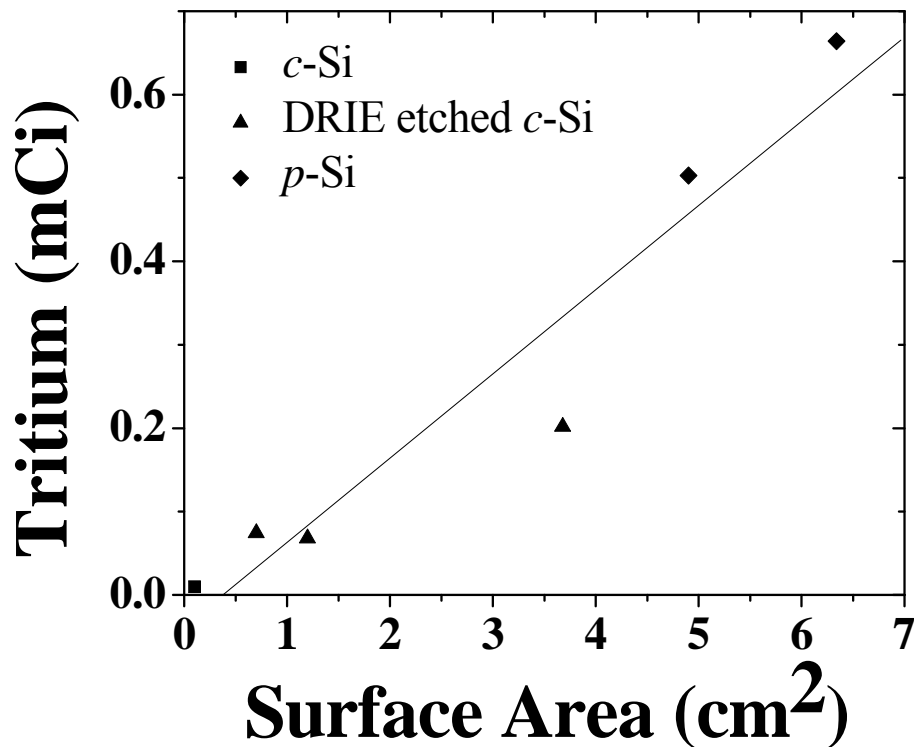


Figure 5.10 The total tritium occluded in crystalline silicon as a function of the total surface area. [57]

5.4 RADIOACTIVE SURFACE ACTIVITY OF THE TRITIATED AMORPHOUS, CRYSTALLINE AND POROUS SILICON

The surface activity measurement is performed by a surface activity monitor (SAM) which is illustrated in the inset of Figure 5.11. The SAM is based on gas ionization principle using parallel capacitor configuration[71, 72]. The source is mounted on one of the parallel plates and the high energy emitted electrons ionize the gas and create electron ion pairs. An external electrical

field is used to separate the pairs by applying a bias voltage. The ionization current as a function of the applied bias voltage is shown. The distance between the electrodes is 1 cm. The saturated ionization current is a measure of the effective surface activity of the tritiated sample.[72]. For the saturated current of 40 pA of the *c*-Si sample, the effective surface activity is estimated to be 0.04 mCi/cm^2 , or 40% of total concentration, close to 50% of theoretical limit, which provides an evidence of surface absorption of tritium in *c*-Si. In a contrast, the 300-nm tritiated *a*-Si layer only yielded 10% effective surface activity. Since the average range of 5.7 keV beta particles in silicon is less than $0.2 \text{ }\mu\text{m}$ [73], surface-absorbed tritium could be desirable to eliminate self-absorption of beta particles. The *p*-Si sample yields an ionization current of 2 nA/cm^2 . The surface activity measurement is also a demonstration of the tritiated *a*-Si:H as a cold electron source. The cold electron ionization sources based on tritiated Si are potentially amenable to a series of applications, such as on-chip micro-gas or micro-particle analyzers.

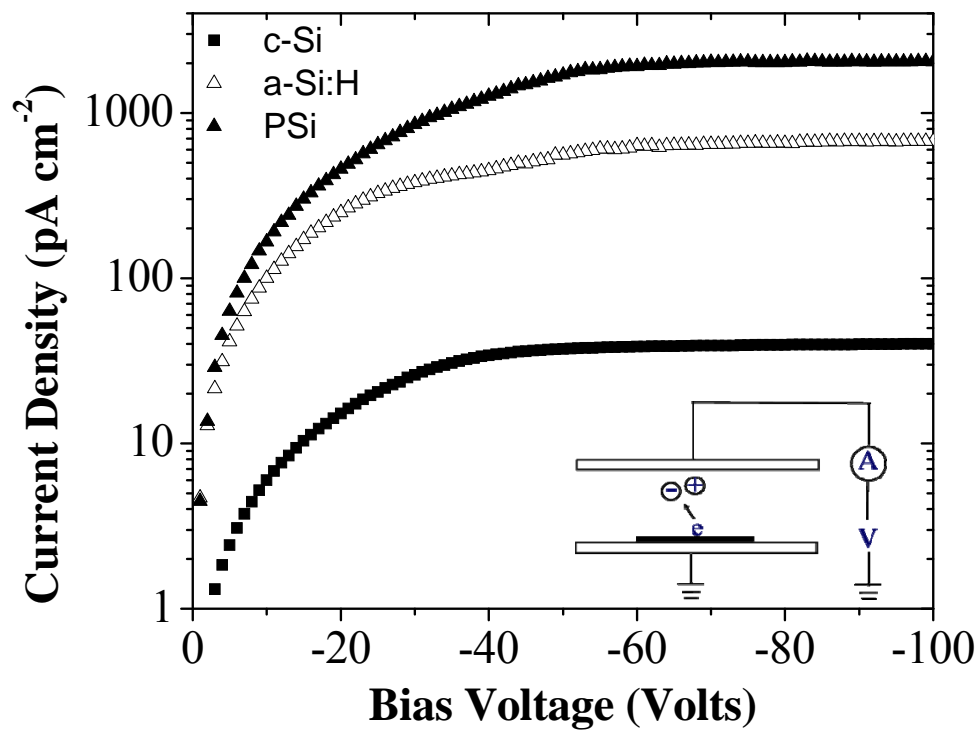


Figure 5.11 Ionization current induced by tritiated c-Si, a-Si:H, and p-Si samples per unit centimeter in air as a function of the bias voltage. The air gap is set at 1 cm.[57]

5.5 SUMMARY

In summary we demonstrate a simple and versatile method to stably incorporate tritium into various types of silicon using T_2 gas. The low-temperature post-tritiation process described in this work provides a convenient way to locally integrate a radioisotope micro-power source on-chip.

Tritium effusion technique is employed to study tritium evolution from *a*-Si:H films deposited and tritiated in various conditions. Gaussian deconvolution of tritium effusion spectra yields two peaks for *a*-Si:H films tritiated at high temperature (250 °C), one low temperature (LT) peak which is attributed to tritium cluster and weakly bonded tritium, and another high temperature peak (HT) which is attributed to the monotritides. The structure information is also confirmed by FTIR spectra. A lower temperature peak (LRT) was found for *a*-Si:H film tritiated at low temperature (100 °C) which is attributed to free tritium atom and molecular tritium trapped in voids, as well as shallowly trapped tritium near the surface of the film. The LRT and LT peaks appear to be surface desorption limited. The activation energy of 0.6-0.9 eV for LRT peak and 1.8-4.0 eV for the LT peak were derived. The Si-T bond energies range from 3.14–4.15 eV. Due to a much tighter lattice, *c*-Si absorbed less tritium than *a*-Si:H and the tritium solubility and diffusivity is much lower in *c*-Si than in *a*-Si:H. The concentration near the surface is 40% and 8% in *a*-Si:H and *c*-Si, respectively. This is much higher than the reported results in post-hydrogenation and post-deuteration. The solubility is enhanced by the electron bombardment due to beta-decay of tritium. The high energy electrons active the material surface, hasten the release of the mobile tritium and create dangling bonds; thus enhance solubility of tritium in silicon.

Tritium locked in silicon provides potentially a safe and localized on-chip energetic electron source for capacitor charging, MEMS cantilever actuation, molecular excitation and ionization, and for micro-nano power production amenable to a wide array of applications.

6.0 METAL TRITIDES AND CONTACT POTENTIAL DIFFERENCE BETAVOLTAICS

6.1 METAL TRITIDES

Since T. Granham's first observation of the absorption of the hydrogen in palladium in 1866, the behavior of hydrogen in metals has been studied very extensively.[74] The interest was motivated by the possible applications, such as moderator material in nuclear fission reactors, reversible hydrogen storage, and by the fact that metal hydrides show exciting physical properties (e.g., superconductivity, quantum effusion, phase diagrams, etc.) [75]. Many of those properties have been determined for the stable hydrogen isotopes H and D in various metals. A series of metals have been tested for tritides, such as nickel, scandium, magnesium and titanium.[9, 74, 76, 77] Scandium is chosen here to make the metal tritide in this research.

To produce high density tritium fuel, scandium film was deposited on silicon wafer substrate. The substrate was thoroughly cleaned. The Sc film was subsequently tritiated by exposing it to tritium gas of 250 °C. In the tritium gas, the scandium film absorbs tritium and immobilizes the tritium in the lattice. A scandium tritium alloy, scandium tritide, will form as ScH_x , where x is the scandium to tritium ratio. Thermal effusion, outgassing monitoring and surface activity measurement were performed to characterize of the scandium tritides. To study the stability of the tritiated ScT_x film, a thermal effusion measurement[53] was performed on a cleaved small sample. Typical effusion data showed tritium outgassing from the samples

beginning at approximately 250 °C, the tritium loading temperature, while the majority of tritium evolution peaked around 600 °C. Thermal effusion experiments also provided the concentration of tritium in the ScT_x film of 60 mCi/cm², which is equivalent to a tritium to scandium atomic ratio $x=1$. A 2 cm² ScT sample was also placed in the tritium effusion monitor, in ambient atmosphere, at room temperature for a week to monitor the long-term stability of tritium in the film. An average outgassing rate of less than 2 pCi cm⁻² s⁻¹, or 4.8×10^7 atoms cm⁻² s⁻¹ was obtained. Assuming that the outgassing rate is undiminished with time, it is equivalent to a tritium diffusion half-life of greater than 100 years, over 8 times the tritium decay half-life. The loss of tritium from the sample due to room temperature outgassing is negligible.

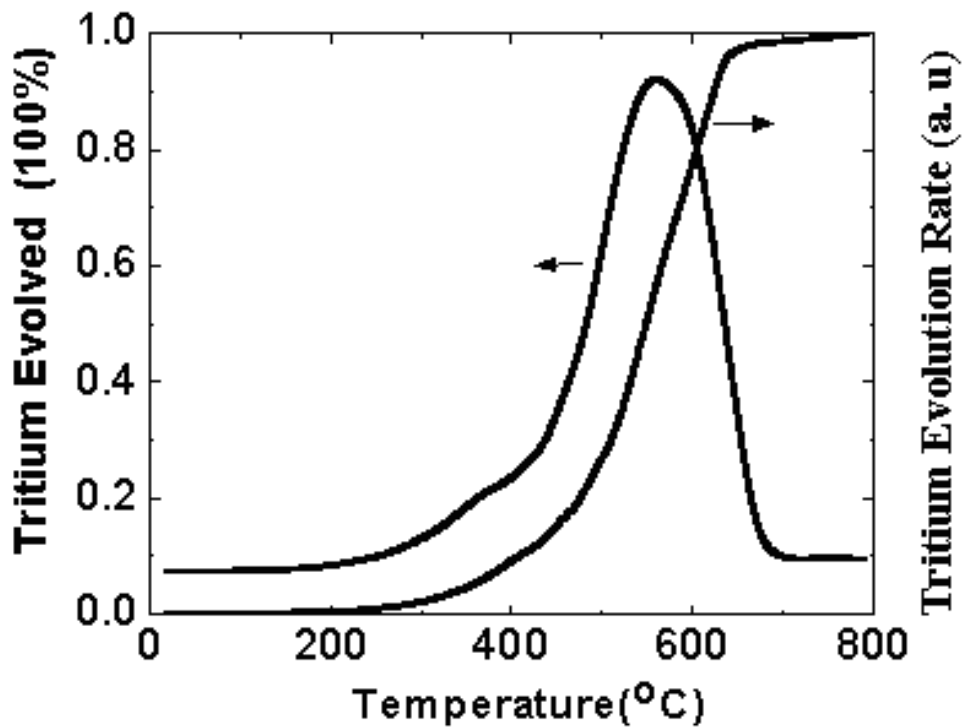


Figure 6.1 Cumulative tritium effusion and tritium effusion rate as a function of temperature for scandium film exposed to tritium gas at 250 °C.

The surface activity monitor (SAM) was used to characterize the effective surface activity available for ionization.[72] The ionization current density (J) as a function of the applied bias voltage at electrode gaps of 1, 2, 4 and 6 mm, is shown in Figure 6.2. The saturated current density is approximately 15 nA/cm². Using the average ionization energy in air of 33.75 eV per ion pair, the effective surface activity of the ScT film is estimated to be 15 mCi/cm², which is equivalent to an average energy (5.7keV) beta flux density of 90 pA/cm² or a power density of 0.5 μ W/cm². This scandium tritide film is useful in nano- to micro-watt betavoltaics [78].

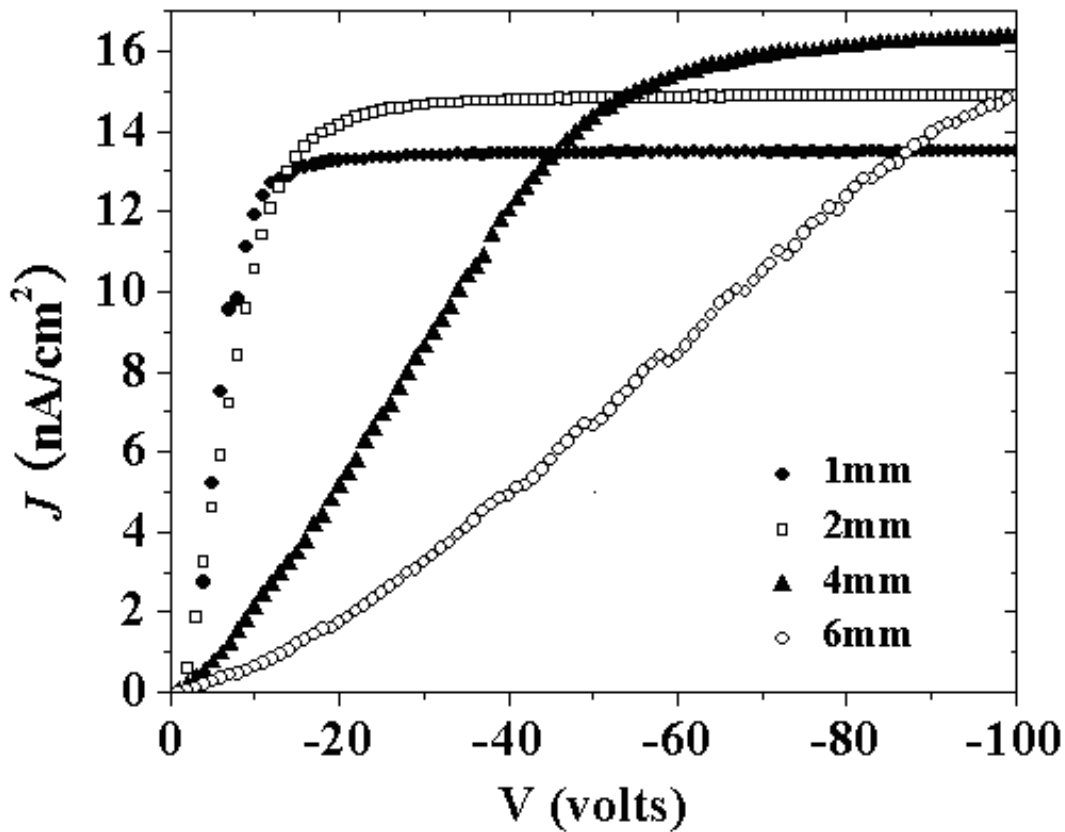


Figure 6.2 Ionization current density (J) due to the Sc:T film sample in air as a function of the bias voltage (V). The air gaps are set at 1, 2, 4, and 6 mm, respectively.[79]

6.2 BETAVOLTAICS USING CONTACT POTENTIAL DIFFERENCE

A series of studies have been reported on betavoltaics employing semiconductor *pn* junction using materials such as amorphous silicon,[6], textured silicon,[25, 26] porous silicon,[7, 27] silicon carbide[28, 29] and gallium arsenide/nitride[22]. The efficiency and longevity of these battery structures rely on high-quality *pn*-junctions, which are often susceptible to radiation damage and lack structural self-healing resiliency.

One simple method to convert the kinetic energy of radioemissions into electrical energy is to utilize a contact potential difference (CPD) device produced from metals with dissimilar work functions.[39] An appropriate dielectric medium, in the form of a thin film, gas or liquid, is sandwiched between two metal electrodes. An ionizing radiation source, dispersed within the dielectric medium or included in an electrode, provides the energy source for electron-ion pair generation. Charged carriers are separated by the built-in electric field, induced by the contact potential difference of the electrodes, and thus generating current in an external load. Figure 6.3 shows a schematic of the CPD betavoltaics cell. A CPD-based micropower source is relatively simple to implement and can be integrated for on-chip applications. Utilizing the scandium tritide film, the CPD betavoltaic batteries are constructed [79].

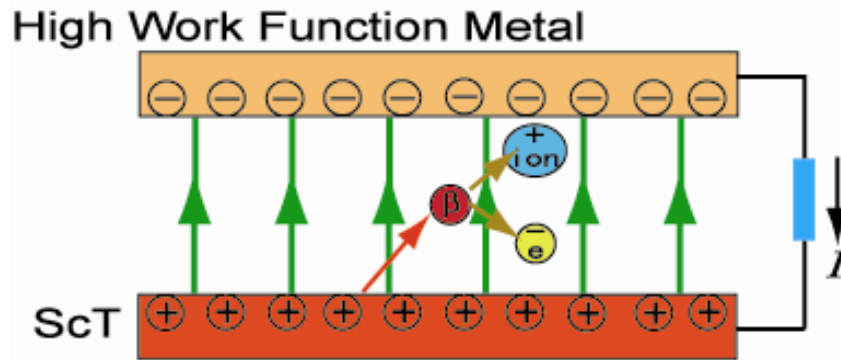


Figure 6.3 The schematic of the CPD Betavoltaic battery

6.2.1 Air-Medium CPD Betavoltaic

The air-medium CPD betavoltaic is constructed by the ScT film and the copper plate; the air works as the medium between them. The ScT film was used as the cathode, as well as the ionization source, while copper was used as the anode; the work functions of pure Sc and Cu are 3.5 eV and 4.7 eV, respectively. The active plate area was 2.5 cm by 1.3 cm, and the air gaps were varied from 0.05 to 3 mm.

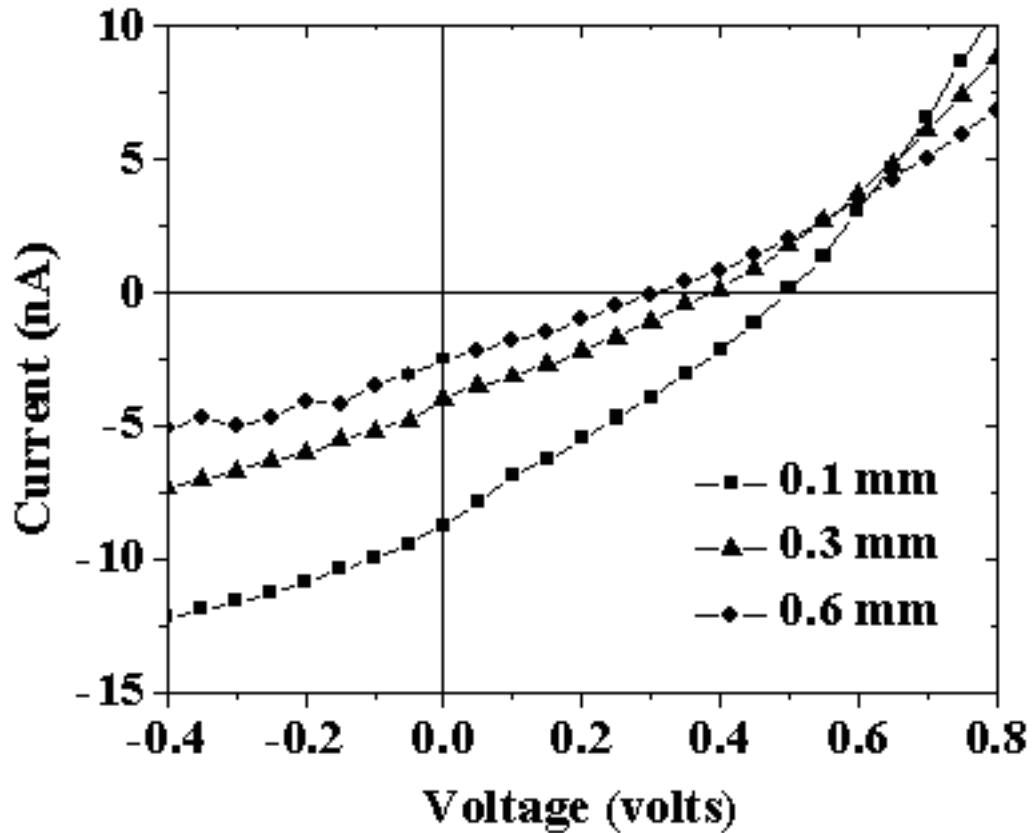


Figure 6.4 The IV characteristics of the CPD cell with a size of 2.5 cm by 1.3 cm at the electrode distances of 0.1, 0.3 and 0.6 mm in air.[79]

A Keithley 617 electrometer was used to measure the voltage and current. The measurement was carried out at room temperature and standard pressure. The IV characteristics of the CPD cell at electrode distances of 0.1, 0.3 and 0.6 mm are shown in Figure 6.4.[79] An open circuit voltage (V_{oc}) of 0.5 V and a short circuit current (I_{sc}) of 8.73 nA, which is equivalent to a short circuit current density of 2.67 nA/cm² (18% of the saturation current in Figure 6.2.), were measured at a distance of 0.1 mm. The maximum power point yields 1.3 nW (0.4 nW/cm²) which corresponds to a fill factor of 0.3. The current might be improved by using gas with higher pressure or lower ionization energy such as argon.

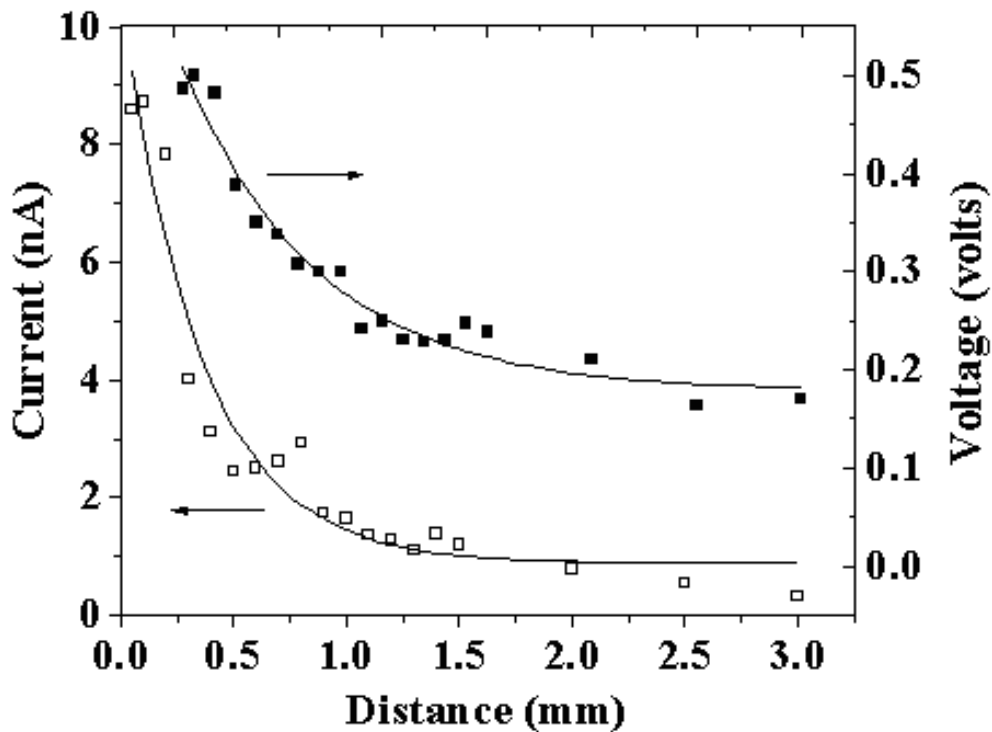


Figure 6.5 The short circuit current (I_{sc}) and the open circuit voltage (V_{oc}) as a function of the electrode distance (d).[79]

Both the open circuit voltage V_{oc} and the short circuit current I_{sc} are observed to decrease with electrode separation d (see Figure 6.5). The short circuit current shows a more pronounced drop with distance than the open circuit voltage. This is reasonable considering that the maximum range of tritium beta particles in air is about 6 mm and that their kinetic energy decays exponentially with the distance traversed. Moreover, electron-ion recombination increases as the electrode separation increases.

6.2.2 Semiconductor Sandwiched CPD Betavoltaic

Using semiconductor medium a solid state CPD cell can be obtained [79]. The radiation ionization energy is much smaller than that in the gas, so more electron ion pairs can be created which thus boosts the current for same amount of radiation source. Intrinsic hydrogenated amorphous silicon (a -Si:H) is a widely used semiconductor material in photovoltaics[54] and it was also used in betavoltaics [6, 8]. We choose the a -Si:H as the dielectric medium here, and it was sandwiched between a platinum (Pt) anode and ScT cathode. Titanium and platinum were sequentially evaporated on a silicon substrate using an e-beam evaporator; the Ti and Pt films were approximately 20 nm and 200 nm thick, respectively. Subsequently, a -Si:H film of 400 nm in thickness was deposited on the Pt film using the dc saddle field PECVD technique.[6, 8] The deposition here involved the flow of pure silane gas through the glow discharge chamber at 30 sccm (the abbreviation of Standard Cubic Centimeters per Minute) with a chamber pressure of 160 mTorr, anode potential of 600 V, anode current of 18 mA, ion current to substrate of 0.6 mA, substrate temperature of 250 °C, and deposition duration of 1 hour and 20 minutes. Thereafter, an array of scandium dots was thermally evaporated onto the a -Si:H; the Sc dots

were of 3 mm diameter and 300 nm thickness each. Finally, the Sc dots were tritiated using tritium gas. A schematic of the cell is illustrated in Figure 6.6.

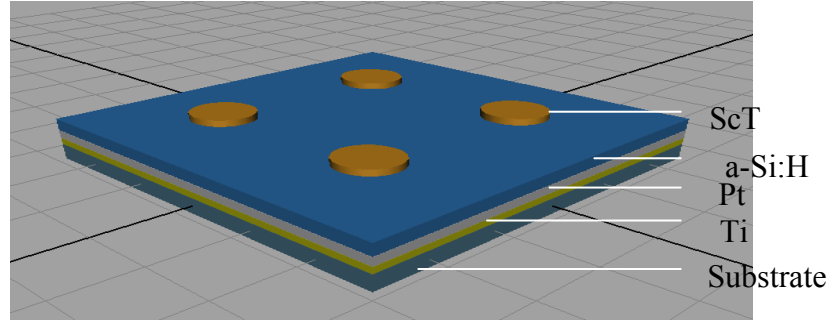


Figure 6.6 The schematic of the solid state CPD cell. The Sc:T is the cathode, Pt is the anode and a-Si:H is the semiconductor medium. [79]

Prior to the tritiation step, each cell was tested for its IV characteristics under darkness and room light illumination. The cells showed good rectification and photovoltaic characteristics. The tested CPD cells were then exposed in tritium gas for 10 hours at a temperature of 250 °C and a pressure of 10 bars. The resulting scandium tritide film showed a surface activity of 15 mCi/cm². In a-Si:H the mean ionization energy is reported to be approximately 4.5 eV per electron-hole pair.[53] The theoretical upper limit for the short circuit current density can be estimated using the following relation[53]

$$J_{sc} = \lambda n_T E_\beta / \varepsilon \quad (6.1)$$

where λ is the decay constant of tritium (1.78×10^{-9} s), n_T is the surface activity of the scandium tritide film (15 mCi/cm², which is equivalent to 3.1×10^{17} atoms/cm²), E_β is the average kinetic energy of the tritium betas (5.7 keV), and ε refers to the ionization energy (4.5 eV). Equation (6.1) yields a J_{sc} of 110 nA/cm².

After the tritiation, IV measurements were carried out on all functional cells in darkness. A typical result is shown in Figure 6.7. Powered by the ScT film, an open circuit voltage of 160 mV and a short circuit current of 370 pA were measured. The area of the ScTx disc is about 7 mm². The maximum power point was measured to be 18 pW (0.26 nWcm²). The short circuit current density is 5.3 nA/cm², which is 4.8% of the theoretical limit calculated by Eq. (6.1). Owing to a smaller ionization energy in *a*-Si:H, the short circuit current density is doubled in comparison with that of the cell with the gaseous dielectric, though the overall output power density in this solid cell doesn't improve owing to a lower open circuit voltage.

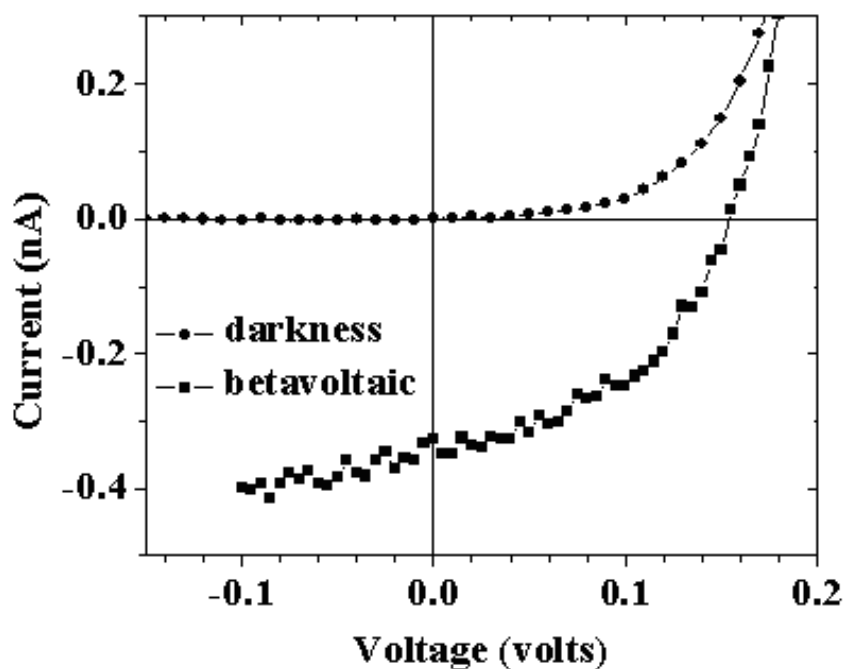


Figure 6.7 The IV characteristics of the solid CPD cell in darkness before tritiation and betavoltaic performance after tritiation. [79]

6.3 SUMMARY

In summary, tritium based betavoltaics using scandium tritide films and contact potential difference have been demonstrated. The batteries utilize gaseous and *a*-Si:H film as dielectric media, displaying short circuit current densities of 18% and 4.8% of the theoretical limits, respectively. Both CPD cells with gas and semiconductor media produce nanowatt power. The energy conversion efficiency is calculated to be around 0.1%. This is consistent with reported betavoltaic devices powered by tritium,[6, 7] This is less than that of the wide bandgap semiconductor SiC *pn*-junction cell using high energy beta using ⁶³Ni and ³³P.[28, 29] In the gaseous CPD cells the low power density and conversion efficiency is attributed to the relatively high ionization energy, while in the *a*-Si:H CPD cells the lower performance is attributed to the low built-in field and associated higher recombination rate.

The batteries provide nanowatt power with a projected life time comparable to the half-life of tritium and can be operated at temperatures as high as 250 °C. The appropriateness of ScTx is also evident from its low tritium vapour pressure at elevated temperatures.[80] The output power density can be further enhanced by increasing the surface activity of the ScTx film using a textured surface as well as through improved passivation of the CPD cell. It is suggested that using stacking series-connected cell geometry, a tritium battery based on the CPD principle could be realized with a continuous output power of 1 μW and corresponding cell volume of ~1cm³.

7.0 TRITIUM BETAVOLTAICS USING SEMICONDUCTOR PN JUNCTIONS

7.1 THREE DIMENSIONAL SEMICONDUCTOR PN DIODE FOR BETAVOLTAICS

Radioisotope batteries have utilized some different types of nuclear-to-electricity conversion mechanisms. Direct conversion radiovoltaic devices using p-n semiconductor junction is one of the favorable, and well-suited to beta emitters such as tritium, Ni-63 and Pm-147 primarily due to minimized lattice damage considerations. The main factors that limit the performance of a radioisotope powered betavoltaic battery include the energy conversion efficiency and the fuel fill factor. The theoretical maximum of betavoltaic efficiency is about 20-22% for wide band semiconductor and decrease to 13-14% for silicon.[20, 81] Theoretical maximum of efficiency of tritium based betavoltaic converters reduces to about 15% for wide band semiconductor and to 8-9% for Si based cells owing to low photocurrent density ($\sim 1\mu\text{A}/\text{cm}^2$). By deploying some wide bandgap semiconductor materials and high quality junction devices, the efficiency can be improved. A range of semiconductor *pn*-junctions have been used for betavoltaic applications such as amorphous silicon,[6] silicon carbide[28] and gallium arsenide[22], however, their energy conversion efficiency is still limited by the available open surface area directly exposed to the energetic particles. To raise the fuel factor, past attempt has been made by employing KOH etched pyramidal texturing [25]. However, the KOH etching can give a fuel factor enhancement of only 1.85 times.

Advances in MEMS/NEMS and nanotechnology also offer innovative opportunities to raise the fuel fill factor and utilize radioisotope power more efficiently. Recently, micro-engineering has been used to fabricate so-called three dimensional (3D) *pn* diodes to considerably increase surface area of a *pn*-junction device in a given volume. Porous or trenced 3D *pn*-junctions fabricated using either electrochemical etching [7, 27] or deep reactive ion etching (DRIE)[26] promise a significant increase in the surface to volume ratio of the device and accordingly increase in power production and energy conversion efficiency of nuclear batteries.

The 3D configuration is particularly advantageous for betavoltaic devices harnessing low energy beta particles such as those from decay of tritium or ^{63}Ni . Tritium produces energetic electrons with an average energy of 5.7 keV and a maximum energy of 18.6 keV which poses little radiation damage concern for on-chip energy conversion devices. On the other hand, the beta particles at 5.7 keV can only traverse about 0.1 μm in solid materials (e.g. metal tritide and semiconductors). In another word, the energy conversion process occurs mainly near the surface. Therefore, effective energy conversion of low-energy beta particles requires a large surface powering the betavoltaic device. The use of 3D *pn*-junctions is one approach that can improve power production. Pores and ridges fabricated in semiconductor materials at the micron and submicron level permit large surface to volume ratios. Moreover, infiltration of micrometer sized porous structures with tritium fuel minimizes self-absorption losses in energy and results in relatively complete delivery of tritium beta energy into the energy conversion region of the device. Thus, high-density tritium fuel can be utilized efficiently.

The fabrication of the 3D p-Si diode commences by electrochemical anodized etching of the p-type silicon leading to the formation of porous structures. The average pore diameter and

depth are 1 and 45 μm , respectively. The fraction of the planar surface containing the pores is 0.31. The total surface area is estimated to be magnified by 50 times, 98% of the surface area being inside the porous structure. The *pn* junction is formed on the entire surface including the internal pore surface using a P_2O_5 diffusion process.[7] A 50-nm thick aluminum contact layer is evaporated on the porous side. Due to the high aspect-ratio and small diameters of porous structures, little aluminum was deposited on the side wall. A SEM picture of the cross-section picture of the porous diode is shown as Figure 7.1

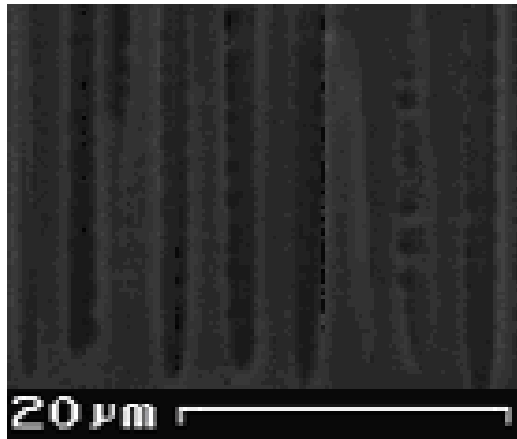


Figure 7.1 The SEM image of the 3D porous silicon device.

7.2 HIGH PRESSURE TRITIUM POWERED P-SI DIODE

If we take the traditional planar structured diode as a surface effect battery, the macroporous structure of the p-Si diode provides us a volume effect battery. The gaseous tritium is particularly suitable for powering this sort of batteries, and the input power density can be increased by using tritium of high pressure. It is noted here that for a planar diode, the input power density from the

gaseous tritium is limited due to the limited transverse range of the betas. At the standard condition, the tritium betas can traverse about 32 mm in tritium gas, and tritium gas beyond 32 mm of the cell won't contribute in the power input at all. By pressurizing, the transverse range drops accordingly. In the 3D p-Si cells the macro-pores usually have a dimension of microns, the self-absorption in the gas is negligible even at very high pressure, e.g. 100 atm. In the study here, the power scaling of 3D diodes as function of tritium fuel density is examined. By exposing 3D diodes in gaseous form of tritium, the power output of a 3D diode is studied from 0.05 to 33 atm at room temperature, which is corresponding to an isotope power density from $4.35 \mu\text{W}/\text{cm}^3$ to $2.87 \text{ mW}/\text{cm}^3$.

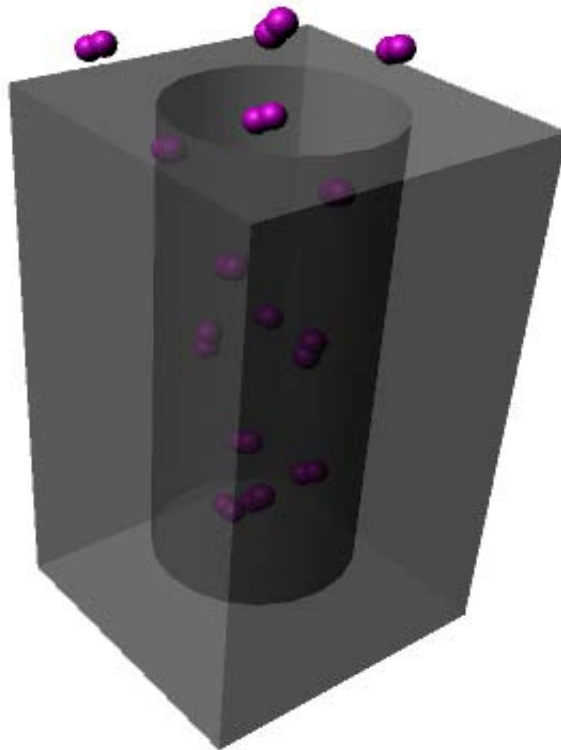


Figure 7.2 An illustration of the tritium molecules in the pores of the p-Si device.

The test with gaseous tritium was performed using a sample with a size of $1 \times 2 \text{ cm}^2$. The sample is sealed in a stainless steel chamber. The chamber was initially purged with helium gas and then pumped down to 10^{-3} mTorr. The tritium gas was then gradually introduced into the chamber. The IV characteristics of the sample monitored via appropriate electric feedthroughs during the pressurization. There are two areal regions of the 3D diode that contribute to the produced betapower. These are the un-anodized top planar surface and surface internal to the pores (See Figure 7.2).

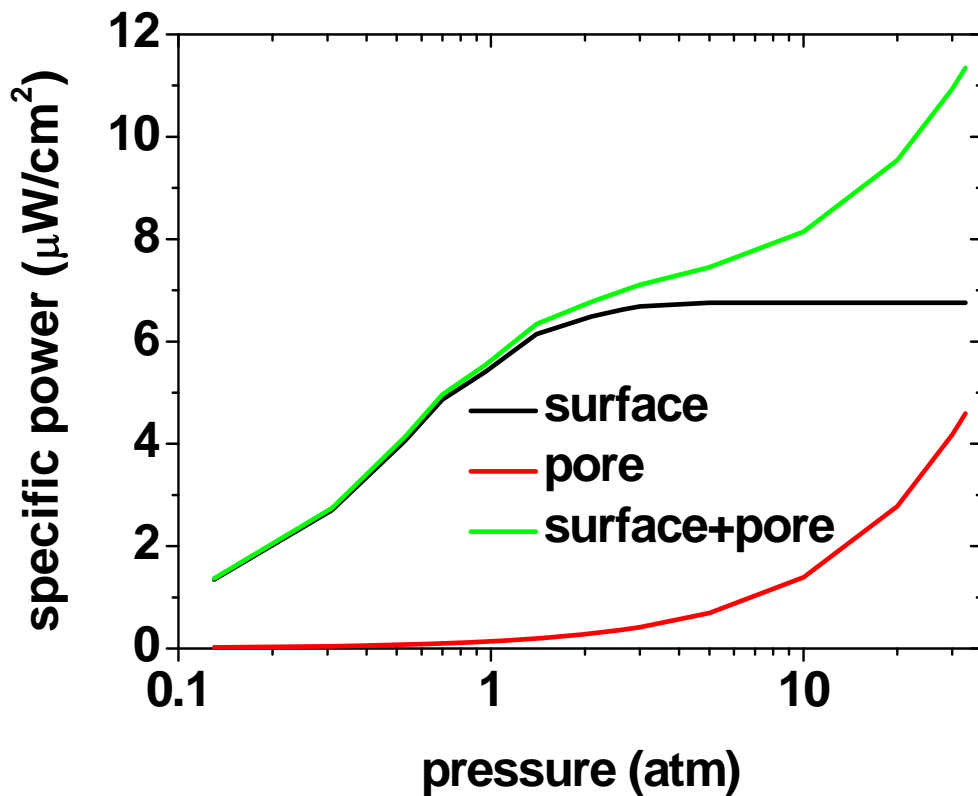


Figure 7.3 The effective specific power due to the gaseous tritium impinging on the planar device surface, on the pore device surface, and the total specific power, as a function of the tritium pressure.

As mentioned above, due to self-absorption the maximum propagation distance of beta particles produced by tritium decay is limited to approximately 3.2 cm at 1 atm (for 18.6 keV beta). With increasing tritium pressure the range of the tritium betas is reduced. Hence, the beta flux impinging the un-anodized top surface saturates at around 2 atm with a maximum power flux of $14 \mu\text{W}/\text{cm}^2$. [22] The 50 nm Al coating is estimated to block 3/4 of the beta energy. [76] Thus the maximum beta power flux impacting the un-anodized top surface is estimated to be $6.8 \mu\text{W}$ for a 1cm^2 3D diode. In sharp contrast, tritium gas trapped in the small porous structures suffers negligible self-absorption due to the small pore diameter of $\sim 1 \mu\text{m}$, thus almost 100% of beta particles produced by tritium decay inside pores impinge on the pore surface. The beta power flux therefore increases linearly with the tritium pressure. It is estimated that the total void volume in the pores is $\sim 1.6 \text{mm}^3/\text{cm}^2$, accordingly the power flux internal to the porous structure will increase linearly to $4.6 \mu\text{W}$ at 33 atm tritium pressure for a 1cm^2 3D diode. Figure 7.3 illustrates beta power flux impinging the un-anodized top surface and internal pore surface as a function of tritium pressure.

The experimental IV characteristics of the 3D diodes as a function of tritium pressure are shown in Figure 7.4-7.6. A typical IV curve of the diode in dark and at tritium pressure of 0.8 atm is plotted as Figure 7.4, in which a short circuit current of $1.6 \mu\text{A}$ and an open circuit voltage of 22 mV are obtained; the maximum output power is about 9.2 nW.

The short circuit current (I_{sc}), and open circuit voltage (V_{oc}) as a function of the tritium fill pressure is presented in Figure 7.5 a) and b), respectively. The short circuit current I_{sc} increases with the tritium pressure reaching a maximum of $2.93 \mu\text{A}$ at 33 atm. This is consistent with the increase of the beta flux in the pores. However, V_{oc} does not behave as expected. The open-circuit voltage reaches a maximum 22 mV at 0.8 atm and subsequently drops to 11 mV

when the pressure reaches 33 atm. It is unclear what causes the drop in cell potential. However, it is speculated that with increasing tritium pressure the localized beta heating induces surface migration-diffusion of aluminum from the planar surfaces to the edge surface and accordingly causes a shunt across the metallurgical junction.

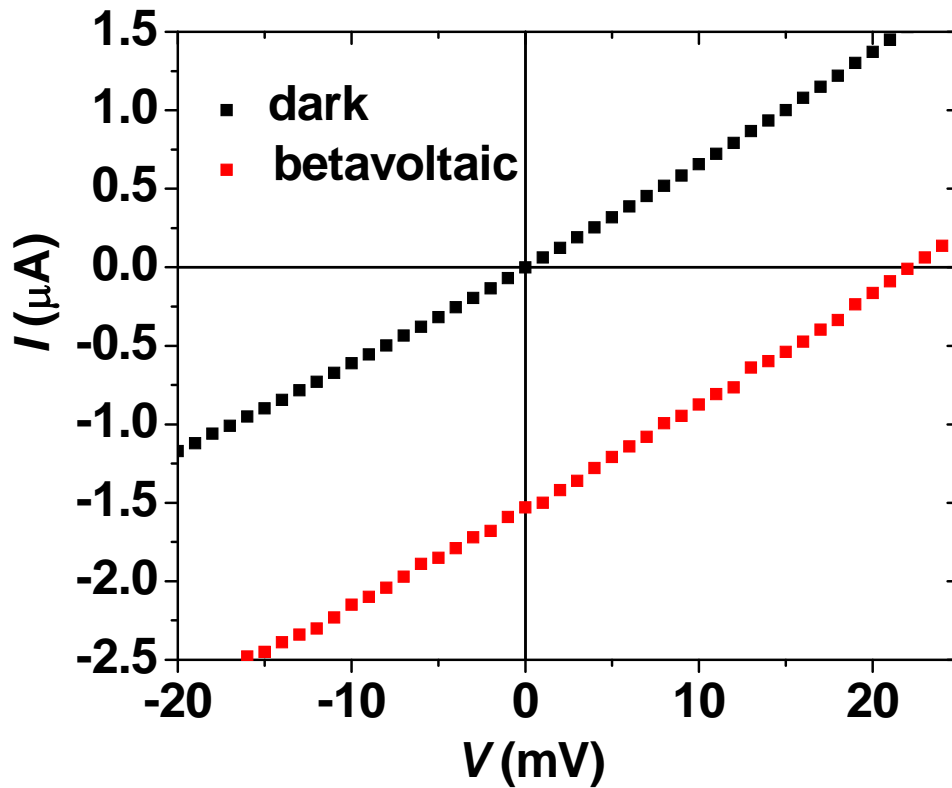


Figure 7.4 The IV characteristics of the 3D diode under tritium-free dark condition and at tritium pressure of 0.8 atm.

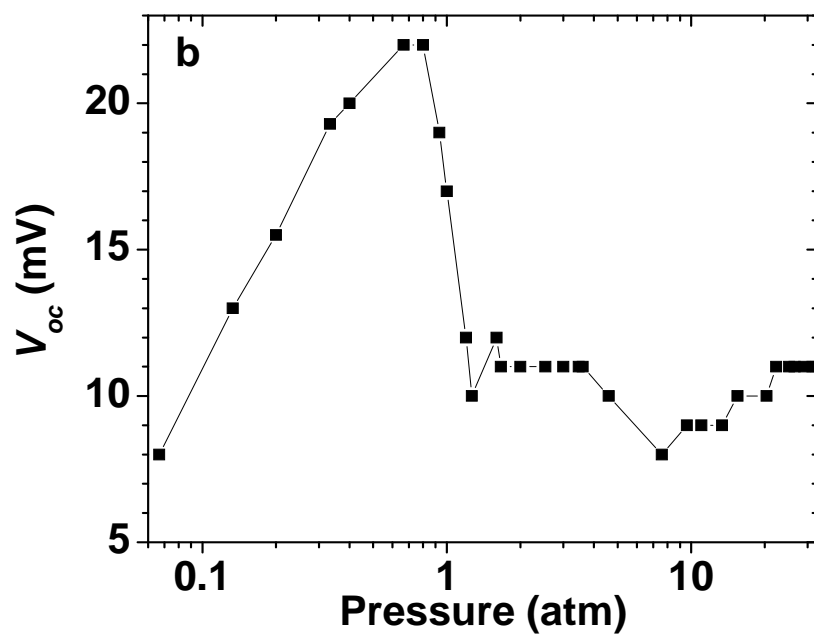
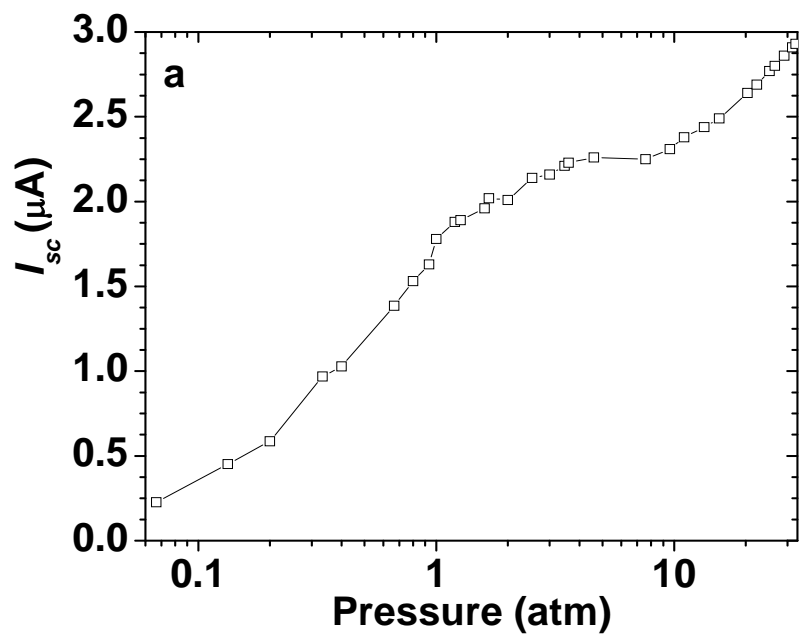


Figure 7.5 a) The short circuit current density (I_{sc}), and b) the open circuit voltage (V_{oc}), as a function of tritium pressure.

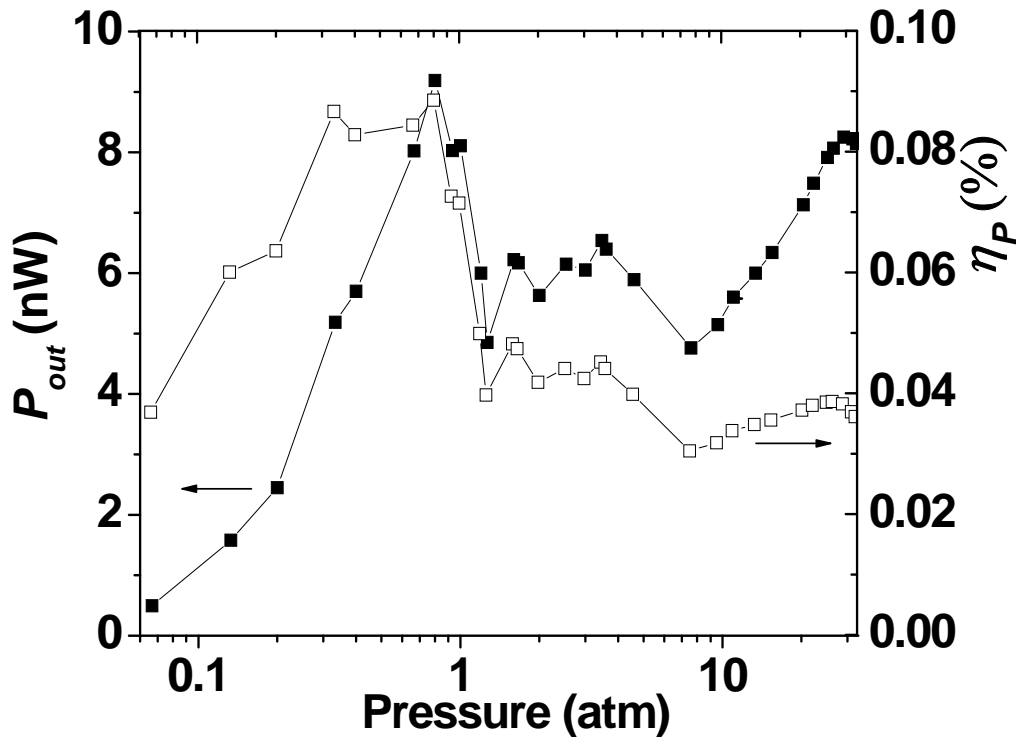


Figure 7.6 The output power (P_{out}) and the energy conversion efficiency (η_p) as a function of tritium pressure.

The output power (P_{out}) is shown in Figure 7.6. The P_{out} doesn't increase beyond 0.8 atm due to the drop of V_{oc} , and the maximum power obtained is 9.2 nW for the 1×2 cm² sample. The energy conversion efficiency (η_p) is also calculated and shown in Figure 7.6; the η_p falls in the range in 0.03-0.09 %.

The efficiency is consistent with previous results obtained at regular pressure test.[7] The output power increases with the tritium refill pressure below 0.8 atm. The output power hovers around below 9 nW due to the stuck retardance of the voltage. While as we observed, the current keeps increasing, this indicates that the raise of tritium pressure acts on the cell.

7.3 SCANDIUM TRITIDE POWERED P-SI DIODE

To further analyze the results obtained from the pressure experiment. The 3D diode was also powered by two difference forms of solid tritium fuels. As a comparison to the 2D power configuration, a 300nm thick scandium tritide (ScT) film with a surface activity of 15 mCi/cm² [79, 82], which is equivalent to a power density of 0.5 μ W/cm², was used to power the 3D diode. This is the first, in-direct, solid tritium fuel.

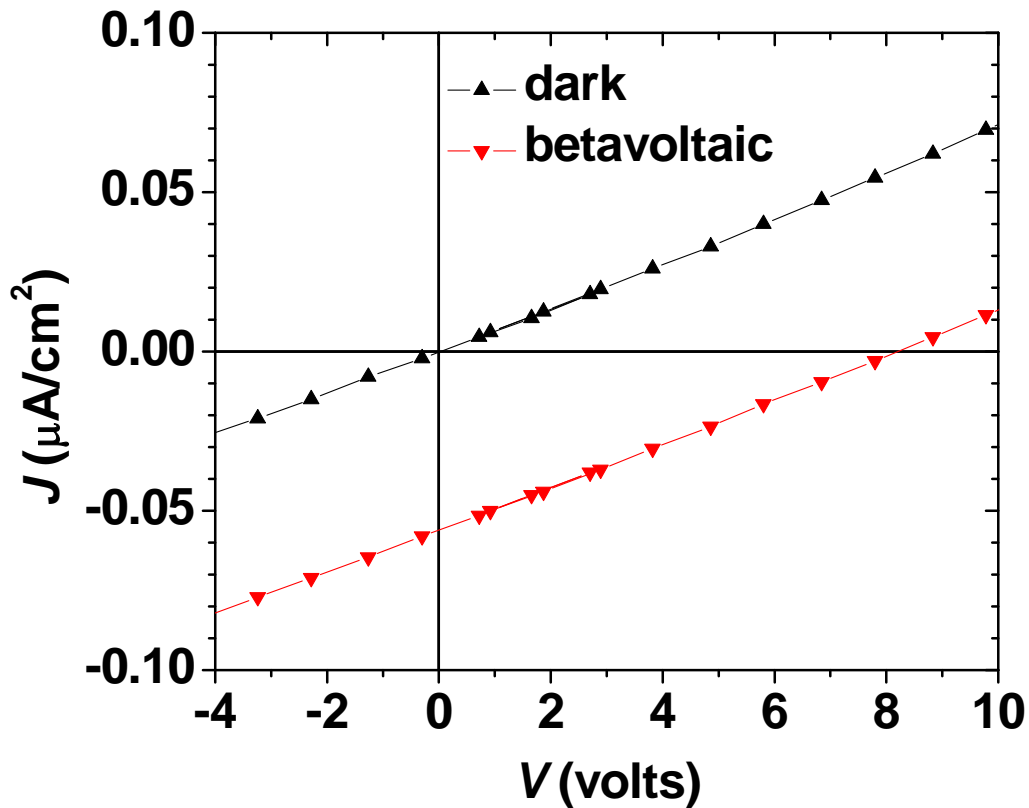


Figure 7.7 The IV characteristics of the 3D BV cell under dark conditions and when powered by a ScT film (indirect solid tritium).

The measurement was performed at standard condition with the ScT film directly in contact with the diode. A J_{sc} of 55 nA/cm² and an V_{oc} of 8 mV was measured, respectively, resulting in a maximum output power of 0.12 nW/cm². The IV characteristics of the cell measured in dark and with the irradiation from the ScT beta source are shown in Figure 7.7. Taking into account of the shielding effect of 50 nm Al contact layer, the input isotope power flux reaching the device is estimated to be 240 nW/cm². The maximum short circuit density is calculated to be 64 nA/cm²; the current collection efficiency of 86% and the conversion efficiency of 0.05% are calculated. Both the collection efficiency and the energy conversion efficiency are consistent with those obtained by the tritium gas source.

7.4 INTERNALLY OCCLUDED TRITIUM POWERED P-SI DIODE

The porous surface of the 3D silicon cell is capable of absorbing tritium[57], which offers a convenient 3D beta source to power the diode; this is the second, direct, solid tritium fuel. This result is compared with the 2D beta source of ScT film. The porous diode was tritiated in tritium gas at a slightly elevated temperature of 100 °C and a pressure of 10 atm for 1 day. The tritium effusion measurement was carried out to determine the quantity and bonding characteristics of the tritium occluded in the device.[54, 57] The normalized tritium effusion profile and the tritium evolution rate as a function of the temperature are shown in Figure 7.8.

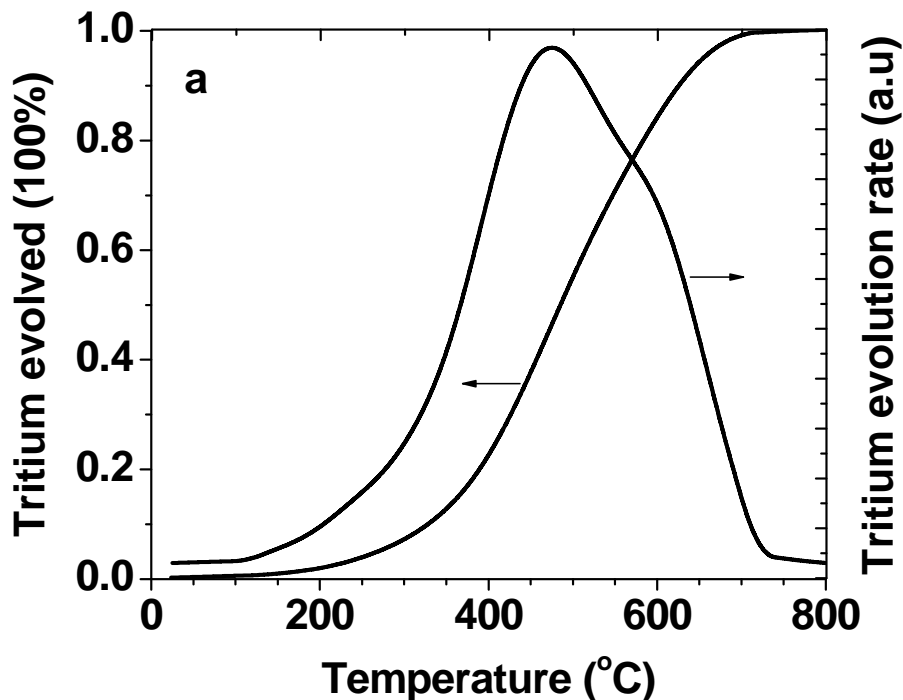


Figure 7.8 The tritium effusion profile and the effusion rate as a function of temperature for the 3D silicon cell tritiated in tritium gas at 100 °C and 10 atm.

The tritium effusion rate profile shows the out-diffusion peak around 480 °C. The effusion profile is consistent with the previous result of tritiated crystalline silicon. It suggests that chemical bonding of tritium on the surface of porous silicon is similar to those on the surface of crystalline silicon.[57] For the size of $1 \times 1 \text{ cm}^2$ porous 3D structure, the effusion experiment yielded 4 mCi of total tritium activity. Considering the 50 fold magnification in the surface area of the porous sample, the corresponding surface activity is 0.08 mCi/cm^2 . This result is in consistent with reported data of crystalline silicon tritiated at similar condition (0.1 mCi/cm^2).[57] This experiment indicates that tritium has been occluded in the sidewall surfaces of the porous 3D diode.

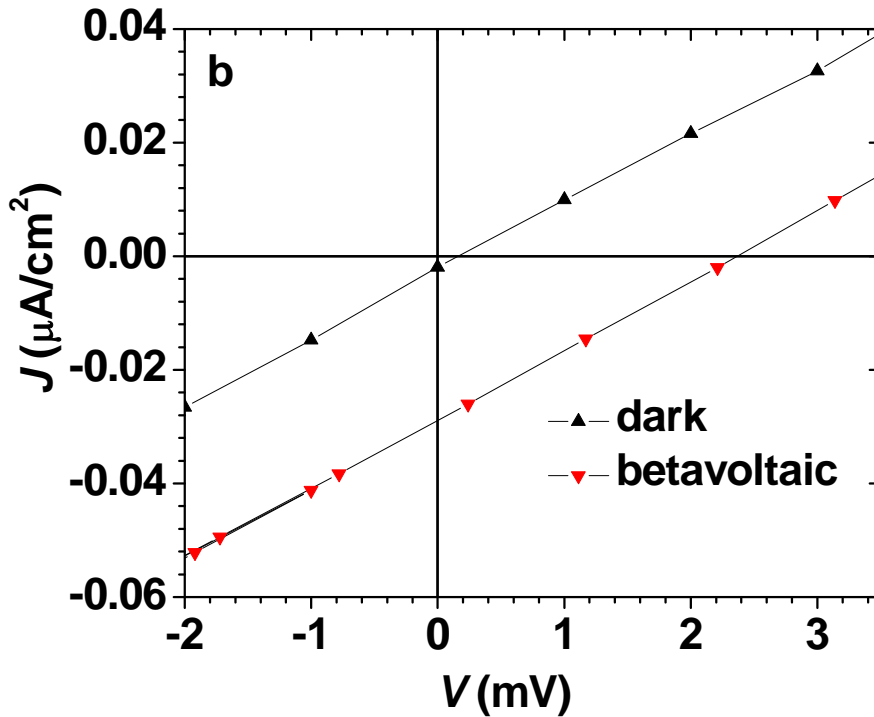


Figure 7.9 The IV characteristics of the 3D BV cell under dark condition and when powered by tritium incorporated into the porous surface (direct solid tritium).

The IV characteristics of the diode before and after the tritiation are shown in Figure 7.9. A J_{sc} of 29 nA/cm² and an V_{oc} of 2.4 mV was measured for the tritiated cell, respectively. The measured V_{oc} is relatively low in comparison to the measured V_{oc} powered by the 2D ScT film. One reason is due to the lower power input; 4 mCi/cm² is equivalent to a power density of 0.13 μW/cm². Given the shallow position of the pn-junction in relation to the porous surface, another possible reason is the diffusion of tritium into the depletion region. Tritium decay in the junction could lead to the formation of recombination centers and accordingly reduces the open-circuit voltage since the *pn*-junction of the 3D diode was formed very close to the porous surface.

7.5 SUMMARY

In summary, the 3D diode shows an advantage of the 3D cell and the power scaling effect powered tritium gas. The IV characteristics of the diode under high tritium pressure shows an increase in short-circuit current due to the large surface area of the porous structure. However, at high pressures the open circuit voltage, and accordingly the power conversion efficiency, are observed to decrease; this is attributed to localized heating induced shunt at the metallurgical junction. This result is consistent with the IV performance of the diode powered by tritium directly absorbed into the porous surface. To fully explore the potential of 3D diode structures, immobilized tritium source may need to be infiltrated into appropriate porous or deep trenched structures contiguous but sufficiently displaced from the pn junction.

8.0 TRITIUM IN NANO-MATERIALS

8.1 INTRODUCTION

Nanotechnology is a highly multidisciplinary field of applied science and technology whose theme is the control of matters of generally 100 nanometers or smaller, and the fabrication of device or materials that lie with the size range.[83, 84] With the rapid development of the nanotechnology, a bunch of novel nano-materials are emerging, such as carbon nanotubes (CNTs), quantum dots (QDs), nano-wires, rods, and particles. As the size of the system decrease, a number of properties and phenomena because pronounced for the nano-materials, for example, the vastly increased ratio of surface area to volume. Those materials also own other excellent advantages in quantum efficiency, electrical and thermal conductivity.

The nanotechnology has made prominent progress, especially in the last two decades. A large number of publications are generated devoted to method of their preparation, study of their properties, and possible applications. Up to now, tritium has very rarely been introduced into the field of nanotechnology, and very few publications have appeared in study of tritium in nano-materials. Tritium, as the isotope of hydrogen, is chemically active to most of the elements in the periodic table. Owing to its unique radioactive properties, interaction of tritium with nano-materials can be of great interest and can potentially lead to some useful applications. In this

chapter, we introduce two applications of nano-materials in tritium study: the use of CNTs in tritium room-temperature storage and beta-luminescence of ZnO nanowires.

8.2 TRITIUM STORAGE USING CARBON NANOTUBES

It is generally believed that the carbon nanotubes were discovered by a Japanese physicist at NEC in 1991.[85] They are cylindrical carbon molecules and categorized as single-walled nanotubes (SWNTs) and multi-walled nanotubes (MWNTs). There are a few methods in preparation including electric arc and laser-induced evaporation, pyrolysis of hydrocarbons, deposition of metal carbide, etc.[86] They exhibit extraordinary properties and make them potentially useful in many applications in electronics, optics, material science and other field of science and technology.[87-91]

The cylindrically shaped structures of carbon nanotubes are formed by the folded graphite carbon. The interior channels of the tubes are several nanometers in diameter, which favors the efficient capillary occlusion of gas molecules (Figure 8.1), such as hydrogen. Hydrogen is incorporated in nanotubes by exposing those in hydrogen atmosphere at low temperature. The gravimetric density ranging in 5% to 10% has been reported.[92-94]

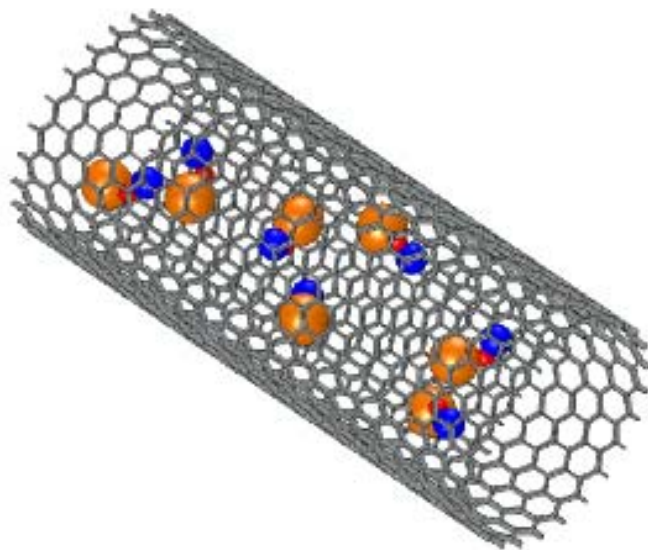


Figure 8.1 Schematic of gas molecules in single-walled carbon nanotubes.

As the isotope of hydrogen, tritium is chemically identical to protium (^1H). The carbon nanotubes are expected to be a good carrier for tritium. Although no experimental study has been reported, numerical simulation shows that carbon nanotubes can exhibit quantum sieving, where heavy isotopes are preferentially adsorbed over light isotopes.[95, 96] Here, we experimentally studied the capability of these CNTs in tritium storage [97].

The Single Wall Carbon Nanotubes here were synthesized using the pulse laser vaporization technique having diameters of $\sim 1\text{nm}$, lengths on the order of micrometers and high surface area of $\sim 1600\text{m}^2/\text{g}$ [98]. Figure 8.2 shows the SEM image of the SWNTs. The CNT samples were exposed to tritium gas at temperature of $100\text{ }^\circ\text{C}$ and pressure of 70 atm over a time duration of 3 days.

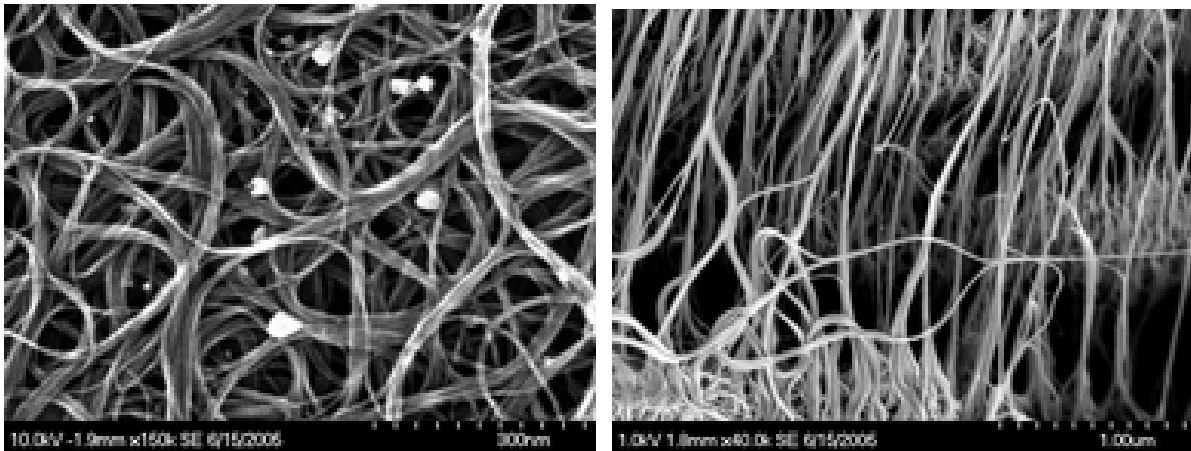


Figure 8.2 SEM image (top and side views) of the purified Single Wall Carbon Nanotubes.

After the exposure, thermal effusion experiments were carried out on those tritiated samples at a linear ramp rate of 20 °C/min; typical temperature profiles of tritium effusion from the tritiated CNT sample is shown in Figure 8.3. Tritium effusion commences at the loading temperature of 100 °C and by 900 °C essentially all the tritium is evolved from the sample. Most tritium effuses at high temperature, around 500 °C; this indicates that most of the tritium is stably bonds to the CNT. Tritium atomic concentration of 1.9 at.%, and equivalently a weight concentration of 0.5 wt.% were measured for the CNT samples.[97] The Gaussian deconvolution of the effusion rate curve yields two peaks: one low temperature peak at 240 °C, and a high temperature peak at 500 °C. The low temperature peak is likely associated with the physically absorbed tritium, while the high temperature peak is associated with the chemically absorbed tritium in the CNTs.

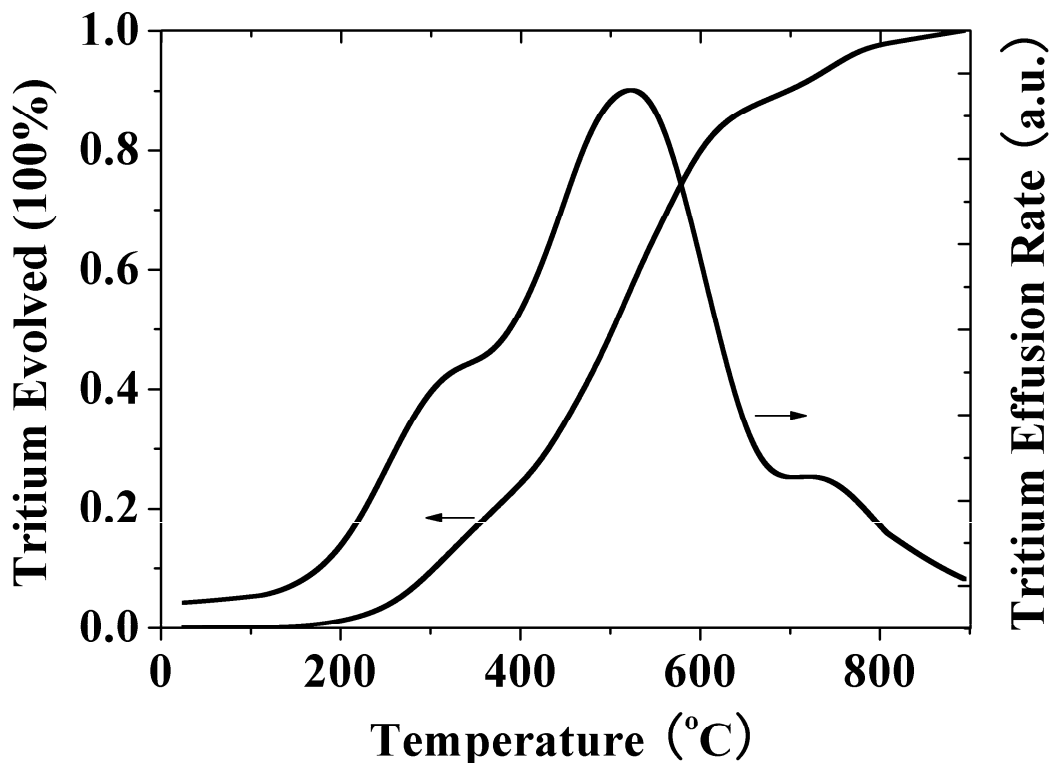


Figure 8.3 Tritium effusion and tritium effusion rate as a function of temperature for CNT sample exposed to tritium gas at 70 atm and 100°C for 3 days.[97]

As the first attempt in tritium incorporation in carbon nanotubes, tritium is stably immobilized in CNTs and a gravimetric density of 0.5% was achieved. The effusion shows that the tritium is stable up to 200 °C. It is noteworthy that there is much room to improve in the density of tritium in CNTs based on the reported results of the hydrogen storage. Assuming 10% by weight of hydrogen is retained in nanotubes on changing from hydrogen (protium) to tritium, a specific activity of tritiated CNTs is 1000 Ci/g. Such a tritium carrier would be very useful in betavoltaic energy conversion devices, and luminescence lighting devices.

8.3 ZNO NANOWIRE BETA-LUMINESCENCE

The radio-luminescence (RL) was discovered as early as 1898 by Becquerel, who observed fluorescent uranium compounds fogged film through opaque media.[99] Later in 1920s, it was found by Elster, Geitel and Crookes that alpha radiation could produce scintillation in zinc sulfide screen. In 1970s, light sources based on RL were invented employing a large number of radionuclides and used as emergency sign, military illumination and other special conditions. [100] Up to now, tritium lighting has already been an industry consuming large quantities of radioisotopes. With the development of the modern technology, new material and technique has been involved in the radio-luminescence. The new light sources include the organic formulations with fluorescent organic dyes or inorganic phosphors [101, 102]and other tritium storage material such as zeolites.[103] The wide band gap semiconductors powered by tritium gas have also been involved in the RL[104]. With the rapid development of nanotechnology, a bunch of nano-materials are available with advantageous properties in electronics and photonics. The ZnO nanowires are potentially good candidate for radio-luminescence.

In the past decade, due to the strong commercial desire for ultraviolet (UV) and blue optical devices, great interest has been focused on the synthesis and optical properties of wide-band-gap semiconductors. Zinc Oxide (ZnO), a II-VI compound semiconductor with a wide and direct band gap of 3.37 eV at room temperature, has been recognized as a good candidate for use in blue and UV light emission and room temperature optical UV light source[105]. Beside the bulk

and thin form of ZnO, the low dimensional nanowire structure has been synthesized and their optical and electrical properties have been extensively investigated. The room temperature photoluminescence of ZnO nanowires generally show three bands in UV, green and yellow region[105-108]. The UV emissions are commonly attributed to the direct combination of excitons through an exciton-exciton collision process, and the green and yellow emissions are identified as being from the radiative recombination of electrons from shallow donors with the trapped holes from singly ionized oxygen vacancies and interstitial oxygen [109].

The ZnO nWs we utilized for this study were grown on silicon substrate using the standard vapor-liquid-solid (VLS) technique [110, 111]. The nanowires were tuned to emit the green light by modifying the oxygen content during the preparation. The ZnO nanowires morphology was studied using scanning electron microscopy (SEM) (Figure 8.4). The SEM observation showed that the nanowires have lengths of 8-10 μm and diameter of 40-100 nm [112]. The PL spectrum for the undoped sample shows weak band-edge luminescence at 380 nm and strong midgap emission at 525 nm.[112]

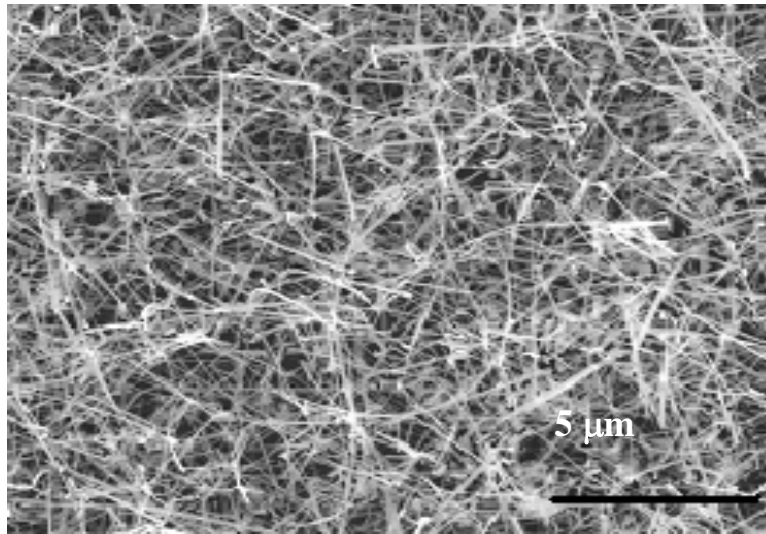


Figure 8.4 SEM image of the ZnO nanowires.

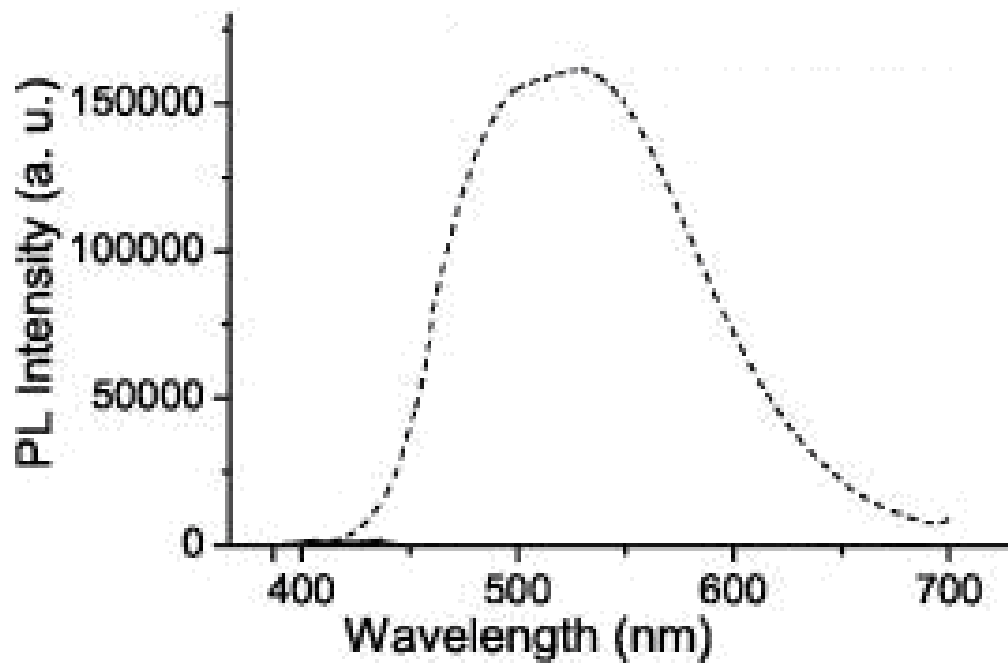


Figure 8.5 Photoluminescence spectra of undoped ZnO nanowires at room temperature. [112]

The beta-luminescence of the ZnO nanowires is studied using the scandium tritide film beta source. The scandium tritide has a surface activity of 15 mCi/cm^2 . [79] The spectrum of the nWs under beta illumination was shown as Figure 8.6. A broad spectrum with wavelength ranging between 400 and 600 nm were observed. The peak is generally located at the same region as the photoluminescent spectrum, which reveals the same mechanism in the light emission. Weak peaks at UV region and yellow band are also observed at around 340-380 nm and 620 nm. The UV emission is attributed to the direct exciton recombination and the yellow band emission is attributed to the electron recombination with the ionized oxygen vacancy or interstitial oxygen.[105]

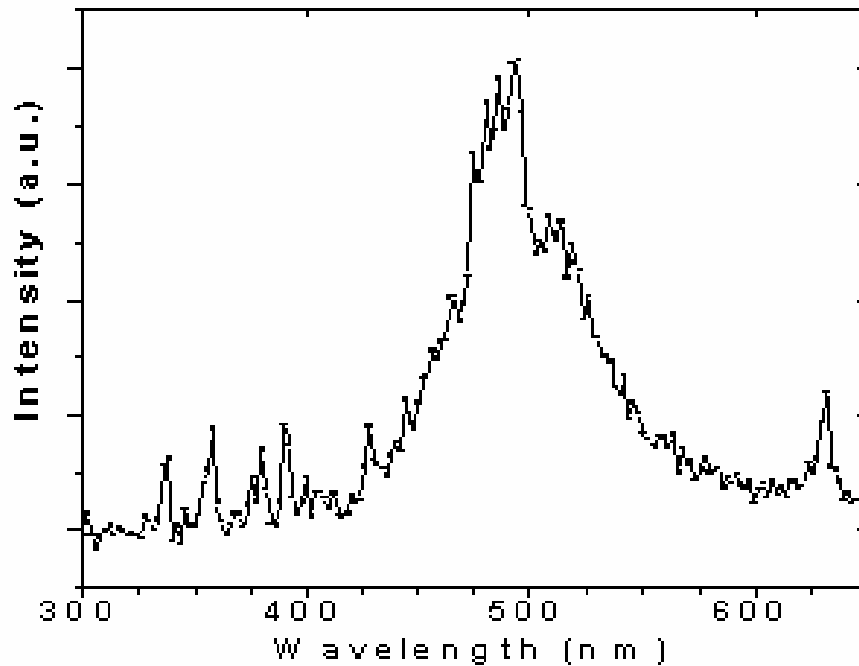


Figure 8.6 The emission spectrum of the ZnO nWs under beta illumination.

The surface activity of the beta source is relatively low. Tritium gas can generate much higher density of beta flux, $14 \mu\text{W}/\text{cm}^2$ in power flux for a tritium gas layer of 1 cm at standard temperature and pressure. Exposing the ZnO nanowires in the tritium gas is expected to realize a self-powered lighting device with bright green light emission. By adjust the oxygen content in the material; the emission can also be tuned to UV region. Ultimately, the RL source can be used for lasing. Moreover, this research also provides a chance to study the fundamental properties of the nanowires under beta irradiations.

In summary, the phenomena of tritium in nano-materials, carbon nanotubes and ZnO nanowires, were experimentally studied. Tritium stably incorporation in CNTs with a density of 0.5 wt.% was realized. Beta-luminescence of ZnO was also exhibited. Tritium interaction with nano-materials is rarely attended area and there are more interesting phenomena to be revealed.

9.0 SELECTIVE LOCKING OF TRITIUM IN SILICA USING DEEP UV LASER IRRADIATION

9.1 INTRODUCTION

Hydrogen is widely used in micro-electronic and photonic industries as a doping element and hydrogen loading is common technique in fiber Bragg grating writing [113-126]. First reported by Lemaire et al., photosensitivity of silica fiber is dramatically enhanced by exposing the fiber to a high-pressure hydrogen environment [127]. The permeated hydrogen molecules react with silica under deep ultraviolet (UV) laser irradiation to form a stable –OH bond [126, 128, 129]. Hydrogen occluded through this photochemical process increases the UV-induced refractive index change in the silica fiber by four orders of magnitudes [124]. Owing to the increased optical loss in the 1550 nm telecommunication window induced by the –OH bond, deuterium has also been used to red shift the –OH absorption tails beyond 1900 nm [130]. Accelerated thermal annealing tests have shown that –OH bonds formed through UV irradiation are normally very stable up to 400 °C [131, 132]. Considering that tritium is chemically identical to hydrogen, notwithstanding the difference in atomic mass and its radioactive nature, it is expected that similar laser processing can also occlude tritium in glass to provide a stable, on-chip isotope power source.

In this chapter, the high pressure hydrogen exposure and laser irradiation technique is migrated to the nuclear micro-engineering field by substituting tritium for hydrogen. It is shown

that high-pressure tritium loading and deep UV laser irradiation are simple and effective means to occlude tritium in silica glass. By forming the Si-OT bond, the gaseous nuclear fuel is safely immobilized and integrated for on-chip applications [82]. This laser-locking of tritium potentially opens the door to radioisotope micro-power on-chip integration in silicon oxide for a wide array of micro-electronic and MEMS applications.

9.2 EXPERIMENTAL PROCEDURES

The 8 μm thick silica films containing 3% atomic Germanium (Ge) were used. The Ge-doped layer was grown over a 20 μm thick silica-cladding layer on crystalline silicon using the flame hydrolysis deposition technique. This glass composition is widely used in fiber optics, which has high photosensitivity after hydrogen loading.

The silica sample was tritiated at a tritium pressure of 70 atm and a temperature of 60 °C for 20 hours. The laser locking experiments were carried out using a 248 nm KrF excimer laser (Lambda Physik Compex 102) with a series of time durations, which corresponded to total laser fluence of 700, 3000, and 4800 J/cm^2 . Afterwards, the non-irradiated and irradiated samples were subjected to an effusion measurement to characterize the bonding conditions, and radioactive surface activity measurement to measure the radioactive surface activity due to the beta emission of the occluded tritium in the silica sample.

9.3 DEEP UV LASER LOCKING OF TRITIUM IN SILICA

To test the stability of tritium that had permeated into silica glass, effusion measurements were performed on samples that had been tritiated at a tritium pressure of 70 atm and a temperature of 60 °C for 20 hours. Immediately after tritium exposure and no laser exposure a sample was subjected to linear temperature ramping at a ramp rate of 10 °C/min from room temperature to approximately 600 °C in an argon purged tritium effusion monitor [54]. A concentration of 10 mCi/cm² was measured, which is equivalent to an estimated tritium atomic concentration of 0.36%. This is much lower than the value reported in hydrogen loading experiments. Lemaire et al. have reported 11% atomic concentration of hydrogen can permeate and be subsequently locked in silica fiber. The observed discrepancy is attributed to lower loading pressure and shorter loading time. The cumulative tritium evolution is shown in trace A of Figure 9.1. Most of the tritium effuses out of the sample around 200°C. The tritium effusion rate as a function of temperature is shown in Figure 9.2; this is obtained by taking the derivative of the trace in Figure 9.1. These results show that approximately 90% of the tritium effuses at temperatures below 250°C with a distinct effusion peak at 240°C. A smaller effusion peak, ~10% of the tritium, was found at 450°C. Both peaks are resolved by a Gaussian deconvolution. The low-temperature effusion peak is likely associated with the effusion of molecular tritium trapped in the glass matrix, which has a low activation energy of ~0.4 eV [133]. The high-temperature peak is likely associated with tritium bonded in –OT hydroxyl form. This supposition is based on similar degradation temperatures (300-400°C) of most fiber Bragg gratings formed by hydrogenation and 248 nm KrF laser irradiation.[124, 126] This suggests that the high-energy beta particles, which have an average energy of 5.7 keV, cause tritium to be self-occluded through beta-induced chemical reactions in the glass matrix. It is worth noting that the generation of atomic tritium

through tritium decay is negligible given its long half-life of 12.3 years. Raman studies to confirm the above have yet to be carried out.

The T₂-impregnated samples were irradiated with 20 ns laser pulses at a repetition rate of 20 Hz and a pulse fluence of 20 mJ/cm². The effusion results for irradiated samples with 700, 3000, and 4800 J/cm² total laser fluence are shown as traces B, C, and D, respectively in both Figures 9.1 and 9.2. The effects of laser irradiation are clearly evident in Figure 9.2 where more tritium is stably bonded and effuses out at higher temperatures (>300°C). The Gaussian deconvolution was used to analyze the peaks; figure 9.3 shows the analysis as an example. Assuming that the tritium effusing out at the high temperature peak is stable and chemically bonded tritium, 60% of the permeated tritium is bonded due to laser irradiation at a total fluence of 4800 J/cm². This is in contrast to the 10% bonded tritium in non-laser irradiated samples.

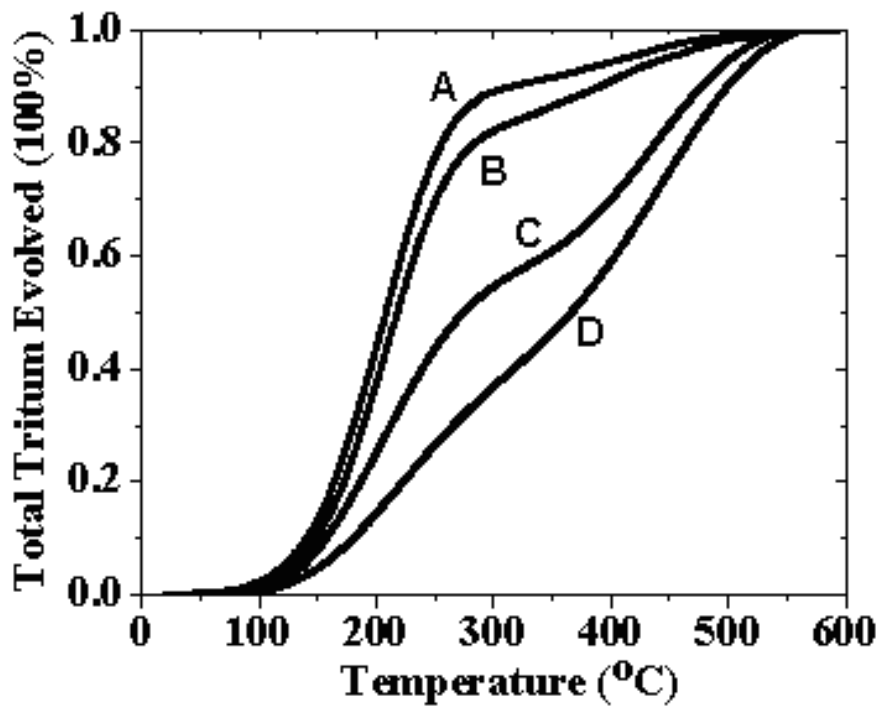


Figure 9.1 Total tritium effusion from silica films as a function of temperature. The total laser fluence is 0, 700, 3000, 4800 J/cm² for traces A, B, C and D, respectively.[82]

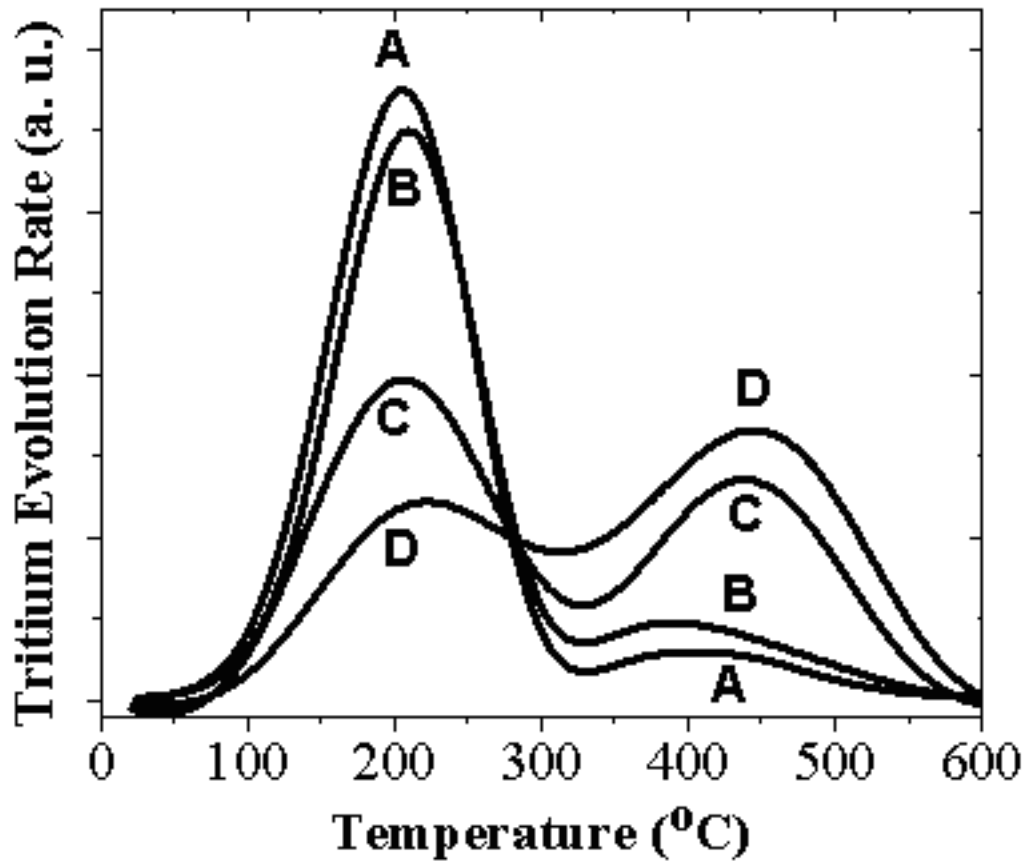


Figure 9.2 Tritium effusion rate as a function of temperature. The total laser fluence is 0, 700, 3000, 4800 J/cm² for traces A, B, C and D, respectively.[82]

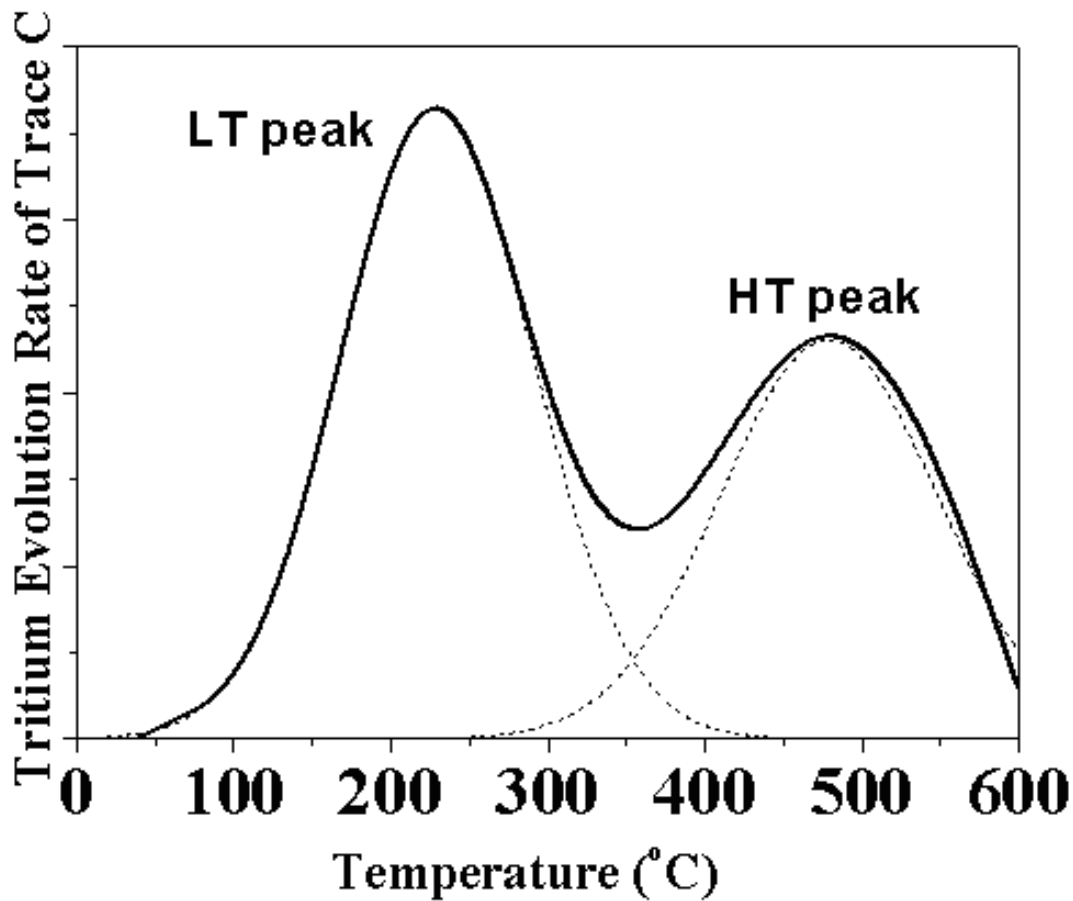


Figure 9.3 The Gaussian deconvolution of trace C, which yields a low temperature (LT) peak and a high temperature (HT) peak.

Figure 9.4 shows a linear relationship between the percentage of bonded tritium and the accumulated laser fluence. The non-saturated relationship suggests that more tritium can be bonded in silica with a further increase in the accumulated laser fluence. The laser locking results are also qualitatively consistent with the results of laser irradiation studies in hydrogen-loaded silica fiber of identical composition[124]. The accumulated fluence of 4800 J/cm^2 at 248 nm

leads to the formation of 0.1 to 0.4 atm% (1000 to 4000ppm) -OH bonds in hydrogen-loaded 3% Ge-doped silica fiber [126].

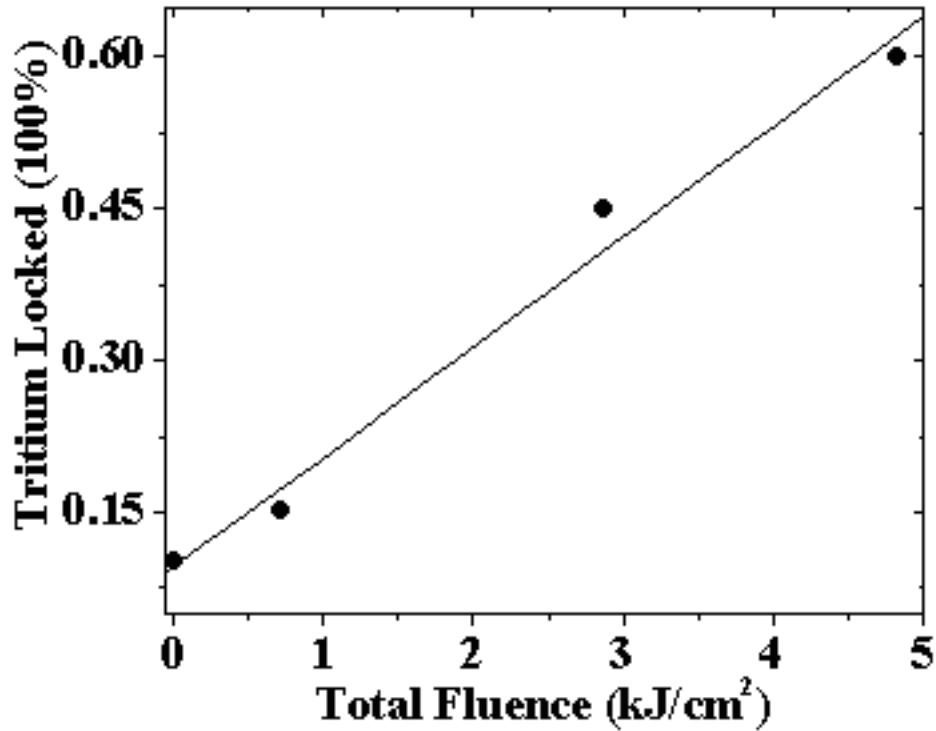


Figure 9.4 Percentage of tritium occluded in silica as a function of the total laser fluence.[82]

9.4 TRITIUM SELF-LOCKING IN SILICA

The demonstration of laser locking of tritium in silica suggests that tritium can be locked on-chip as a micro-power source. However, the laser process window is also limited by a “self-locking” process illustrated in trace A of Figure 9.1 and 9.2. The 20-hour tritium loading process has led

to 10% tritium locked in glass matrix without any laser irradiation. This self-locking effect is further manifested in Figure 9.5, for a tritiated sample kept at room temperature for 2 weeks. The effusion measurements revealed a total tritium concentration of 6.3 mCi/cm^2 in the sample, suggesting 37% of the original tritium in the sample outgassed as molecular tritium. For the remaining tritium in silica, the effusion result shown in Figure 9.5 indicates that about 30% of the original tritium, in contrast with 10% in trace A, was stably locked and effused out at high temperature. A distinct effusion peak near 450°C is consistent with effusion peaks formed by the UV laser irradiation as shown in Figure 9.2. Figure 9.5 provides appealing evidence of the formation of $-\text{OT}$ bonds, likely catalyzed by high energy electrons from tritium decay.

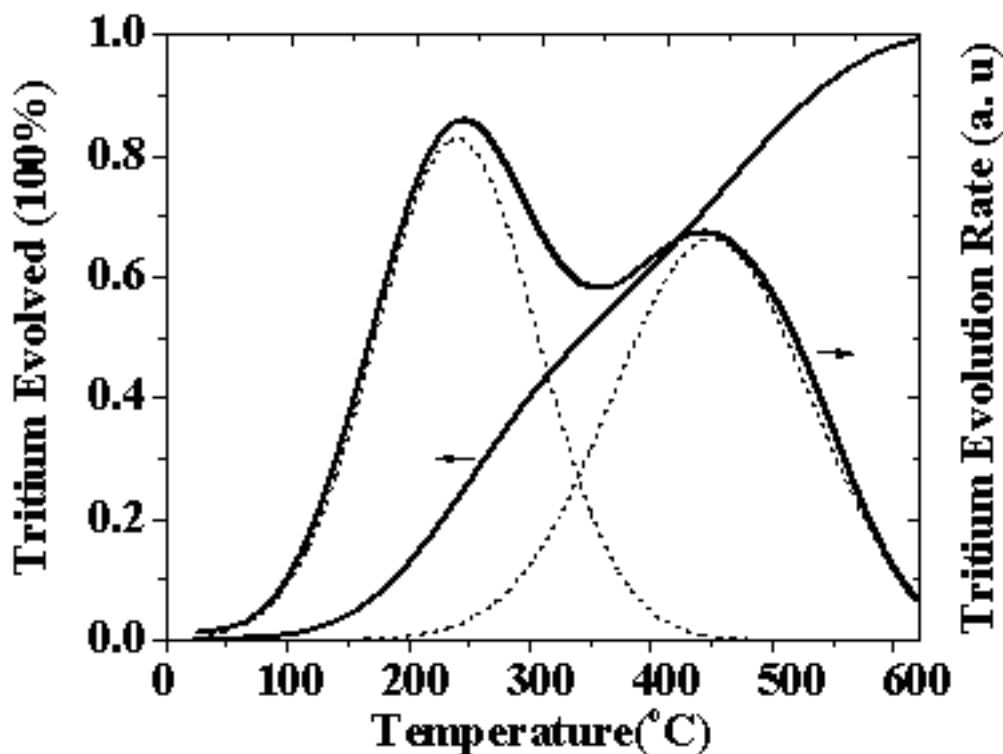


Figure 9.5 Tritium effusion from a tritiated silica film stored at room temperature for 2 weeks post high-pressure tritiation. Gaussian deconvolution shows two peaks at 240°C and 450°C . [82]

9.5 TRITIATED SILICA AS A COLD ELECTRON SOURCE

Tritium locked in silica film provides potentially a safe and localized on-chip energetic electron source for capacitor charging, molecular excitation and ionization, and for micro-nano power production amenable to a wide array of applications.

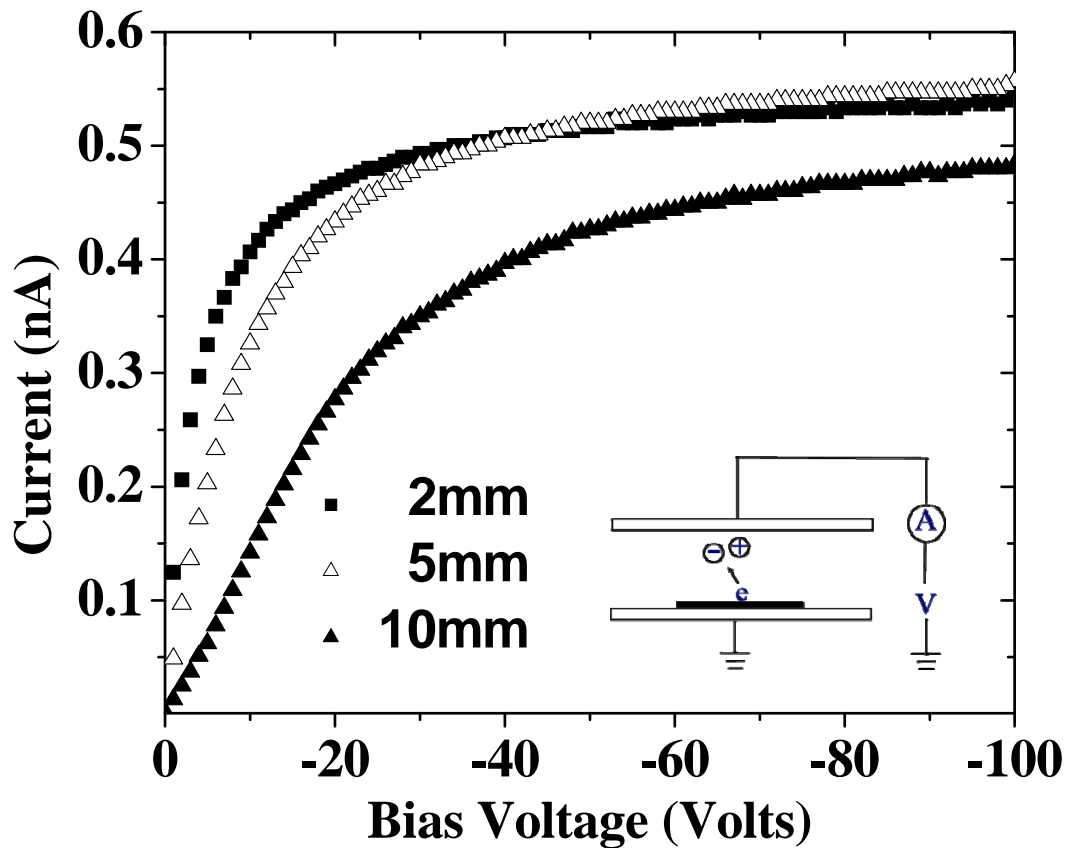


Figure 9.6 Ionization current due to a 0.5 cm^2 tritiated silica sample in air as a function of the bias voltage. The air gap is set at 2, 5, and 10 mm.[82]

Figure 9.6 illustrates a simple example of molecular ionization using the laser-locked tritium on-chip high-energy electron source. A 0.5 cm^2 tritiated silica film was placed between two metal electrodes with a potential difference applied by an external voltage source. High-energy electrons emitted by on-chip tritium ionize the ambient gas molecules and thus result in the measured ionization current. Figure 9.6 shows the ionization current as a function of the applied bias voltage for three different electrode-gap distances of 2 mm, 5 mm, and 10 mm.. For the saturated current of 500 pA shown in Figure 9.6, the effective surface activity is estimated to be 1 mCi/cm^2 in contrast to the total tritium dosage of 10 mCi/cm^2 in the $8 \text{ }\mu\text{m}$ glass films. This is due to the short range of beta particles in solids; in silica the average and maximum range are $0.4 \text{ }\mu\text{m}$ and $2 \text{ }\mu\text{m}$, respectively. Such on-chip ionization sources could be useful for on-chip micro-gas or micro-particle analyzers.

9.6 SELECTIVE LOCKING OF TRITIUM IN SILICA

The laser locking of isotope presented in this chapter promises an intriguing potential of nuclear micro-engineering for on-chip applications. By irradiating samples through a photolithography mask, the isotope can be selectively locked in silica glass film in a stable $-\text{OH}$ form. A subsequent thermal annealing process at 300°C will drive all unreacted molecular tritium out of silica glasses. Isotope micro-power sources in micron scale can be monolithically integrated on-chip with micro-electronic circuits, MEMS units, and microfluidic devices for a wide array of applications. This nuclear micro-engineering process is illustrated in Figure 9.7.

Since 5.7 keV high-energy electrons can travel up to 2 μm in silica matrix, the minimum size of an isotope power unit is in the order of 4 μm . Due to this small travel distance of the beta particles, the thickness of tritiated silica film between 1-3 μm will be sufficient to achieve the maximum surface activity. This suggests that the high-pressure tritium loading time could be substantially shortened to minimize the self tritium locking. The nuclear micro-engineering process opens the door to integrate the power source and the devices all on a single chip.

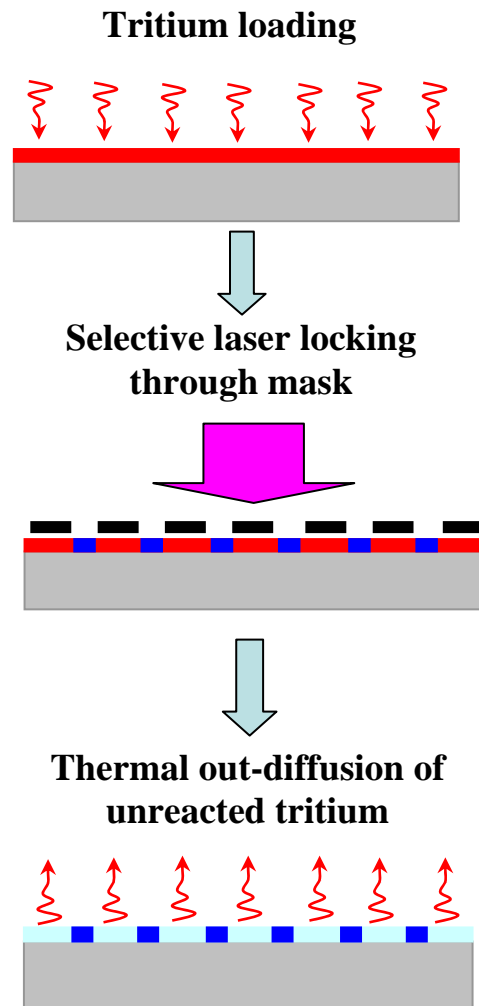


Figure 9.7 The processing of the nuclear micro-engineering in silica employing high pressure tritium loading, UV laser irradiation and thermal effusion.

9.7 SUMMARY

In summary, this chapter presents tritium incorporation in silica through the high pressure tritium loading and UV laser irradiation. Using 248 nm KrF laser irradiation, 60% tritium has been stably locked in silica films on silicon substrates. Effusion experiments indicate that laser-locked tritium is stable up to 400°C in contrast to an effusion temperature of 200 °C for tritiated samples without laser treatment. This work demonstrates a safe and simple approach to integrate radioactive micro-power sources on-chip for MEMS and micro-electronics applications.

Employing UV laser irradiation through a photolithography mask, tritium can be selectively locked in silica in micron scale. This nuclear micro-engineering process can be potentially interesting and useful in MEMS and microelectronic devices.

10.0 NUCLEAR MICRO-ENGINEERING USING METAL TRITIDES

10.1 INTRODUCTION

The MEME/NEMS (micro/nano-electromechanical systems) and nanotechnologies have brought revolutionary changes in science and engineering especially in the last two decades. As the trend of “small is better”, a lot of miniaturized devices have been introduced with advantageous properties. Taking advantage of the MEMS technology the nuclear engineering, which has long been used in power generation, medical imaging and sensing[134], can be pushed into the micron scale. In last chapter, it is described a nuclear micro-engineering process using UV laser to selectively lock tritium in silica. In this chapter, a more general method is demonstrated to integrate radioisotope on-chip in form of metal tritides through the photolithography and post-tritiation technique. This method is flexible and compatible with the semiconductor processing and VLSI integration. The scandium tritides also have higher radiation activity than the tritiated silica by an order in magnitude. The micro-engineered radioisotope on-chip can enable a series of applications. For example, in biomedicine this micro-radiator can be used in cellular diagnosis which may potentially be useful for cancer therapy and drug development. In industry, it can be used to build the gas and particle sensors with dramatically shrinking in size. In the following section, we will describe this nuclear micro-engineering process and exhibit its application as on-chip gas chromatography sensor.

Gas sensors using ionization principle[135, 136] with radioisotopes have been used extensively for a variety of applications. The ionization principle smoke/particle sensors have

been using for decades utilizing alpha radiation source. Those sensors are usually in a parallel planar or cylindrical configuration; we can call them three dimensional (3D) sensors. Recently, a compact ionization detector using beta source having bipolar and unipolar regions was reported[137, 138]. Because the beta particles have less kinetic energy, the sensor can be built smaller without losing any responsivity. Efforts have been made to further shrink the size of the sensor using novel materials such as carbon nanotubes to make the ionization sensor[139]. Here, utilizing the nuclear micro-engineering process, we demonstrate a micro-scale planar ionization sensor, in which the radioisotope source and accessory circuit are integrated on a chip to realize a two-dimensional (2D) ionization sensor. The 2D ionization sensor in millimeter scale and micrometer scale are presented. The working principle of the planar sensor is illustrated in Figure 10.1. The radioisotope, which will be beta source here, emits high energy particles through nuclear decay and ionizes the gas, and the electrical field applied through the integrated circuit will collect electron ion pairs and measure a current. The current is a measurement for the sensing.

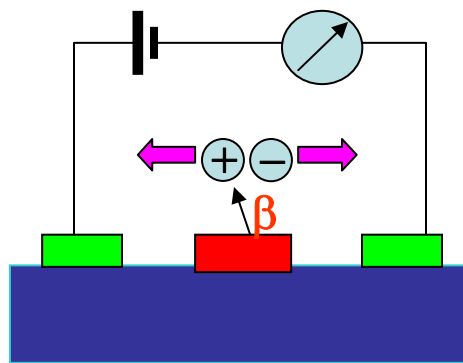


Figure 10.1 The schematic of the on-chip sensing device.

Metal tritide is used as radiation source in this on-chip sensor. Tritiated materials were proved to be applicable in sensing devices [137]. Utilizing the photolithography technique the tritium getter metal can be patterned on the substrate. The metal will further be tritiated through the post-tritiation technique, which is developed to tritiate the materials by exposing those in tritium gas at an elevated temperature as described in Chapter 4.[57, 82] The candidate metals are titanium, palladium, nickel and scandium. In previous study, we have proved that scandium is a good candidate in tritiation through the high temperature high pressure gas exposure process. The ScT alloy will form by tritiation at 250 °C in tritium gas. The surface activity is about 15 mCi/cm² for a 300 nm thick ScT.

10.2 FABRICATION OF THE ON-CHIP MICRO-SENSOR

In the fabrication of the planar ionization sensor, the pattern is integrated on the silicon nitride substrate through the photolithography and thermal evaporation process. The processing of the chip is illustrated in Figure 10.2. Two photomasks were designed for the micro-chip fabrication; one is for the aluminium layer and the other is for the scandium layer. The scandium is the tritium getter and the aluminium works as the accessory circuit. The processing of the micro-chip began by spin-coating the positive photoresist with a thickness of about 2 µm. Next to a light exposure through a photomask, a subsequent bake and photoresist development process removes the exposed part and leaves the desired pattern on the substrate. A layer of aluminium was thermally evaporated on top of the developed photoresist with a thickness of around 300 nm. The Al-coated sample was then rinsed in acetone to lift off the unwanted photoresist. Through the

procedures above, the patterning of the aluminium layer is accomplished. Next another layer of positive photoresist was recoated on top of the substrate with a thickness about 2 μm , thick enough to cover the Al layer. By repeating the above procedures, the scandium layer was also patterned on the wafer. Proper alignment marks were made on the photomask to ensure that the two series of metal patterns were made at the proper positions.

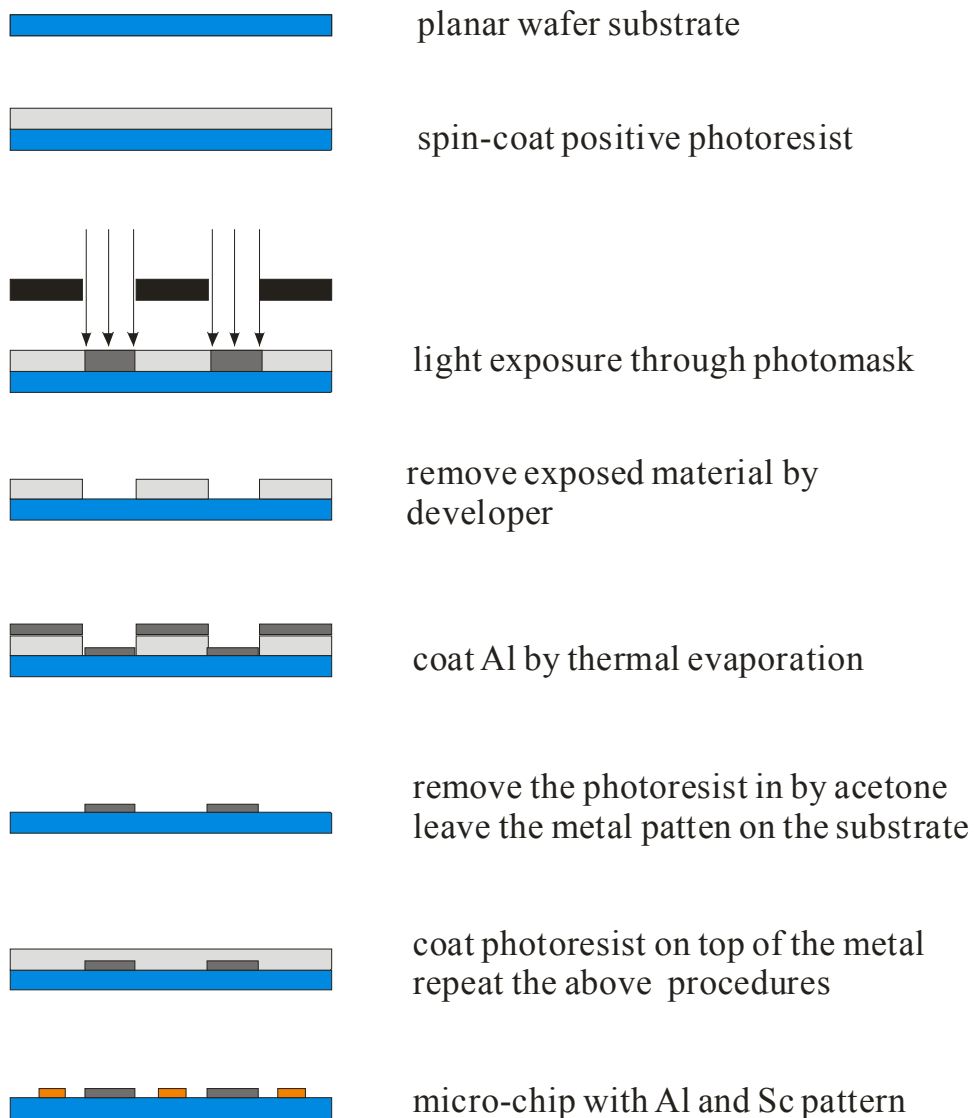
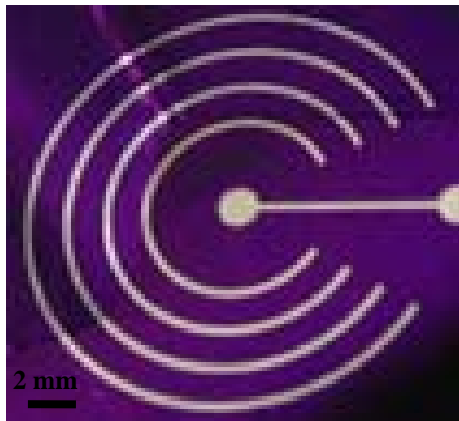
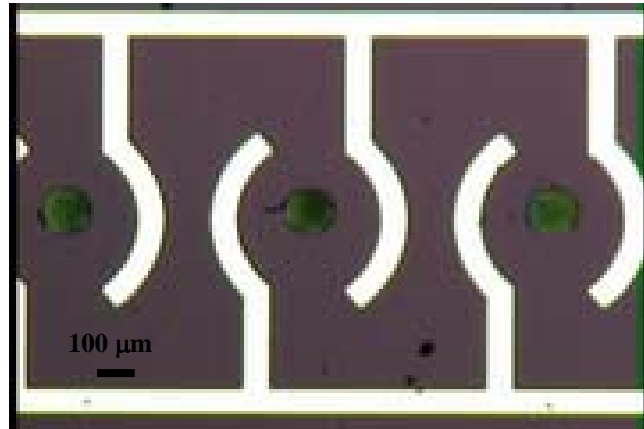


Figure 10.2 The processing of the micro-chip.

Upon the completion of the patterning, the chip was exposed in tritium gas of 250 °C, 10 bars for 1 day. The tritiated chip was stored in a ventilating fumehood for 1 day for possible outgassing before they were subjected to further measurement. A few different configurations are designed in two scales: millimetre scale and micrometer scale. Figure 10.3a shows a planar sensor in millimetre scale and Figure 10.3b shows an array of planar sensor in micrometer scale. In Figure 10.3a, the white arcs and lines are aluminium with a width of 0.5 mm, and the spacing between the lines is 2 mm. The golden-like arc is the scandium tritide source. In Figure 10.3b, the aluminium arc and lines are in width of 50 μm . The diameter of the golden-like source disc is 100 μm , and the spacing between the source and arc is also 100 μm . In these millimetre and micrometer sensors, the scandium tritides work as the radiation sources, while the aluminium pattern works as the accessory circuit.



a)



b)

Figure 10.3 The microscopic picture of the planar sensors. a), Picture of millimeter scale sensor. b), Microscopic picture of micro-scale sensor.

The tritium immobilized in the scandium tritides emits high energy beta particles through nuclear decay and the betas ionize the gas around. Through the aluminium circuit a forced electrical field is applied by a bias voltage, the electrical field sweeps out the electron-ions and the measured current can work as a signal for sensing. The ionization based vacuum gauge and gas chromatography work similarly as described above. While those sensors are in a bulky three dimensional configuration, the ionization sensor on a chip has not yet been practised. Using the two dimensional design the size of the sensor decreases dramatically. Measurements are performed in surrounding environment in air, as well as in argon and helium.

10.3 EXPERIMENTAL TEST

10.3.1 The 3D Ionization Sensor

Prior to the tests of the 2D ionization sensor, the scandium tritide source was used to build a 3D sensor to test its viability in working as radiation source in sensing, and the results will also be used as a reference for the subsequent tests for the 2D sensors.

The 3D ionization sensor is configured in two parallel metal plates. In the 3D ionization sensor, the scandium tritide film works as the radiation source and also serves as one of the electrodes. The radiation source emits high energy beta particles and ionizes the gas. The area of the scandium tritide film is about 3 cm². In ambient environment, the ionization current is measured at different air gaps. It is noted that the saturation current is the function of the electrode distance due to the range of the betas in the air. The saturation current as a function of the distance in air is shown as Figure 10.4. The maximum saturation current is obtained at

around 3 mm. Considering that the maximum range of the tritium in air is 4.5-6 mm, the obtainment of the maximum signal at 3mm implies that the beta energy is partially consumed in the metal and secondary electrons are created. Using this maximum saturation current the surface activity of the scandium tritide is calculated to be 15 mCi/cm².

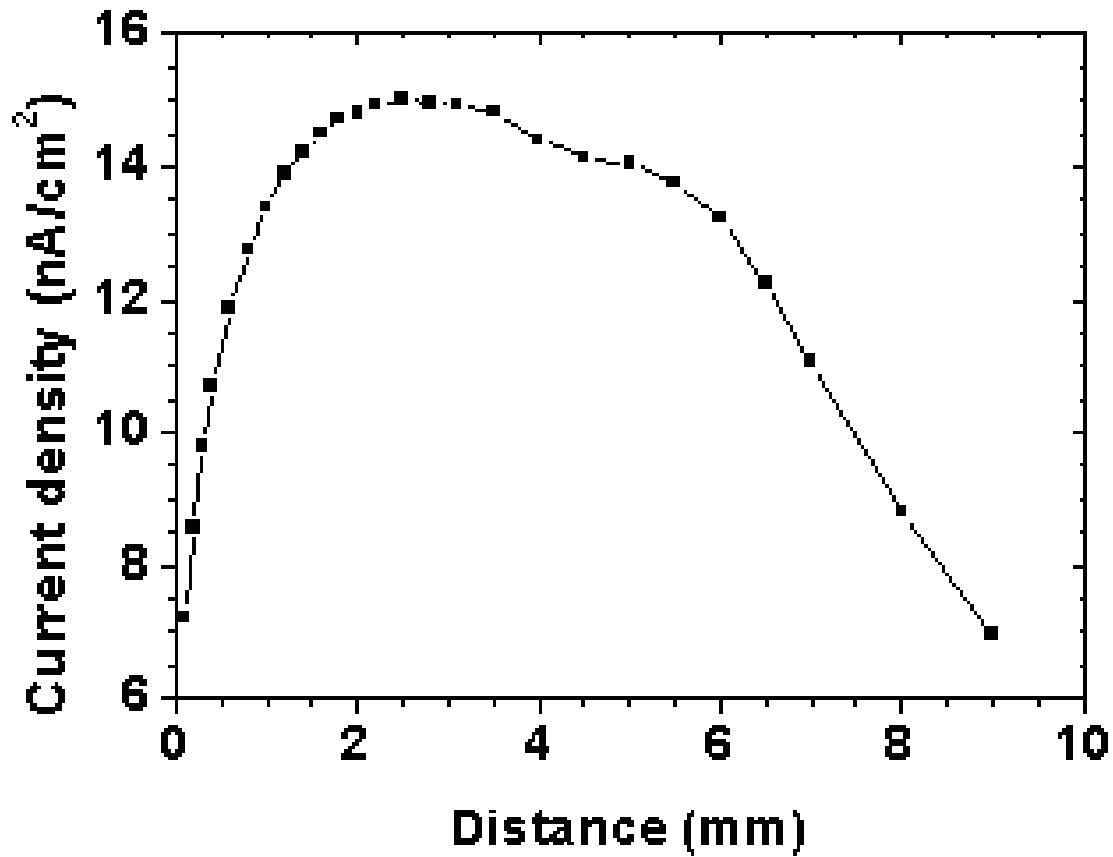


Figure 10.4 The collected current density in SAM at a biased voltage of 100 V as a function of the air gap.

Besides the air, the measurements are also performed in argon and helium. The argon and helium are chosen for they respectively have relatively small and large radiation ionization

energy among the readily available gases. The radiation ionization energies of the argon, helium and air are listed in Table 10.1. The measurements using argon and helium are performed using an aluminium box with gas import and export on it. The electrical lines are connected through an electrical fitting on the box. Before the measurement, the box is purged with argon or helium for 15 minutes

The current responses in argon and helium were studied at two different electrode gaps, 3 and 6 mm. The results are shown in Figure 10.5 a) and b), respectively. The curves measured in air are also shown in the figures. Higher current is measured in argon than in air due to the smaller ionization energy of argon. However, at 3mm distance lower current is measured in helium and in 6mm the current is higher. That is because the tritium betas have different transverse range in different gases. The transverse ranges of tritium betas in air, argon and helium are listed in Table 10.1. The different nature of each gas results in different radiation ionization energy and cross section, thus results in different transverse range of betas. At 3mm distance the beta energy has not been completely consumed in helium due to the small cross section before the betas reaches the electrodes, thus a smaller current is measured. In general, the measured current signal is different associating with different gas; that is used as a signature of each gas in gas chromatography.

TABLE 10.1 Radiation ionization energy and transverse range of tritium betas in air, argon and helium.

	Air	Argon	Helium
W-value (eV)	33.7	26.2	41.9
Range (mm)	4-6	10	30

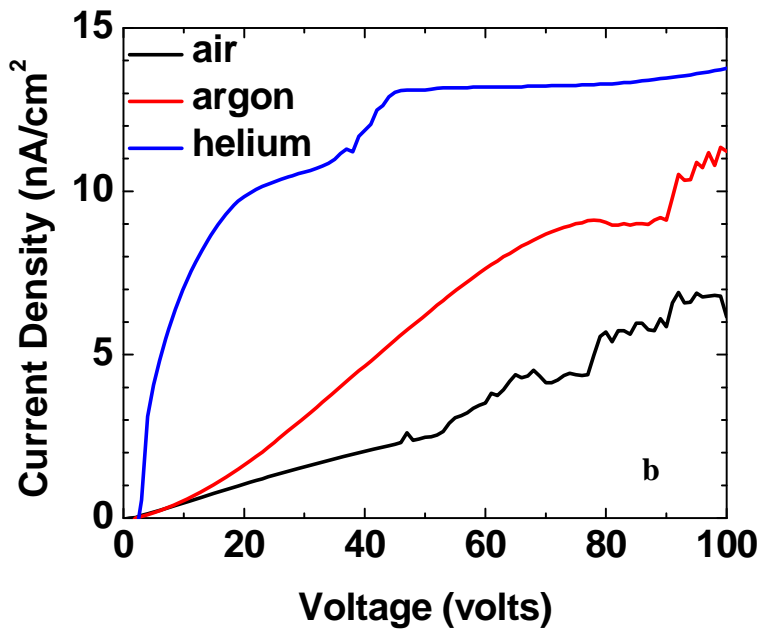
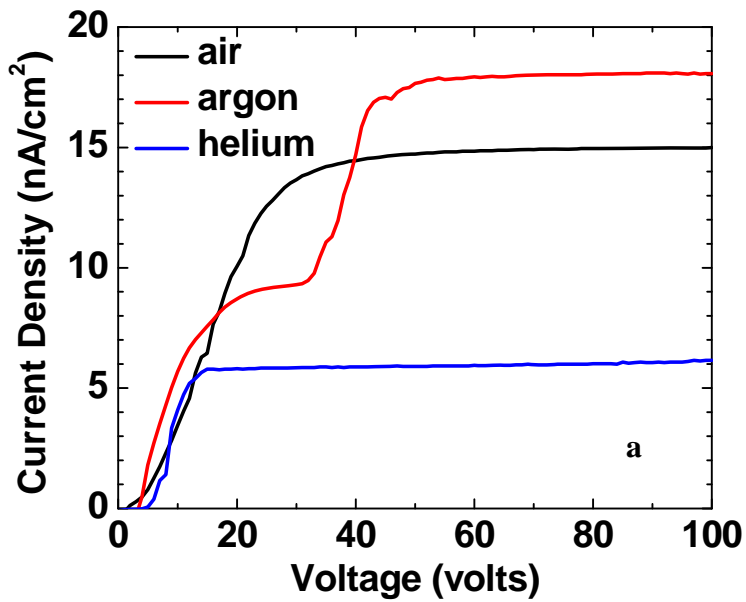


Figure 10.5 The collected current density from the ScT thin film as a function of the biased voltage measured by the SAM at an gas gap of 3mm a) and 6mm b) for air, argon and helium respectively.

10.3.2 The 2D Ionization Sensor

The test of the 2D sensor (Figure 10.3a) started by measuring the current response at biased voltages. The connection of the measurement is illustrated as an inset in Figure 10.6. The inner disc and the ScT arc are both grounded. Arcs 1 to 4 are connected to positive voltage to perform the measurement. The bias voltage is up to 100 V. The signal of the millimeter sensor is shown in Fig. 10.6.

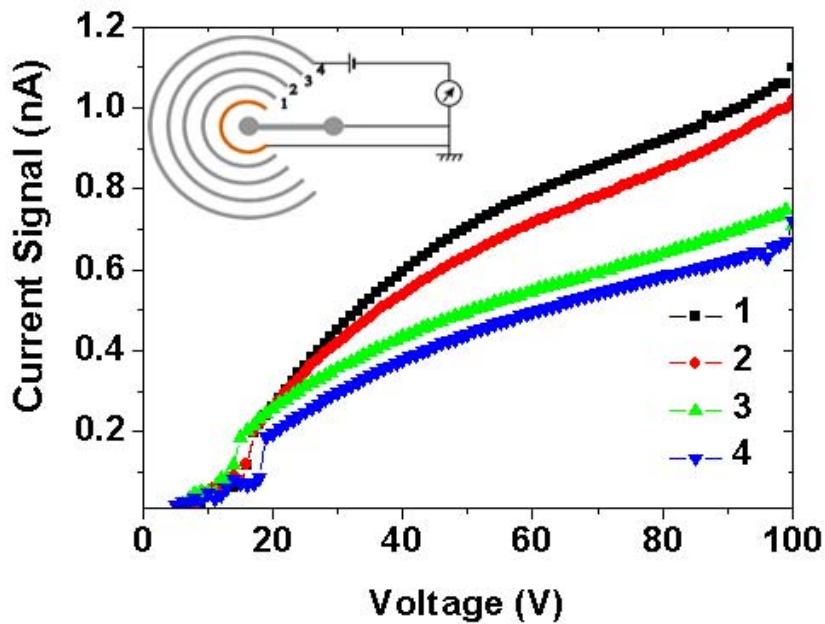


Figure 10.6 Current as a function of the bias voltage for electrodes at different distances.

As shown in Figure 10.6, the current increase as the voltage increases. The IV curves in Figure 10.6 are analogous to that obtained from the 3D configuration. This indicates that the working principle in the 3D parallel capacitor configuration works as well as in the 2D planar

configuration. The results in Figure 10.6 also show that signal increases quickly at low voltage and the growing becomes slower when the electrical field is strong enough. While it differs from the 3D result that the current keeps increasing and doesn't saturate. This is due to the open field configuration in this 2D sensor; the high energy particles can traverse farther than that between two parallel plates with fixed distance. A stronger field can collect more electron-ion pairs as the voltage increases. The effect of the electrode distance is clearly exhibited in the figure. The measurement is performed in air. The results show that a narrower distance which results in a stronger electric field yields a larger signal as expected.

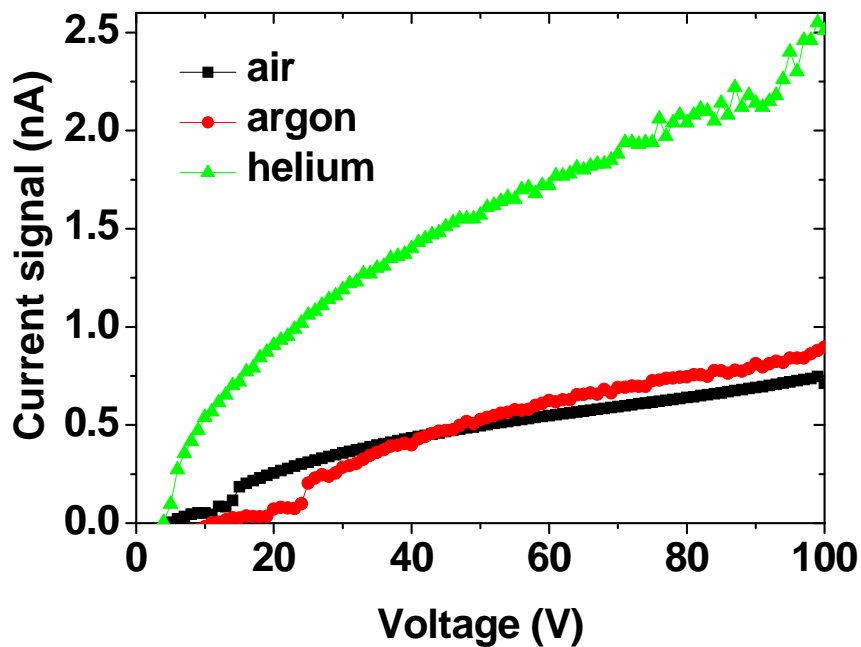


Figure 10.7 Current signals as a function of the bias voltage in air, argon and helium.

Besides the surrounding gas of air, the measurements are also performed in argon and helium. The responses of the sensor in argon and helium as well as in air are shown in Figure

10.7; in the measurement the positive voltage is applied to arc 4. Similar results are obtained as the 3D ionization sensor, though smaller currents are obtained due to reduction in radiation source. Higher current is measured for argon in comparison with air due to smaller ionization energy of argon. Due to the open space above the sensor, a relatively large signal is obtained for helium. The transverse range of the betas in helium is about 30 mm, and the open space enables the sufficient consumption of the beta energy in helium. These curves are similar as the one in the 3D configuration with electrode distance of 6mm. The results indicate the ionization based sensor also works in a planar configuration.

10.3.3 The Micro-scale Ionization Sensor

In last section, the results indicate that the ionization principle is also applicable for a planar configuration. The sensor in micro-sensor is then tested as the ionization sensor in shrunk sizes to exam its applicability as a microscale sensor. Voltage up to 100 V is applied between the upper and lower line (Fig. 10.3b). The current response is shown in Figure 10.8, which shows the current signal in air, argon and helium. The results are similar as obtained in 3D configuration (Fig. 10.5b) and in the millimetre sensor (Fig. 10.7). This shows that the ionization sensor works well in micron scale.

As a demo of this gas sensor, the response of the sensor in air when a flux of helium is introduced is shown in Figure 10.9. A voltage of 100 V is applied and a stable current is measured before a helium flux is introduced. As the sudden helium flux is introduced. The current rises rapidly and it drops back as the helium flux is removed.

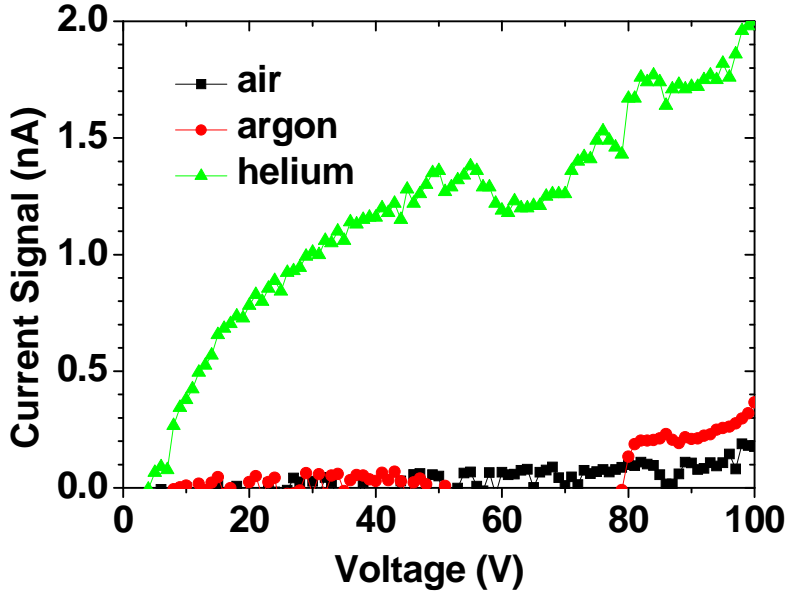


Figure 10.8 Current signal of the microscale as a function applied voltage in air, argon and helium, respectively.

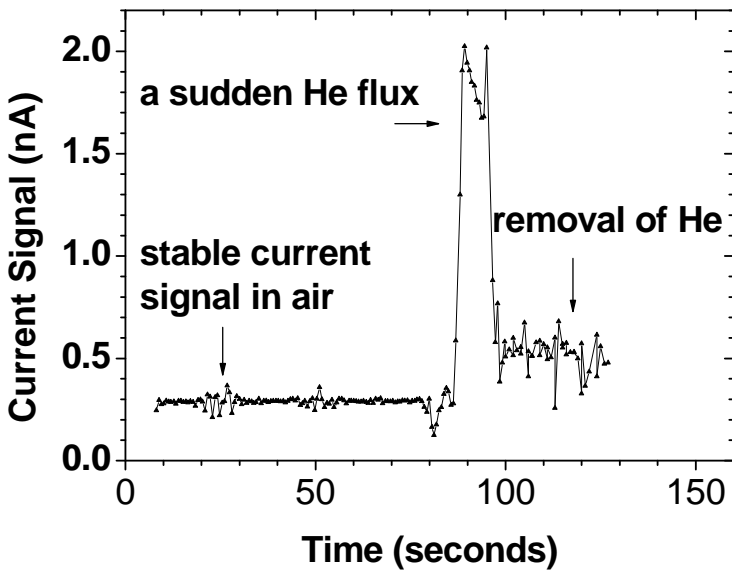


Figure 10.9 Response of helium flux introduced into the microsensor in air.

10.4 SUMMARY

Our studies demonstrated the nuclear micro-engineering on-chip for the first time, where the radiation source is integrated on-chip and planar ionization sensor in microscale has been developed. The sensors exhibit the viability in gas chromatography as a 2D configuration MEMS device. The results represent an advance of nuclear engineering in micron scale. Our approach is flexible and compatible with current semiconductor and VLSI processing. We believe that this demonstration of nuclear micro-engineering process open the door to a broad research area which will produce useful devices in micro- to nano- scale with various applications.

11.0 CONCLUSIONS AND FUTURE WORKS

11.1 CONCLUSIONS

In the last decades, we have been experiencing rapid progresses in semiconductor, MEMS, and nano-technology. Taking advantage of those, this thesis pushes the nuclear engineering into the small scale. Other than the traditional power generation utilizing the fission process, the radioisotope is immobilized in semiconductor/metal, or integrated on a chip to realize a micro-power source, or on-chip radiator.

A high temperature and high pressure gaseous tritium exposure apparatus was constructed. The tritium loading apparatus can provide a tritium gas environment at pressures of up to 200 bars and temperatures of up to 300 °C. This system provides a chance for the study of the tritium interaction with various materials. Stable incorporation of high density tritium in silicon, silica, carbon nanotubes, was achieved. Effusion measurements show the presence of stable tritium in silicon, silica and CNTs up to 400 °C. The concentration of tritium locked in those materials with a density is up to 20 at.%. This work provides a series of tritiated materials which provide us cold electron sources. Those cold electron sources are amendable to ranges of applications in various occasions.

Utilizing the tritiated materials, a number of novel micro-power sources are explored. The scandium tritide powered betavoltaic battery using the contact potential difference principle

was demonstrated. It is a low cost battery which can provide nanowatt power. Three-dimensional betavoltaics using the porous silicon diode were explored as a volume effect battery powered by gaseous tritium.

The tritium is also introduced into the nano-materials, carbon nanotubes and ZnO nanowires. Carbon nanotubes are found to be a good tritium carrier and a density of 0.5 wt.% was achieved. The beta-luminescence of the ZnO nanowires was studied. The emission of green light is observed.

The UV laser irradiation was used to selectively lock the tritium in silica in micron scale. Using the MEMS approach, the embedded on-chip isotope micro-sources were created as localized ionization sources for chip-scale sensors and radiators. The nuclear micro-engineering was demonstrated.

This thesis work laid ground work to develop micro-power source that can dramatically improve the operational longevity of micro- and nano- systems for unattended applications. These devices offer important alternative energy sources for exploration, military, and implanted applications. The extension of nanotechnology into nuclear engineering will also generate research and engineering opportunities in their respective areas of science and technology.

11.2 FUTURE WORK

In this thesis study, betavoltaic experiments were performed on a 3-D macro-porous silicon *pn*-junction. Such structures were fabricated to overcome some of the limitations of two-dimensional betavoltaic batteries caused by the limited surface area of the *pn*-junctions. A continuous *pn*-junction is created along the surface of the entire porous network. Using standard electrochemical etch techniques deep channel pores are prepared in a crystalline silicon wafer [7]. For the cell with a size of 1 cm by 2cm, the output power increases as the tritium pressure went up from the vacuum level and reached the optimized value at 0.8 atm. An open circuit voltage of 22 mV and a short circuit current of 1.5 μ A were measured. The 3D diode was proved to increase the power output and energy efficiency in comparison with the traditional 2D diode.

However, the absolute value of the efficiency is estimated to be 0.1%. This low energy conversion efficiency is probably due to a large density of surface recombination centers produced by the electrochemical etching used to produce porous structures. To eliminate this problem and to improve the surface quality of the devices, we propose a 3D diode with high-quality junction fabricated by a dry process to improve the efficiency and power output. Such structures will be fabricated by a deep trench etching and a POCl_3 doping process to produce *pn*-junctions. A SEM picture of the trenched silicon is shown in Figure 11.1a. The fabrication starts from a 300 μ m p^+ substrate, a *p*-layer is then epitaxially grown on the p^+ layer. The deep trench will be fabricated in the *p*-layer. The depth of the trench ranges from 1 to 100 μ m to magnify the surface area up to 100 times. The n^+ layer is made using POCl_3 on the internal surface. The metal contact will be coated on the top and back side of the device. Tritium

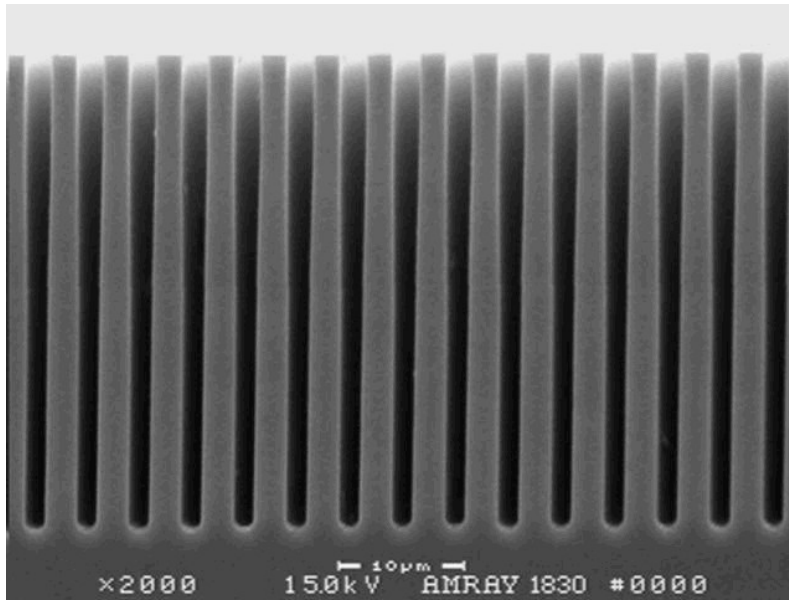
absorbers can be deposited in the trenches. The proposed structure is shown in Figure 11.1b. The tritium getters can be either metal hydrides such as titanium and scandium or a-Si deposited by a CVD process. If a 300 nm Ti film is deposited on the surface, an effective surface activity of 60 mCi/cm² will act on the silicon *p-n* junction; the activity per square centimeter sample will be 6 Ci. The ionization energy of the crystalline silicon is ~3.8 eV. A beta particle with a kinetic energy can generate ~1500 electron-ion pairs. The maximal current density will be ~63 μA/cm².

The output voltage will be determined by the quality of the junction. A junction of high quality will yield very low leakage current, which consequently leads to high open circuit voltage. The open circuit voltage is given by

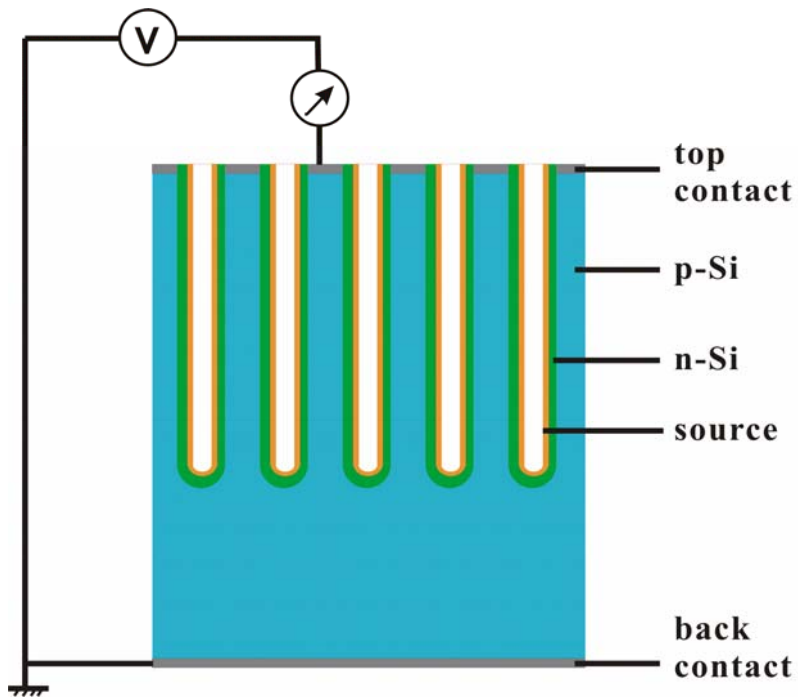
$$V_{oc} = \frac{nkT}{q} \ln\left(\frac{I_{\beta}}{I_0} + 1\right) \approx 25mV \times \ln\left(\frac{I_{\beta}}{I_0} + 1\right)$$

(11.1)

I_0 is the leakage current determined by the quality of diode, I_{β} is the closed-circuit current. Figure 11.2 shows a plot of open circuit voltage (V_{oc}) vs. the leakage current (I_0) ranging from 0.5 pA to 1 nA. For a leakage current of 1 nA/cm², an open circuit voltage of 100mV is expected. If the leakage current goes down to 1 pA/cm², the open circuit voltage increases to 380 mV. Assuming a fill factor of 0.5, an output power of 14 μW/cm² is expected, which will be a remarkable improvement.



a)



b)

Figure 11.1 a) The SEM side view of the trenched silicon. b) The proposed betavoltaic cell using a 3D diode.

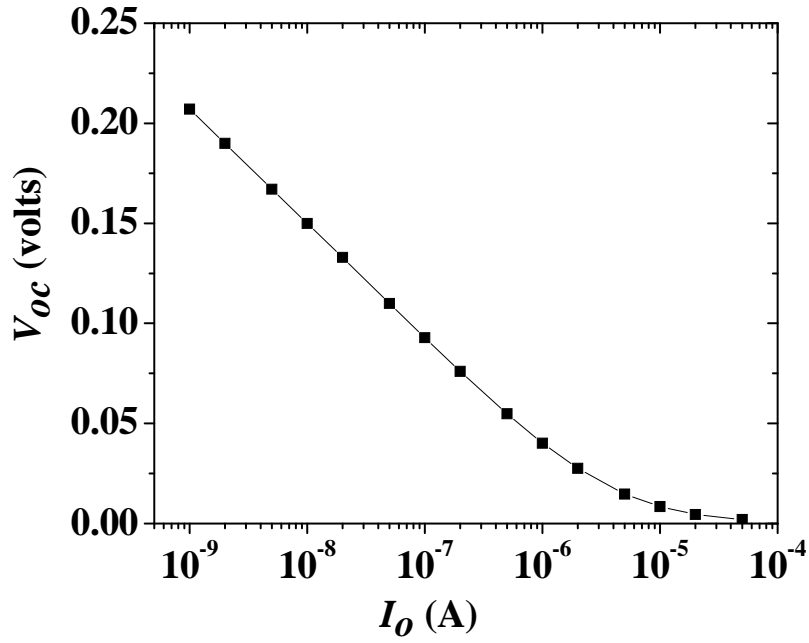


Figure 11.2 Plot of open circuit voltage (V_{oc}) vs. the leakage current (I_o) per unit area (1 cm^2).

BIBLIOGRAPHY

- [1] T. Pichonat and B. Gauthier-Manuel, "Recent developments in MEMS-based miniature fuel cells," *Microsystem Technologies-Micro-and Nanosystems-Information Storage and Processing Systems*, vol. 13, pp. 1671-1678, Jul 2007.
- [2] S. Kal, "Microelectromechanical systems and microsensors," *Defence Science Journal*, vol. 57, pp. 209-224, May 2007.
- [3] H. Schenk, A. Wolter, U. Dauderstaedt, A. Gehner, and H. Lakner, "Micro-opto-electro-mechanical systems technology and its impact on photonic applications," *Journal of Microlithography Microfabrication and Microsystems*, vol. 4, pp. -, Oct-Dec 2005.
- [4] A. B. Frazier, R. O. Warrington, and C. Friedrich, "The Miniaturization Technologies - Past, Present, and Future," *IEEE Transactions on Industrial Electronics*, vol. 42, pp. 423-430, Oct 1995.
- [5] T. A. Ameel, R. O. Warrington, R. S. Wegeng, and M. K. Drost, "Miniaturization technologies applied to energy systems," *Energy Conversion and Management*, vol. 38, pp. 969-982, Jul-Sep 1997.
- [6] T. Kostaske, N. P. Kherani, P. Stradins, F. Gaspari, W. T. Shmayda, L. S. Sidhu, and S. Zukotynski, "Tritiated amorphous silicon betavoltaic devices," *IEE Proc.: Circuits Devices Syst.*, vol. 150, pp. 274-281, Aug 2003.
- [7] W. Sun, N. P. Kherani, K. D. Hirschman, L. L. Gadenken, and P. M. Fauchet, "A three-dimensional porous silicon p-n diode for betavoltaics and photovoltaics," *Adv. Mater. (Weinheim, Ger.)*, vol. 17, pp. 1230-1233, May 13 2005.
- [8] N. P. Kherani, T. Kostaske, S. Zukotynski, and W. T. Shmayda, "Tritiated Amorphous-Silicon for Micropower Applications," *Fusion Technology*, vol. 28, pp. 1609-1614, Oct 1995.
- [9] N. P. Kherani and W. T. Shmayda, "Radioluminescence Using Metal Tritides," *Zeitschrift Fur Physikalische Chemie-International Journal of Research in Physical Chemistry & Chemical Physics*, vol. 183, pp. 453-463, 1994.

- [10] M. Saljoughian and P. G. Williams, "Recent developments in tritium incorporation for radiotracer studies," *Current Pharmaceutical Design*, vol. 6, pp. 1029-1056, Jul 2000.
- [11] R. J. Hawryluk, et. al: A 20 year retrospective," *Physics of Plasmas*, vol. 5, pp. 1577-1589, May 1998.
- [12] A. Becker and E. Kruppke, *Z. Phys.*, vol. 107, p. 476, 1937.
- [13] W. Ehrenberg, C.-S. Lang, and R. West, "The electron voltaic effect," *Proceedings of the Physical Society (London), Section A*, vol. 64, p. 424, April 1951 1951.
- [14] W. Ehrenberg and C. S. Lang, "Probing of barrier layers with an electron beam," *Physica*, vol. 20, pp. 1137-1138, 1954.
- [15] P. Rappaport, "The Electron-Voltaic Effect in P-N Junctions Induced by Beta-Particle Bombardment," *Physical Review*, vol. 93, pp. 246-247, 1954.
- [16] W. G. Pfann and W. Van Roosbroeck, "Radioactive and Photoelectric p-n Junction Power Sources," *Journal of Applied Physics*, vol. 25, pp. 1422-1434, 1954.
- [17] P. Rappaport, J. J. Loferski, and E. G. Linder, *RCA Rev.*, vol. 17, p. 100, 1956.
- [18] H. Flicker, J. J. Loferski, and T. S. Elleman, "Construction of a promethium-147 atomic battery," *IEEE Transactions on Electron Devices*, pp. 2-8, 1964.
- [19] C. A. Klein, "Bandgap dependence and related features of radiation ionization energies in semiconductors," *Journal of Applied Physics*, vol. 39, pp. 2029-2038, 1968.
- [20] L. C. Olsen, "Betavoltaic energy conversion," *Energy Conversion*, vol. 13, pp. 117-127, 1973.
- [21] L. C. Olsen, "Review of betavoltaic energy conversion," in *NASA, Lewis Research Center, Proceedings of the 12th Space Photovoltaic Research and Technology Conference (SPRAT 12)*, 1993, pp. 256-267.
- [22] K. E. Bower, Y. A. Barbanel, Y. G. Shreter, and G. W. Bohnert, *Polymer, Phosphors, and Voltaics for Radioisotope Microbatteries*. Boca Raton, FL: CRC Press, 2002.
- [23] T. Kostas, N. P. Kherani, F. Gaspari, S. Zukotynski, and W. T. Shmayda, "Tritiated amorphous silicon films and devices," *Journal of Vacuum Science & Technology a-Vacuum Surfaces and Films*, vol. 16, pp. 893-896, Mar-Apr 1998.

- [24] S. Deus, "Tritium-powered betavoltaic cells based on amorphous silicon," in *the 28th Photovoltaic Specialists Conference Alaska*, 2000, pp. 1246-1249.
- [25] H. Guo and A. Lal, "Nanopower betavoltaic microbatteries," in *TRANSDUCERS, Solid-State Sensors, Actuators and Microsystems, 12th International Conference on*, 2003, 2003, pp. 36-39 vol.1.
- [26] R. Duggirala, S. Tin, and A. Lal, "3D Silicon Betavoltaics Microfabricated using a Self-Aligned Process for 5 Milliwatt/CC Average, 5 Year Lifetime Microbatteries," *Solid-State Sensors, Actuators and Microsystems Conference, 2007. TRANSDUCERS 2007. International*, pp. 279-282, 2007.
- [27] J. P. Clarkson, W. Sun, K. D. Hirschman, L. L. Gadeken, and P. M. Fauchet, "Betavoltaic and photovoltaic energy conversion in three-dimensional macroporous silicon diodes," *Physica Status Solidi a-Applications and Materials Science*, vol. 204, pp. 1536-1540, May 2007.
- [28] M. V. S. Chandrashekar, C. I. Thomas, H. Li, M. G. Spencer, and A. Lal, "Demonstration of a 4H SiC betavoltaic cell," *Applied Physics Letters*, vol. 88, p. 033506, Jan 16 2006.
- [29] C. J. Eiting, V. Krishnamoorthy, S. Rodgers, T. George, J. D. Robertson, and J. Brockman, "Demonstration of a radiation resistant, high efficiency SiC betavoltaic," *Applied Physics Letters*, vol. 88, p. 064101, Feb 6 2006.
- [30] R. A. Street, *Hydrogenated amorphous silicon*. Cambridge Cambridge University Press, 1991.
- [31] R. J. Walko, R. C. Lincoln, W. E. Baca, S. H. Goods, and G. H. Negley, in *Proceedings of the 26th intersociety Energy Conversion Engineering Conference*, Boston, Massachusetts, 1991, pp. 135-140.
- [32] A. G. Kavetsky, V. S. Kalinovsky, V. P. Khvostikov, V. R. Larionov, V. D. Rumyantsev, and V. M. Andreev, "Tritium-powered betacells on $Al_xGa_{1-x}As$," in *the 28th IEEE Photovoltaic Specialists Conference Alaska*, 2000.
- [33] C. Hongsberg, W. A. Doolittle, M. Allen, and C. Wang, "GaN betavoltaic energy converter," in *the 31st IEEE Photovoltaics Specialist Conference*, Orlando Florida, 2005.
- [34] "Miniature Atomic Powered Battery," *Radio and TV News*, vol. 57, p. 160, 1957.
- [35] P. E. Sims, L. C. DiNetta, and A. M. Barnett, *Proceedings of the XIII Space Photovoltaic Research and Technology*, vol. 359, 1994.

- [36] M. Sychov, A. Kavetsky, G. Yakubova, G. Walter, S. Yousaf, Q. Lin, D. Chan, H. Socarras, and K. Bower, "Alpha indirect conversion radioisotope power source," *Applied Radiation and Isotopes*, vol. 66, pp. 173-177, 2008.
- [37] E. G. Linder and S. M. Christian, "The Use of Radioactive Material for the Generation of High Voltages," *Physical Review*, vol. 83, pp. 233-233, 1951.
- [38] E. G. Linder and P. Rappaport, "Radioactive Charging through a Dielectric Medium," *Physical Review*, vol. 91, pp. 202-202, 1953.
- [39] P. E. Ohmart, "A Method of Producing an Electric Current from Radioactivity," *Journal of Applied Physics*, vol. 22, pp. 1504-1505, 1951.
- [40] A. Lal, R. Duggirala, and H. Li, "Pervasive power: A radioisotope-powered piezoelectric generator," *Ieee Pervasive Computing*, vol. 4, pp. 53-61, Jan-Mar 2005.
- [41] H. Li, A. Lal, J. Blanchard, and D. Henderson, "Self-reciprocating radioisotope-powered cantilever," *Journal of Applied Physics*, vol. 92, pp. 1122-1127, Jul 15 2002.
- [42] R. Duggirala, H. Li, and A. Lal, "High efficiency β radioisotope energy conversion using reciprocating electromechanical converters with integrated betavoltaics," *Applied Physics Letters*, vol. 92, p. 154101, 2008.
- [43] A. Lal and J. Blanchar, "The daintiest dynamo," *IEEE Spectrum*, vol. 41, pp. 36-41, Sep 2004.
- [44] J. R. Srour, C. J. Marshall, and P. W. Marshall, "Review of displacement damage effects in silicon devices," *IEEE Transactions on Nuclear Science*, vol. 50, pp. 653-670, Jun 2003.
- [45] N. P. Khernai and W. T. Shmayda, "Tritium-Materials Interactions," *Nuclear Science and Technology, Safety in Tritium Handling Technology, Euro Course Series*, pp. 85-105, 1993.
- [46] E. A. Evans, *Tritium and its Compounds*. New York: John Wiley, 1975.
- [47] A. B. Antoniazzi, C. S. Morton, K. P. Chen, and B. Liu, "High-pressure and high-temperature tritium apparatus for the tritiation of materials," *Fusion Science and Technology*, vol. 54, pp. 635-638, 2008.
- [48] Y. Kawamura, S. Konishi, and M. Nishi, "Adsorption isotherms of hydrogen isotopes on molecular sieves 5A at low temperature," *Journal of Nuclear Science and Technology*, vol. 37, pp. 536-542, Jun 2000.

- [49] N. H. Nickel and W. B. Jackson, "Hydrogen-Mediated Creation and Annihilation of Strain in Amorphous-Silicon," *Physical Review B*, vol. 51, pp. 4872-4881, Feb 15 1995.
- [50] W. B. Jackson and C. C. Tsai, "Hydrogen Transport in Amorphous-Silicon," *Physical Review B*, vol. 45, pp. 6564-6580, Mar 15 1992.
- [51] J. Pearson, J. W. Corbett, and M. Stavola, *Hydrogen in Crystalline Semiconductors*. New York: Springer-Verlag, 1992.
- [52] W. Beyer, "Diffusion and evolution of hydrogen in hydrogenated amorphous and microcrystalline silicon," *Solar Energy Materials and Solar Cells*, vol. 78, pp. 235-267, Jul 2003.
- [53] T. Kosterki, "Tritiated Amorphous Silicon Films and Devices," in *Department of Electrical and Computer Engineering*. vol. Ph.D Toronto: University of Toronto, 2001.
- [54] N.P.Kherani, R. B. Gangadhar, and S.Zukotynski, "Photovoltaics: The next generation," in *30th Annual Conference of Canadian Solar Energy Society (SESCI)*, Vancouver, Canada, August, 2005.
- [55] N. P. Kherani and W. T. Shmayda, "In-Line Process Tritium Monitors," *Fusion Technology*, vol. 21, pp. 340-345, Mar 1992.
- [56] N. P. Kherani, B. Liu, K. Virk, T. Kosterki, F. Gaspari, W. T. Shmayda, S. Zukotynski, and K. P. Chen, "Hydrogen effusion from tritiated amorphous silicon," *Journal of Applied Physics*, vol. 103, p. 024906, 2008.
- [57] B. Liu, K. P. Chen, N. P. Kherani, T. Kosterki, S. Costea, S. Zukotynski, and A. B. Antoniazzi, "Tritiation of amorphous and crystalline silicon using T₂ gas," *Appl. Phys. Lett.*, vol. 89, p. 044104, Jul 24 2006.
- [58] L. S. Sidhu, T. Kosterki, S. Zukotynski, and N. P. Kherani, "Infrared vibration spectra of hydrogenated, deuterated, and tritiated amorphous silicon," *Journal of Applied Physics*, vol. 85, pp. 2574-2578, Mar 1 1999.
- [59] B. Tuck, *Introduction to Diffusion in Semiconductors*: Peregrinus, Salisbury, 1974.
- [60] S. Acco, D. L. Williamson, P. A. Stolk, F. W. Saris, M. J. vandenBoogaard, W. C. Sinke, W. F. vanderWeg, and S. Roorda, "Hydrogen solubility and network stability in amorphous silicon," *Physical Review B*, vol. 53, pp. 4415-4427, Feb 15 1996.
- [61] P. Danesh, B. Pantchev, B. Schmidt, and D. Grambole, "Hydrogen solubility limit in hydrogenated amorphous silicon," *Semicond. Sci. Technol.*, vol. 19, pp. 1422-1425, 2004.

- [62] Y. Uchida, S. C. Deane, and W. I. Milne, "Posthydrogenation of Low-Pressure Chemical-Vapor-Deposited Amorphous-Silicon Using a Novel Internal Lamp System and Its Application to Thin-Film Transistor Fabrication," *Journal of Applied Physics*, vol. 72, pp. 3150-3155, Oct 1 1992.
- [63] J. Dubeau, L. A. Hamel, and T. Pochet, "Radiation ionization energy in alpha-Si:H," *Physical Review B*, vol. 53, pp. 10740-10750, Apr 15 1996.
- [64] A. Yelon, H. Fritzsche, and H. M. Branz, "Electron beam creation of metastable defects in hydrogenated amorphous silicon: hydrogen collision model," *Journal of Non-Crystalline Solids*, vol. 266, pp. 437-443, May 2000.
- [65] S. Najar, B. Equer, and N. Lakhoua, "Electronic Transport Analysis by Electron-Beam-Induced Current at Variable Energy of Thin-Film Amorphous-Semiconductors," *Journal of Applied Physics*, vol. 69, pp. 3975-3985, Apr 1 1991.
- [66] J. A. Mcmillan and E. M. Peterson, "Kinetics of Decomposition of Amorphous Hydrogenated Silicon Films," *Journal of Applied Physics*, vol. 50, pp. 5238-5241, 1979.
- [67] W. Beyer and H. Wagner, "Determination of the Hydrogen Diffusion-Coefficient in Hydrogenated Amorphous-Silicon from Hydrogen Effusion Experiments," *Journal of Applied Physics*, vol. 53, pp. 8745-8750, 1982.
- [68] K. Murakami, N. Fukata, S. Sasaki, K. Ishioka, M. Kitajima, S. Fujimura, J. Kikuchi, and H. Haneda, "Hydrogen molecules in crystalline silicon treated with atomic hydrogen," *Physical Review Letters*, vol. 77, pp. 3161-3164, Oct 7 1996.
- [69] G. F. Cerofolini, F. Corni, S. Frabboni, C. Nobili, G. Ottaviani, and R. Tonini, "Hydrogen and helium bubbles in silicon," *Materials Science & Engineering R-Reports*, vol. 27, pp. 1-52, Apr 14 2000.
- [70] O. Blaschko, J. Pleschiutchnig, R. Glas, and P. Weinzierl, "Helium Damage in Metal-Tritium Systems," *Physical Review B*, vol. 44, pp. 9164-9169, Nov 1 1991.
- [71] N. P. Kherani and W. T. Shmayda, "Ionization Surface-Activity Monitor for Tritium," *Fusion Technology*, vol. 28, pp. 893-898, Oct 1995.
- [72] C. R. Shmayda, W. T. Shmayda, and N. P. Kherani, "Monitoring tritium activity on surfaces: Recent developments," *Fusion Science and Technology*, vol. 41, pp. 500-504, May 2002.
- [73] R. D. Evans, *The atomic nucleus*. McGraw Hill, New York, 1955.

- [74] R. Lässer, *Tritium and helium-3 in metals*. United States: New York, NY ;Springer-Verlag New York Inc., 1989.
- [75] F. Schuth, B. Bogdanovic, and M. Felderhoff, "Light metal hydrides and complex hydrides for hydrogen storage," *Chemical Communications*, pp. 2249-2258, Oct 21 2004.
- [76] N. P. Kherani and W. T. Shmayda, "Electron Flux at the Surface of Titanium Tritide Films," *Fusion Technology*, vol. 21, pp. 334-339, Mar 1992.
- [77] N. P. Kherani, W. T. Shmayda, J. M. Perz, K. G. McNeill, and S. Zukotynski, "Electron emission at the surface of metal tritide films," *Journal of Alloys and Compounds*, vol. 253, pp. 62-65, May 20 1997.
- [78] A. Kavetsky, G. Yakubova, M. Sychov, Q. Lin, G. Walter, D. Chan, S. Yousaf, H. Socarras, J. Abrefah, and K. Bower, "Tritium-Charged Capacitor," *Nuclear Science and Engineering*, vol. 159, pp. 321-329, July 2008 2008.
- [79] B. Liu, K. P. Chen, N. P. Khernai, S. Zukotynski, and A. B. Antoniazzi, "Betavoltaics using scandium tritide and contact potential difference," *Applied Physics Letters*, vol. 92, p. 083511, 2008.
- [80] A. W. P. Poon, R. J. Komar, C. E. Waltham, M. C. Browne, R. G. H. Robertson, N. P. Kherani, and H. B. Mak, "A compact H-3(p,gamma)He-4 19.8-MeV gamma-ray source for energy calibration at the Sudbury Neutrino Observatory," *Nuclear Instruments & Methods in Physics Research Section a-Accelerators Spectrometers Detectors and Associated Equipment*, vol. 452, pp. 115-129, Sep 21 2000.
- [81] L. C. Olsen, "Review of betavoltaic energy conversion," in *Proceedings of the 12th Space Photovoltaic Research and Technology Conference*, 1992, pp. 256-267.
- [82] B. Liu, K. P. Chen, N. P. Kherani, S. Zukotynski, and A. B. Antoniazzi, "Tritium locked in silica using 248 nm KrF laser irradiation," *Applied Physics Letters*, vol. 88, p. 134101, Mar 27 2006.
- [83] A. Lakhtakia, *The Handbook of Nanotechnology. Nanometer Structures: Theory, Modeling, and Simulation*. Bellingham, WA, USA: SPIE Press, 2004.
- [84] L. E. Foster, *Nanotechnology: Science, Innovation, and Opportunity*: Prentice Hall, December 21 2005.
- [85] S. Jijima, "Helical microtubules of graphite carbon," *Nature*, vol. 56, p. 354, 1991.

- [86] M. Meyyappan, L. Delzeit, A. Cassell, and D. Hash, "Carbon nanotube growth by PECVD: a review," *Plasma Sources Science & Technology*, vol. 12, pp. 205-216, May 2003.
- [87] L. Jiang, G. F. Huang, H. X. Li, X. F. Li, W. P. Hu, Y. Q. Liu, and D. B. Zhu, "Self-assembled molecular electronic devices," *Progress in Chemistry*, vol. 17, pp. 172-179, Jan 2005.
- [88] V. N. Popov, "Carbon nanotubes: properties and application," *Materials Science & Engineering R-Reports*, vol. 43, pp. 61-102, Jan 15 2004.
- [89] M. Law, J. Goldberger, and P. D. Yang, "Semiconductor nanowires and nanotubes," *Annual Review of Materials Research*, vol. 34, pp. 83-122, 2004.
- [90] D. Pribat, C. S. Cojocaru, M. Gowtham, L. Eude, P. Bondavalli, and P. Legagneux, "Carbon nanotubes and semiconductor nanowires for active-matrix backplanes," *Journal of the Society for Information Display*, vol. 15, pp. 595-600, Aug 2007.
- [91] G. Viswanathan, D. B. Kane, and P. J. Lipowicz, "High efficiency fine particulate filtration using carbon nanotube coatings," *Advanced Materials*, vol. 16, pp. 2045-+, Nov 18 2004.
- [92] C. Liu, Y. Y. Fan, M. Liu, H. T. Cong, H. M. Cheng, and M. S. Dresselhaus, "Hydrogen storage in single-walled carbon nanotubes at room temperature," *Science*, vol. 286, pp. 1127-1129, Nov 5 1999.
- [93] P. Chen, X. Wu, J. Lin, and K. L. Tan, "High H-2 uptake by alkali-doped carbon nanotubes under ambient pressure and moderate temperatures," *Science*, vol. 285, pp. 91-93, Jul 2 1999.
- [94] [Anon], "Alkali-doped carbon nanotubes absorb H-2 at ambient pressure," *Chemical & Engineering News*, vol. 77, pp. 29-29, Jul 5 1999.
- [95] Q. Y. Wang, S. R. Challa, D. S. Sholl, and J. K. Johnson, "Quantum sieving in carbon nanotubes and zeolites," *Physical Review Letters*, vol. 82, pp. 956-959, Feb 1 1999.
- [96] S. R. Challa, D. S. Sholl, and J. K. Johnson, "Light isotope separation in carbon nanotubes through quantum molecular sieving," *Physical Review B*, vol. 6324, pp. -, Jun 15 2001.
- [97] B. Liu, N. P. Kherani, K. P. Chen, and S. Zukotynski, "Tritiation of semiconductor materials for micropower application," *Fusion Science and Technology*, vol. 54, pp. 627-630, 2008.

- [98] B. J. Landi, R. P. Raffaele, S. L. Castro, and S. G. Bailey, "Single-wall carbon nanotube-polymer solar cells," *Progress in Photovoltaics*, vol. 13, pp. 165-172, Mar 2005.
- [99] C. L. Renschler, J. T. Gill, R. J. Walko, C. S. Ashley, T. J. Shepodd, S. T. Reed, G. M. Malone, L. E. Leonard, R. E. Ellefson, and R. L. Clough, "Solid-State Radioluminescent Lighting," *Radiation Physics and Chemistry*, vol. 44, pp. 629-644, Dec 1994.
- [100] A. Korin, M. Givon, and D. Wolf, "Parameters affecting the intensity of light sources powered by tritium," *Nuclear Instruments & Methods* vol. 130, p. 231, 1975.
- [101] N. Z. Galunov, "Mechanism of Radioluminescence of Condensed Organic Media," *Jetp Letters*, vol. 57, pp. 567-570, May 10 1993.
- [102] A. M. B. Dorego, J. L. Dasilva, and M. I. Morais, "Radioluminescence Yield of Polymeric Films - Dynamic-Model in the Delayed Component Treatment," *Nuclear Tracks and Radiation Measurements*, vol. 20, pp. 465-473, Jul 1992.
- [103] J. T. Gill, D. B. Hawkins, and C. L. Renschler, "Solid-State Radioluminescent Sources Using Tritium-Loaded Zeolites, and Their Proposed Use as Process Monitors," *Fusion Technology*, vol. 21, pp. 325-329, Mar 1992.
- [104] H. E. Ruda, L. Z. Jedral, and L. Mannik, "Semiconductor based light emitters powered by tritium," *Applied Physics Letters*, vol. 71, pp. 2644-2646, Nov 3 1997.
- [105] L. Dai, X. L. Chen, W. J. Wang, T. Zhou, and B. Q. Hu, "Growth and luminescence characterization of large-scale zinc oxide nanowires," *Journal of Physics-Condensed Matter*, vol. 15, pp. 2221-2226, Apr 9 2003.
- [106] N. E. Hsu, W. K. Hung, and Y. F. Chen, "Origin of defect emission identified by polarized luminescence from aligned ZnO nanorods," *Journal of Applied Physics*, vol. 96, pp. 4671-4673, Oct 15 2004.
- [107] J. B. Cui, "Defect control and its influence on the exciton emission of electrodeposited ZnO nanorods," *Journal of Physical Chemistry C*, vol. 112, pp. 10385-10388, Jul 17 2008.
- [108] Y. Y. Gong, T. Andelman, G. F. Neumark, S. O'Brien, and I. L. Kuskovsky, "Origin of defect-related green emission from ZnO nanoparticles: effect of surface modification," *Nanoscale Research Letters*, vol. 2, pp. 297-302, Jun 2007.
- [109] X. L. Wu, G. G. Siu, C. L. Fu, and H. C. Ong, "Photoluminescence and cathodoluminescence studies of stoichiometric and oxygen-deficient ZnO films," *Applied Physics Letters*, vol. 78, pp. 2285-2287, Apr 15 2001.

- [110] Y. C. Kong, D. P. Yu, B. Zhang, W. Fang, and S. Q. Feng, "Ultraviolet-emitting ZnO nanowires synthesized by a physical vapor deposition approach," *Applied Physics Letters*, vol. 78, pp. 407-409, Jan 22 2001.
- [111] Z. H. Wu, X. Y. Mei, D. Kim, M. Blumin, and H. E. Ruda, "Growth of Au-catalyzed ordered GaAs nanowire arrays by molecular-beam epitaxy," *Applied Physics Letters*, vol. 81, pp. 5177-5179, Dec 30 2002.
- [112] U. Philipose, S. V. Nair, S. Trudel, C. F. de Souza, S. Aouba, R. H. Hill, and H. E. Ruda, "High-temperature ferromagnetism in Mn-doped ZnO nanowires," *Applied Physics Letters*, vol. 88, p. 263101, Jun 26 2006.
- [113] M. Buric, K. P. Chen, M. Bhattarai, P. R. Swinehart, and M. Maklad, "Active fiber Bragg grating hydrogen sensors for all-temperature operation," *Ieee Photonics Technology Letters*, vol. 19, pp. 255-257, Mar-Apr 2007.
- [114] C. Jewart, K. P. Chen, B. McMillen, M. M. Bails, S. P. Levitan, J. Canning, and I. V. Avdeev, "Sensitivity enhancement of fiber Bragg gratings to transverse stress by using microstructural fibers," *Optics Letters*, vol. 31, pp. 2260-2262, Aug 1 2006.
- [115] M. Buric, J. Falk, K. P. Chen, L. Cashdollar, and A. Elyamani, "Piezo-electric tunable fiber Bragg grating diode laser for chemical sensing using wavelength modulation spectroscopy," *Optics Express*, vol. 14, pp. 2178-2183, Mar 20 2006.
- [116] C. Jewart, B. McMillen, S. K. Cho, and K. P. Chen, "X-probe flow sensor using self-powered active fiber Bragg gratings," *Sensors and Actuators a-Physical*, vol. 127, pp. 63-68, Feb 28 2006.
- [117] Q. Y. Chen, K. P. Chen, W. Xu, and S. Nikumb, "Deep ultraviolet femtosecond laser tuning of fiber Bragg gratings," *Optics Communications*, vol. 259, pp. 123-126, Mar 1 2006.
- [118] B. McMillen, C. Jewart, M. Buric, K. P. Chen, Y. Lin, and W. Xu, "Fiber Bragg grating vacuum sensors," *Applied Physics Letters*, vol. 87, pp. -, Dec 5 2005.
- [119] L. J. Cashdollar and K. P. Chen, "Fiber Bragg grating flow sensors powered by in-fiber light," *Ieee Sensors Journal*, vol. 5, pp. 1327-1331, Dec 2005.
- [120] K. P. Chen, B. McMillen, M. Buric, C. Jewart, and W. Xu, "Self-heated fiber Bragg grating sensors," *Applied Physics Letters*, vol. 86, pp. -, Apr 4 2005.

- [121] K. P. Chen, L. J. Cashdollar, and W. Xu, "Controlling fiber Bragg grating spectra with in-fiber diode laser light," *Ieee Photonics Technology Letters*, vol. 16, pp. 1897-1899, Aug 2004.
- [122] H. Zhang and E. H. Kisi, "Formation of titanium hydride at room temperature by ball milling," *Journal of Physics-Condensed Matter*, vol. 9, pp. L185-L190, Mar 17 1997.
- [123] X. J. Gu, L. Guan, Y. F. He, H. B. B. Zhang, and P. R. Herman, "High-strength fiber Bragg gratings for a temperature-sensing array," *Ieee Sensors Journal*, vol. 6, pp. 668-671, Jun 2006.
- [124] K. P. Chen and P. R. Herman, "Photo sensitization of standard fibers with deep UV laser radiation," *Journal of Lightwave Technology*, vol. 21, pp. 1958-1968, Sep 2003.
- [125] K. P. Chen, P. R. Herman, R. Taylor, and C. Hnatovsky, "Vacuum-ultraviolet laser-induced refractive-index change and birefringence in standard optical fibers," *Journal of Lightwave Technology*, vol. 21, pp. 1969-1977, Sep 2003.
- [126] K. P. Chen, "Grating, Photosensitivity, and Poling in Silica Optical Waveguides with 157nm F2 Laser Radiation," in *Department of Electrical and Computer Engineering*. vol. Ph.D Toronto: University of Toronto, 2002.
- [127] P. J. Lemaire, R. M. Atkins, V. Mizrahi, and W. A. Reed, "High-Pressure H₂ Loading as a Technique for Achieving Ultrahigh UV Photosensitivity and Thermal Sensitivity in GeO₂ Doped Optical Fibers," *Electronics Letters*, vol. 29, pp. 1191-1193, Jun 24 1993.
- [128] T. Erdogan, V. Mizrahi, P. J. Lemaire, and D. Monroe, "Decay of Ultraviolet-Induced Fiber Bragg Gratings," *Journal of Applied Physics*, vol. 76, pp. 73-80, Jul 1 1994.
- [129] F. M. Araujo, E. Joanni, M. B. Marques, and O. G. Okhotnikov, "Dynamics of infrared absorption caused by hydroxyl groups and its effect on refractive index evolution in ultraviolet exposed hydrogen loaded GeO₂-doped fibers," *Applied Physics Letters*, vol. 72, pp. 3109-3111, Jun 15 1998.
- [130] R. Kashyap, *Fiber Bragg Gratings*. San Diego, Calif.: Academic, 1999.
- [131] S. R. Baker, H. N. Rourke, V. Baker, and D. Goodchild, "Thermal decay of fiber Bragg gratings written in boron and germanium codoped silica fiber," *Journal of Lightwave Technology*, vol. 15, pp. 1470-1477, Aug 1997.
- [132] S. Kannan, J. Z. Y. Guo, and P. J. Lemaire, "Thermal stability analysis of UV-induced fiber Bragg gratings," *Journal of Lightwave Technology*, vol. 15, pp. 1478-1483, Aug 1997.

- [133] K. Kajihara, L. Skuja, M. Hirano, and H. Hosono, "Diffusion and reactions of hydrogen in F-2-laser-irradiated SiO₂ glass," *Physical Review Letters*, vol. 89, pp. 135507-1-4, Sep 23 2002.
- [134] H. C. Hartmann, "Evaluation of Tritiated Scandium for the Electron Capture Detector," *Analytical Chemistry*, vol. 45, pp. 733-739, 1973.
- [135] F. N. Simon and G. D. Rork, "Ionization-Type Smoke Detectors," *Review of Scientific Instruments*, vol. 47, pp. 74-80, 1976.
- [136] F. N. Simon and R. E. Axmark, "Space-Charge Effects in Ionization Type Particulate Detectors," *Review of Scientific Instruments*, vol. 48, pp. 122-126, 1977.
- [137] B. Liu, D. Alvarez-Ossa, N. P. Kherani, S. Zukotynski, and K. P. Chen, "Gamma-free smoke and particle detector using tritiated foils," *IEEE Sensors Journal*, vol. 7, pp. 917-918, May-Jun 2007.
- [138] B. Liu, D. Alvarez-Ossa, N. P. kherani, S. Zukotynski, and K. P. Chen, "Smoke and particle detector using tritiated semiconductor foil," *Fusion Science and Technology*, vol. 54, pp. 631-634, 2008.
- [139] A. Modi, N. Koratkar, E. Lass, B. Q. Wei, and P. M. Ajayan, "Miniaturized gas ionization sensors using carbon nanotubes," *Nature*, vol. 424, pp. 171-174, Jul 10 2003.